Fall 11-6-2023

WIND FARM OPTIMIZATION AND ANALYSIS OF COMPLEX WAKE STRUCTURES

Rubel Chandra Das

Recommended Citation

Das, Rubel Chandra. "WIND FARM OPTIMIZATION AND ANALYSIS OF COMPLEX WAKE STRUCTURES." (2023). https://digitalrepository.unm.edu/me_etds/263

Rubel Chandra Das

Candidate

Mechanical Engineering

Department

This dissertation is approved, and it is acceptable in quality and form for publication:

Approved by the Dissertation Committee:

Dr. Yu-Lin Shen , Chairperson

Dr. Peter Vorobieff

Dr. Sang Lee

Dr. Gowtham Mohan

WIND FARM OPTIMIZATION AND ANALYSIS OF COMPLEX WAKE STRUCTURES

by

RUBEL CHANDRA DAS

B.Sc., Mechanical Engineering, Bangladesh University of
Engineering & Technology, 2015
M.Sc., Mechanical Engineering, Bangladesh University of
Engineering & Technology, 2017

DISSERTATION

Submitted in Partial Fulfillment of the
Requirements for the Degree of

Doctor of Philosophy
Engineering

The University of New Mexico
Albuquerque, New Mexico
May, 2024

DEDICATION

To all the good people out there, fighting alone, in and out.

ACKNOWLEDGEMENTS

I would like to extend my sincere appreciation to Dr. Yu-Lin Shen, my esteemed advisor and dissertation chair, for his unwavering encouragement and guidance throughout the years. I am deeply grateful for his invaluable mentorship, which was instrumental in my successful completion of this dissertation. Dr. Shen's professional style and mentorship will continue to inspire me as I advance in my academic and professional pursuits.

I would also like to express my gratitude to Dr. Sang Lee for his unwavering guidance and mentorship throughout my PhD journey. Additionally, I extend my thanks to my esteemed committee members, Dr. Peter Vorobieff and Dr. Gowtham Mohan, for their valuable feedback on my research study and their support in my professional development.

I am also immensely grateful to the University of New Mexico (UNM), particularly the Mechanical Engineering department, and the Center for Advanced Research and Computing (CARC) at UNM for their invaluable assistance and resources.

I would like to give special thanks to my friends for their invaluable cooperation and support throughout my academic journey. Finally, I express my profound gratitude to my loving parents and supportive brothers for their unwavering encouragement and support.

WIND FARM OPTIMIZATION AND ANALYSIS OF COMPLEX WAKE STRUCTURES

By

Rubel Chandra Das

B.Sc., Mechanical Engineering, Bangladesh University of Engineering & Technology, 2015

M.Sc., Mechanical Engineering, Bangladesh University of Engineering & Technology, 2017

Ph.D., Engineering, University of New Mexico, 2024

ABSTRACT

A high-fidelity computational solver was developed with direct numerical simulation (DNS), large eddy simulation (LES), and Concurrent Precursor Method (CPM) capabilities. Extensive validation ensured the solver's accuracy in modeling fluid dynamics, including the wake characteristics of both utility and miniature-scale wind turbines. Key performance statistics (e.g., velocity and turbulence intensity profiles) were compared against established theoretical, computational, and experimental results. The study examined the influence of ground clearance on turbine performance, comparing two scenarios with different hub heights. Results showed that larger ground clearance facilitates quicker wake recovery. Finally, the study uses a nine-turbine array model to explore wind farm behavior under varying wind conditions and yaw angles. This analysis highlighted that wind speed variations and yaw adjustments impact wake characteristics and power output, with implications for optimizing wind farm efficiency. The research provides insights into enhancing energy extraction and advancing wind energy technology, contributing to sustainable renewable energy development.

Table of Contents

LIST OF FIGURES

LIST OF TABLES

Chapter 1

INTRODUCTION

Wind energy is a renewable energy source at the forefront of the movement to reduce carbon emissions. It is harnessed from the natural flow of air in our atmosphere. Modern wind turbines are more efficient, durable, and capable of harnessing wind energy even in suboptimal conditions, thanks to blade design, materials, and aerodynamics advancements. As the wind industry has expanded, the scale of production has reduced costs, making wind energy increasingly competitive with fossil fuels in many regions. Due to its zero-emission nature, wind energy has become a preferred choice for many nations aiming to meet their environmental targets. It also allows countries to reduce their dependence on imported fossil fuels, promoting energy security and reducing geopolitical risks associated with fuel imports. The wind industry has created numerous jobs worldwide, contributing to economic growth in regions with wind farms. Integrating wind power into the energy mix ensures a more diverse and resilient grid, reducing the reliance on a single energy source and stabilizing energy prices. The intermittent nature of wind power is becoming less of a challenge with the development of better energy storage solutions and grid management systems. This means that stored energy can be dispatched to meet demand even when the wind isn't blowing. The global commitment to a more sustainable future and the tangible benefits of wind energy have accelerated its adoption. As nations rally towards greener initiatives and more ambitious climate goals, wind energy is anticipated to continue to grow and contribute significantly to global electricity generation. The importance of wind energy is growing due to lower energy costs. Researchers around the world are studying the fluid dynamical physics of turbine wakes. Appropriate numerical representation of the real-world wind turbine is crucial for investigating numerous characteristics of the wakes.

Figure 3.6 and Figure 3.6 respectively showcase an actual offshore wind farm operating in Denmark and a three-dimensional view of the wind farm's streamwise velocity component flow field as simulated through our research. These visual representations offer insight into the intricate wake interactions and their consequential impacts on downstream turbines. It is imperative to optimize wind farms whilst minimizing wake effects to ensure successful commercial operations.

Figure 1.1. Vattenfall Horns Rev Offshore Wind Farm, Denmark (Photo by Christian Steiness).

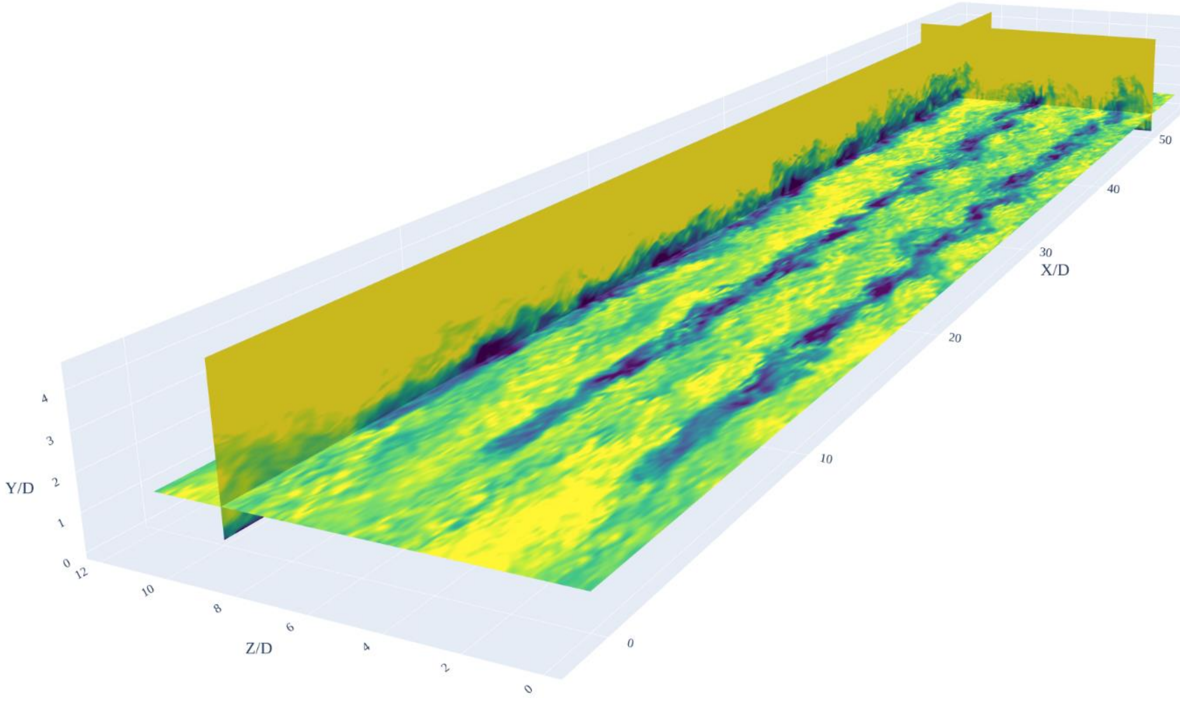

Figure 1.2. A three-dimensional cross-sectional view of streamwise velocity component revealing the wake effects in the downstream turbines, obtained from our wind farm simulation.

The construction of very large wind farms has become a recent trend. However, the flow dynamics within these wind farms are quite complex due to the interaction between the turbines' wakes and the atmospheric flow above the wind farm. The operation of wind turbines is negatively impacted by wakes created by upstream turbines [1]. The design and operation of expansive wind farms introduce intricate flow dynamics. The challenge lies in the interactions between individual wind turbine wakes, coupled with their interaction with the overarching atmospheric boundary layer. The intricacies of wind turbine wakes remain a topic of ongoing research, with many aspects yet to be fully understood. These wakes are characterized by turbulent eddies spanning multiple scales: from the larger integral scales, approximately the size of the rotor (on the order of 10^2 meters), to the much smaller Kolmogorov microscales (on the order of 10^{-3} meters).

When wind flows past a turbine, it creates a wake that is characterized by reduced wind speeds and increased turbulence. The turbine's rotor shapes this wake, which presents a region of disturbed flow that extends downstream. A turbine positioned within the wake of an upstream turbine experiences decreased wind speeds, leading to suboptimal power generation [2]. Moreover, the increased turbulence within the wake can lead to greater wear and tear on turbine components, potentially reducing the lifespan of the equipment and increasing maintenance costs.

The atmospheric boundary layer is the layer of air near the Earth's surface, typically up to 1-2 km in height. Within this layer, wind speeds and directions can vary significantly due to ground roughness, thermal effects, and other atmospheric conditions. As wind farms grow in size, turbines' interactions with these varying conditions become more complex, especially when considering the vertical distribution of wind speeds, known as wind shear. In large wind farms, the wakes of individual turbines can merge, leading to even more extensive regions of reduced wind speed and heightened turbulence. This merged wake can affect multiple downstream turbines, amplifying the negative impacts [3].

Advanced wind farm design strategies are being explored to mitigate these challenges. Some methods include optimizing turbine spacing and layout, incorporating varying hub heights, and employing advanced control strategies. Additionally, computational fluid dynamics (CFD) simulations and wind tunnel tests are being used to understand and predict wake interactions better, informing design and operational decisions. Large Eddy Simulation (LES) has emerged as a powerful tool for conducting high-fidelity numerical simulations of wind farm flows [4–6]. LES has the capability to accurately capture the unsteady, large-scale turbulent structures and their interactions with wind turbine rotors, making it an invaluable tool for studying and optimizing wind farm flows.

In conclusion, while the construction of larger wind farms is a testament to the growing trust and reliance on wind energy, it also underscores the need for advanced research and innovative strategies to address the aerodynamic challenges posed by turbine interactions. Properly addressing these challenges will be crucial for maximizing the efficiency and longevity of these significant renewable energy investments. Wind farms often consist of dozens, if not hundreds, of turbines. As such, when scaled across numerous turbines, an improvement of less than 1% in efficiency or output can result in a considerable increase in the overall electricity generated, enhancing revenue.

To properly study all the wake dynamics related to wind farm optimization, a high-fidelity computational fluid dynamics (CFD) solver has been developed. The solver includes different features, such as Large Eddy Simulation (LES) and Direct Numerical Simulation (DNS) capability, as well as shifted periodic boundary layers using two methods. Additionally, several LES subgrid models are available in the solver, along with the concurrent precursor method, which uses both the precursor domain and test domain. Although other features are available in the solver, this discussion will focus only on the LES-related features for brevity in **Chapter 2**. **Chapter 3** presents the rigorous validation conducted on a newly developed solver. The results of the study on the ground proximity of wind turbines are discussed in **Chapter 4** and were presented in the APS-DFT meeting [7]. The impact of different wind speeds and yaw angles on wind farms is studied in **Chapter 5**, which was published in Energies [8]. **Chapter 6** concludes the discussion.

Chapter 2

NUMERICAL METHODS

2.1 Introduction

Large Eddy Simulation (LES) is a mathematical approach used in computational fluid dynamics to model turbulence, particularly in high Reynolds number flows. It was introduced by Joseph Smagorinsky in 1963 to simulate atmospheric air currents [9], which was a significant advancement in representing turbulent flows. The approach filters out the smaller scales and focuses on the larger, energy-containing scales to reduce the computational burden of capturing the full spectrum of turbulent eddies, unlike Direct Numerical Simulation (DNS). In 1970, Deardorff refined the LES methodology, introducing new subgrid-scale models and techniques[10]. Consequently, LES has become a popular method for studying complex turbulent flows in various engineering and scientific applications. Its accuracy and effectiveness depend on the subgrid-scale models employed and the resolution of the computational mesh. These foundational contributions laid the groundwork for its wide adoption and continued evolution in simulating atmospheric, oceanic, and other flows.

2.2 Governing Equations and LES Framework

For the current study, a neutral atmospheric boundary layer formulation of the filtered Navier-Stokes equations with the continuity equation, neglecting the Coriolis force, has been considered.

$$\frac{\partial \tilde{u}_i}{\partial t} + \frac{\partial \tilde{u}_i \tilde{u}_j}{\partial x_j} = -\frac{\partial \tilde{p}^*}{\partial x_i} + \frac{\partial \tau_{ij}}{\partial x_j} + \tilde{F}_i \qquad 2.1$$

$$\frac{\partial \tilde{u}_i}{\partial x_i} = 0 \qquad 2.2$$

Where $\tilde{u}_i$(or u, v, w) is the filtered or resolved velocity at the filter width (Δ) and x_i(or x, y, z) is the Cartesian coordinates in the i-direction, with i = 1, 2, or 3, corresponding to the streamwise, vertical or spanwise directions respectively. The modified pressure term, $\tilde{p}^*$ (for more details, see [11]), is defined as follows.

$$\tilde{p}^* = \tilde{p} + (1/3)\rho\sigma_{kk} + (1/2)\rho\tilde{u}_i\tilde{u}_j \qquad 2.3$$

Here τ_{ij} is the subgrid-scale (SGS) stress tensor, ρ is the fluid density (constant), t is time, and $\tilde{F}_i$ is the body force. The SGS terms are parametrized with the Lagrangian-averaged scale-dependent (LASD) model [11]. The LASD model dynamically calculates the local Smagorinsky coefficient $C_{s\Delta}$ at every grid point. It allows for a better representation of turbulence structures and their interactions with the resolved flow features. There have been several methods developed from pioneer works of Smagorinsky back in 1963 to today. A brief discussion of the subgrid models is given in section 2.5.

2.3 Solver Numerics

A concurrent precursor method (CPM) was implemented in the in-house code, WIND4D [7]. The equations are discretized using a structured, staggered, finite-volume formulation with a second-order central differencing scheme. The code employs a second-order Adams-Bashforth on the convective terms and the stress terms. A fractional-step method is used to uncouple the pressure and flow fields from the momentum and the continuity equation. This method yields a pressure Poisson equation which is solved by a multigrid solver called HYPRE [12]. The code is fully parallelized via Message Passing Interface (MPI). The code employs a concurrent recycling inflow domain which saves time and storage to run simulations.

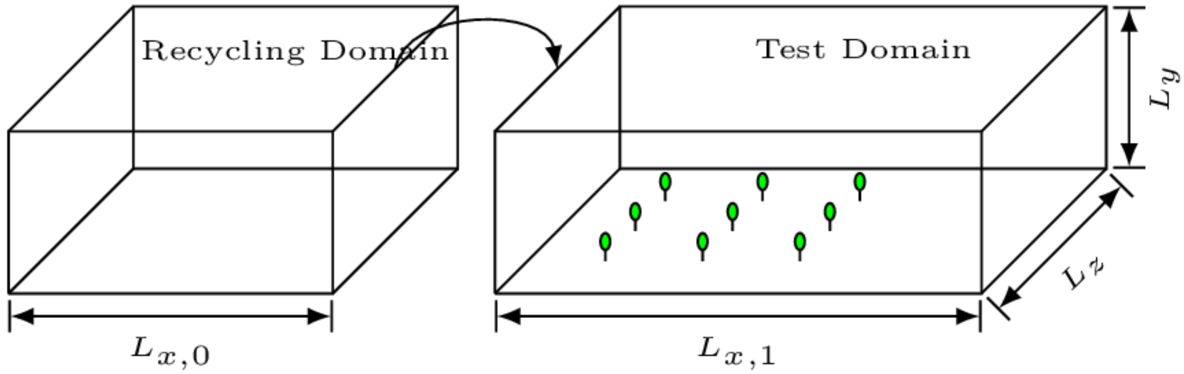

Figure 2.1. The representation of concurrent precursor method with the recycling domain and the test domain.

A common method to filter the velocity field is by applying an explicit filter directly to it. The box filter is a simple and widely-used option for this operation. Its function is to average the velocity across a fixed and predetermined volume or "box" within the computational domain. In our LES, explicit filtering is performed at test or second test levels using a box or top hat filter. Filtering is conducted along the horizontal directions in physical space in a two-dimensional manner. To calculate the discrete integral, the trapezoidal rule is used. The first test filtering is performed with a width twice that of the horizontal grid spacing, denoted as $\triangle$. The second test filtering has a filter width of four times $\triangle$.

The velocity components are calculated at the face centers of the finite volume cell. The off-diagonal parts of the strain-rate tensor $\tilde{S}_{ij}$ are computed at the midpoints of the edges, while the diagonal components of $\tilde{S}_{ij}$ and modified pressure $\tilde{p}^*$ are calculated at the center of the cell. The eddy viscosity ν_T and the deviatoric normal stress components are computed at the cell's center, while the deviatoric shear stress components are stored at the midpoints of the edges. The SGS stress components are staggered in storage, making it easy to calculate the gradient of the components at the corresponding velocity points. Linear interpolations are used when off-diagonal components are needed at the cell center or when the cell-centered values are needed at the edges or faces. The convective terms are calculated at their corresponding velocity points. The divergence form of the convective terms performs slightly better than the advective form for this solver.

2.4 Boundary Conditions and Wall-model

Periodic boundary conditions (BCs) in the horizontal directions (recycling domain) and inflow-outflow boundary conditions in the streamwise direction with zero pressure gradient (test domain) are used. A new boundary condition ($u_0 = u_1 - \frac{du}{dy}dy, w_0 = w_1 - \frac{dw}{dy}dy$) at the wall to calculate the convective terms is imposed, and the velocity gradients are calculated from the wall stress model; it was found that this new boundary works better than no-slip boundary condition and any velocity extrapolations for the ghost points. A stress-free boundary condition at the top (i.e., $\frac{\partial \tilde{u}_i}{\partial x_2} = 0,\ i = 1,3$ and $\tilde{u}_2 = 0$) is enforced, which acts like a half channel with an impermeable centerline boundary.

Due to the current study’s focus on very high Reynolds number flows, where molecular viscosity is minimal at the resolved scales like in the most LES simulations, and the wall layer is modeled, the molecular viscous factor is not taken into consideration. A local similarity model [10] is used to calculate the shear stresses at the surface in Equation 2.4.

$$\tau_w(x,z) = -[\kappa/[ln(dy/2)/y_0]]^2([\,\bar{\tilde{u}}_1(x,dy/2\,,z)]^2 + [\bar{\tilde{u}}_3(x,dy/2\,,z)]^2) \qquad 2.4$$

Here y_0 is the surface roughness factor and $\bar{\tilde{u}}$ is the filtered velocity at first test-filter scale. Using the Equation 2.4 the horizontal shear stress components τ_{xy} and τ_{zy} are computed according to

$$\tau_{i,y}^{wall}(x,z) = \tau_w(x,z)\left[\frac{\bar{\tilde{u}}_i(x,dy/2\,,z)}{\sqrt{\bar{\tilde{u}}_1^2+\bar{\tilde{u}}_3^2}}\right], i = x,z \qquad 2.5$$

It should be noted that the wall shear stresses are computed at the first grid point away from wall at a distance $dy/2$ for a staggered grid discretization.

2.5 Subgrid Models

Large-eddy simulation (LES) has become an important numerical tool for the study of high Reynolds number atmospheric and engineering turbulent flows. In LES, the larger eddies are resolved and smaller eddies are modeled. This section explores the numerical aspects of different subgrid models, focusing on their objectives and limitations. It aims to provide a clear understanding of these models and their limitations.

2.5.1 Smagorinsky-Lilly model with wall-damping:

The classic and widely used Smagorinsky model is based on the eddy-viscosity ν_T and mixing length ℓ theories. The deviatoric subgrid-scale (SGS) stress tensor, τ_{ij} according to [9] is given by Equation 2.6

$$\tau_{ij} = 2\nu_T\tilde{S}_{ij} = 2\ell_S^2|\tilde{S}|\tilde{S}_{ij} = 2(c_{s\Delta}\Delta)^2|\tilde{S}|\tilde{S}_{ij} \qquad 2.6$$

$$\tilde{S}_{ij} = 0.5\left(\partial_j\tilde{u}_i + \partial_i\tilde{u}_j\right) \qquad 2.7$$

$$|\tilde{S}| = \sqrt{2\tilde{S}_{ij}\tilde{S}_{ij}} \qquad 2.8$$

Here ν_T is the eddy viscosity, $\tilde{S}_{ij}$ is the resolved strain rate, $|\tilde{S}|$ is the strain rate magnitude. Introducing the wall-damping function as defined in Equation 2.9, Mason and Thomson [13] eliminates the excessive damping of the turbulence generation and insufficient kinetic energy for the resolved scales near the surface.

$$\frac{1}{\lambda^n} = \frac{1}{\lambda_0^n} + \frac{1}{[\kappa(y + y_0)]^n} \tag{2.9}$$

$$\lambda = C_{s,\Delta}\Delta \tag{2.10}$$

$$\lambda_0 = C_{s,0}\Delta \tag{2.11}$$

Here κ is the von-Karman constant and λ_0 is the mixing length away from the surface where homogeneous isotropic turbulence assumption holds. In the Equation 2.11, Lilly [14] used a fixed value of 0.16 for $C_{s,0}$. In this function, the mixing length λ (Equation 2.10) decreases smoothly following the behavior $\lambda \sim y$ near the wall. The Smagorinsky-Lilly model is still over dissipative despite use of the wall damping function and needs case to case calibration to get better results. This issue prompts the need of a dynamic model to calculate the coefficients.

2.5.2 Planar Averaging Scale-Invariant Dynamic model

The dynamic computation of the model coefficients was introduced by Germano et al. [15].The dynamic model coefficients are determined from the relation of SGS stresses across different scales intermediate between the grid scale (Δ) and a test-filter scale ($\alpha\Delta$).

$$L_{ij} = T_{ij} - \bar{\sigma}_{ij} = \overline{\tilde{u}_i\tilde{u}_j} - \bar{\tilde{u}}_i\bar{\tilde{u}}_j \tag{2.12}$$

Where L_{ij} is the Leonard stresses for the scales between Δ and $\alpha\Delta$, $\bar{\sigma}_{ij}$ is the SGS stress tensor at the grid scale Δ, T_{ij} is the stress tensor at the test-filter scale $\alpha\Delta$.

$$\bar{\tau}_{ij} = \bar{\sigma}_{ij}^{D} = -2c_{s,\Delta}^{2}\Delta^{2}\overline{|\tilde{S}|\tilde{S}_{ij}} \tag{2.13}$$

$$\bar{T}_{ij}^{D} = -2c_{s,\alpha\Delta}^{2}(\alpha\Delta)^{2}|\bar{\tilde{S}}|\bar{\tilde{S}}_{ij} \tag{2.14}$$

Putting Equation 2.13 and Equation 2.14 in Equation 2.12, yields an error function which is

$$e_{ij} = L_{ij}^{D} - \left(T_{ij}^{D} - \bar{\sigma}_{ij}\right) = L_{ij}^{D} - c_{s,\Delta}^{2}M_{ij} \tag{2.15}$$

Where M_{ij} is defined as

$$M_{ij} = 2\Delta^{2}\left[\overline{|\tilde{S}|\tilde{S}_{ij}} - \alpha^{2}\beta|\bar{\tilde{S}}|\bar{\tilde{S}}_{ij}\right] \tag{2.16}$$

To determine the values of C_s, a least-square error minimization of the $\langle e_{ij}e_{ij}\rangle$ leads to the following equation.

$$c_{s,\Delta}^{2} = \frac{\langle L_{ij}M_{ij}\rangle}{\langle M_{ij}M_{ij}\rangle} \tag{2.17}$$

Here $\langle \quad \rangle$ refers to an averaging over the planes in the homogeneous directions. This averaging eliminates the numerical instability which arises from the highly variable local coefficients.

2.5.3 Planar Averaging Scale-Dependent Dynamic model

To include the scale dependency, Porté-Agel et al. [16] introduced a second test-filter to define the relation between the stresses at different filter scales. In this model, a power-law behavior between C_s and Δ is assumed as following

$$c_{s,\Delta} \sim \Delta^{\phi} \tag{2.18}$$

The above equation in its more appropriate dimensional form

$$c_{s,\Delta} = c_{s,\alpha\Delta}(\Delta/\alpha\Delta)^{\phi} \tag{2.19}$$

To determine the $c_{s,\alpha\Delta}$, a second Germano identity for scales intermediate between Δ and $\alpha^2\Delta$ is defined as

$$c_{s,\alpha\Delta}^2 = \frac{\langle Q_{ij}N_{ij}\rangle}{\langle N_{ij}N_{ij}\rangle} \tag{2.20}$$

Here the resolved stress tensors (between Δ and $\alpha^2\Delta$) Q_{ij} and N_{ij} are given as

$$Q_{ij} = \widehat{\tilde{u}_\imath \tilde{u}_\jmath} - \hat{\tilde{u}}_\imath \hat{\tilde{u}}_\jmath \tag{2.21}$$

$$N_{ij} = 2\Delta^2 \left[\widehat{|\tilde{S}|\tilde{S}_{\imath\jmath}} - \alpha^4\beta^2 \left|\hat{\tilde{S}}\right| \hat{\tilde{S}}_{ij} \right] \tag{2.22}$$

A fifth-order polynomial for the β was obtained by equating Equation 2.17 and Equation 2.20. It should be noted that equating Equation 2.17 and Equation 2.20 leads to scale-invariant assumption in this scale-dependent model (more discussions in Porté-Agel et al. [16]). The scale-dependent values of $c_{s,\Delta}$ are measured by substituting β (obtained from solving the polynomial) in Equation 2.17. In many complex practical applications, the assumption of homogenous directions in the flow field doesn't hold, and this issue necessitates the next subgrid model.

2.5.4 Lagrangian Averaging Scale-Independent Dynamic model

Meneveau et al. [17] combined the local and time-averaged formulations to propose a Lagrangian-Averaged Scale-Invariant (LASI) model. The Lagrangian approach is justifiable since the large eddies at grid scales are convected along the fluid pathlines. Also, the energy cascade is most apparent in the Lagrangian frame of reference. Thus, this model works better in case of heterogenous directions since it preserves the local variability and Galilean invariance.

In this model, the coefficients are determined by minimizing the weighted time-average function, E (as defined in Equation 2.23) of the local error contraction $e_{ij}e_{ij}$ over the pathlines.

$$E = \int_{-\infty}^{t} e_{ij}[z(t'),t']e_{ij}[z(t'),t']W(t-t')dt' \tag{2.23}$$

Where $z(t')$ are the previous positions of the fluid elements and $W(t-t')$ is a relaxation function which allocates larger weights to the current values.

By performing $\partial E/\partial c_{s,\Delta}^2 = 0$, an expression for the $c_{s,\Delta}^2$ is obtained as follows

$$c_{s,\Delta}^2 = \frac{\Im_{LM}}{\Im_{MM}} \tag{2.24}$$

Where $\Im_{LM}$ and $\Im_{MM}$ are defined as following

$$\Im_{LM} = \int_{-\infty}^{t} L_{ij}M_{ij}[\boldsymbol{z}(t'),t']W(t-t')dt' \tag{2.25}$$

$$\Im_{MM} = \int_{-\infty}^{t} M_{ij}M_{ij}[\boldsymbol{z}(t'),t']W(t-t')dt' \tag{2.26}$$

Using the relaxation transport equations for $\Im_{LM}$ and $\Im_{MM}$, the resultant formulations for updating value from time-step "*n*" to "*n+1*" at location $\boldsymbol{x}$ is given by

$$\Im_{MM}^{n+1} = H\left[\epsilon\left[M_{ij}M_{ij}\right]^{n+1}(\boldsymbol{x}) + (1-\epsilon)\Im_{MM}^{n}(\boldsymbol{x} - \tilde{u}^n\Delta t)\right] \tag{2.27}$$

$$\Im_{LM}^{n+1} = H\left[\epsilon\left[L_{ij}M_{ij}\right]^{n+1}(\boldsymbol{x}) + (1-\epsilon)\Im_{LM}^{n}(\boldsymbol{x} - \tilde{u}^n\Delta t)\right] \tag{2.28}$$

Where $H(x)$ is a ramp function which clips the values of x if x goes to negative. The ramp function eliminates the negative values of $c_{s,\Delta}$ leading to a more accurate prediction of the coefficients. A multilinear interpolation is used to calculate the values at precious locations $\boldsymbol{x} - \tilde{u}^n\Delta t$.

And ϵ is defined as following

$$\epsilon = \frac{\Delta t/T^n}{1+\Delta t/T^n} \tag{2.29}$$

Where the time scale, T in the above equation is chosen as

$$T^n = 1.5\Delta(\Im_{LM}^{n}\Im_{MM}^{n})^{-1/8} \tag{2.30}$$

2.5.5 Lagrangian Averaging Scale-Dependent Dynamic model

To take account of scale-dependency of the coefficients in the Lagrangian formulation, the Lagrangian Averaged Scale-Dependent (LASD) model was proposed by Bou-Zeid et al. [11]. For this model, similar expressions like Equation 2.24 can be introduced for another two test filters for $\alpha = 2$ and $\alpha = 4$ as followings

$$c_{s,2\Delta}^2 = \frac{\mathfrak{I}_{LM}}{\mathfrak{I}_{MM}} \tag{2.31}$$

$$c_{s,4\Delta}^2 = \frac{\mathfrak{I}_{QN}}{\mathfrak{I}_{NN}} \tag{2.32}$$

Where $\mathfrak{I}_{QN}$ and $\mathfrak{I}_{NN}$ are defined similarly like $\mathfrak{I}_{LM}$ and $\mathfrak{I}_{MM}$ as following

$$\mathfrak{I}_{QN} = \int_{-\infty}^{t} Q_{ij}N_{ij}[\boldsymbol{z}(t'),t']W(t-t')dt' \tag{2.33}$$

$$\mathfrak{I}_{NN} = \int_{-\infty}^{t} N_{ij}N_{ij}[\boldsymbol{z}(t'),t']W(t-t')dt' \tag{2.34}$$

Thus, the scale-dependence parameter, β is measured as

$$\beta = \frac{c_{s,4\Delta}^2}{c_{s,2\Delta}^2} \tag{2.35}$$

And finally, the scale-dependent values for the $c_{s,\Delta}$ is determined according to

$$c_{s,\Delta}^2 = \frac{c_{s,2\Delta}^2}{\beta} \tag{2.36}$$

Since the values of β can vary from Zero to Infinity, β is clipped at 0.125 if it goes below the clipping value. This clipping occurs less than 15% of the time, and it helps to avoid numerical instability. Including the clipping, the formula of $c_{s,\Delta}$ can be written in the following form

$$c_{s,\Delta}^2 = \frac{\frac{\mathfrak{I}_{LM}}{\mathfrak{I}_{MM}}}{max(\beta, 0.125)} \tag{2.37}$$

Where expression for β can be simplified in the form of the following equation.

$$\beta = \frac{\Im_{QN}\Im_{MM}}{\Im_{NN}\Im_{LM}} \tag{2.38}$$

2.6 Time-Adaptive Wind-Turbine Model

When simulating wind farms with many turbines, using fine grid resolutions can be too expensive. For this reason, the Actuator Disk Method (ADM) is more appropriate for large wind farm simulations using a coarse grid. The ADM is a preferred approach for large wind farm simulations where the primary interest is in wake interactions, downstream effects, and overall farm performance, rather than detailed blade aerodynamics. The current study does not consider the actual blades of the turbine since the focus is on the downstream development of flow characteristics rather than the local properties of the flow that interacts with the wind turbine blades.

The thrust force of the turbine has been modeled with the classical actuator disk method [18].

$$\tilde{F_i} = f_e(x) * f_g(x) * C_T' \tag{2.39}$$

$$f_e(x) = \frac{1}{2}\rho(U_d^T)^2\frac{3}{2}\left[1-\left(\frac{r}{R}\right)^2\right]^{1/2} \tag{2.40}$$

$$f_g(x) = \frac{1}{\sigma\sqrt{2\pi}}e^{\frac{(x-x_c)^2}{-2\sigma^2}} \tag{2.41}$$

Here, the $f_e(x)$ is the elliptical distribution of the volume forces over the swept area, where R is the radius of the rotor. A Gaussian kernel $f_g(x)$ has been employed to smooth the point force over the streamwise direction, σ is the smoothing width, and x_c is the coordinate of the turbine center. Since the freestream U_∞ is not readily known in multi-turbine wind farms, the average velocity at the rotor disk U_d is used to calculate the thrust force of the turbine. From the actuator disk model based on momentum theory, U_∞, U_d, and induction factor a are related by

$$U_\infty = \frac{U_d}{(1-a)} \qquad 2.42$$

Since U_∞ has been replaced by U_d, C_T was substituted by C_T' according to

$$C_T' = \frac{C_T}{(1-a)^2} \qquad 2.43$$

A temporal moving average was applied on U_d over a time window of T using a first-order relaxation method (or exponential smoothing). This provides an extra cushion against the numerical instability of the LES code.

$$(U_d^T)^{n+1} = \epsilon U_d^n + (1-\epsilon)(U_d^T)^n \qquad 2.44$$

$$\epsilon = \frac{dt/T}{1+dt/T} \qquad 2.45$$

2.7 Yaw Implementation

Yaw misalignment was implemented based on [19]. In the presence of yaw, the thrust force was replaced as follows.

$$f = C_T \frac{1}{2} \rho A (U_\infty \, cos\theta)^2 \qquad 2.46$$

Then the thrust force was projected into the Cartesian coordinates with the x-component and the z-component being the following.

$$f_x = f cos\theta = C_T \frac{1}{2} \rho A (U_\infty \, cos\theta)^2 cos\theta \qquad 2.47$$

$$f_z = f sin\theta = C_T \frac{1}{2} \rho A (U_\infty \, cos\theta)^2 sin\theta \qquad 2.48$$

The thrust force was then incorporated into the respective momentum equation.

2.8 Conclusion

Despite having some shortcomings, the Large Eddy Simulation is still widely used in simulation of high Reynolds number environments. The selection of the proper LES model depends on the desired accuracy, the geometry, and the cost of computation. The WIND4D solver has both Direct Numerical Simulation and Large Eddy Simulation capabilities and is enhanced with the Concurrent Precursor Method. It uses several LES subgrid models with a sophisticated wall model, with the LASD model being primarily used for the investigations in this thesis. The solver is based on the Finite Volume Method, which operates on a structured grid. In addition, it includes the actuator disk method with a yaw modeling feature to model the turbine.

Chapter 3

VALIDATION

3.1 Introduction

The WIND4D solver is a significant step forward in wind simulation capabilities. Developed from the ground up, it utilizes the latest methodologies, algorithms, and computational techniques to address the intricacies of wind dynamics. However, development is only one aspect of the process, and ensuring the solver's accuracy and reliability is crucial, particularly when it is deployed in real-world scenarios.

After completing the solver's development, an exhaustive validation process was undertaken. WIND4D's output was compared against established benchmarks, experimental data, published simulation findings, and other validated computational models to ensure its accuracy.

The validation process was not confined to a limited set of conditions. Instead, the solver was tested under a wide range of scenarios to simulate the diverse conditions that it might encounter in real-world applications. This included varying wind speeds, yaw angles, etc.

In addition to qualitative comparison, the validation process also included detailed statistical analysis. The goal was to ensure that WIND4D not only provided visually accurate simulations but also produced data that adhered closely to expected statistical norms and benchmarks.

Any discrepancies or deviations identified during validation resulted in iterative refinements of the solver. Potential sources of errors were analyzed, algorithms were fine-tuned, and parameters were adjusted until the solver's output aligned with the expected results.

To further fortify its reliability, results from WIND4D were subjected to peer review through publications. External experts assessed and critiqued the solver, adding another layer of scrutiny to ensure its methodologies and results were sound.

In conclusion, the development of the WIND4D solver was a comprehensive undertaking that combined innovative development with rigorous validation, ensuring its reliability and accuracy in a variety of wind-related applications. All the simulations are carried out for a period long enough for the turbulence to become fully developed.

While the code has additional capabilities such as direct numerical simulation and shifted periodic boundary conditions (two methods were implemented to achieve this), we will only be presenting the validation results related to the large eddy simulation of wind farms for the sake of brevity in our discussions.

3.2 Validation of Precursor Domain

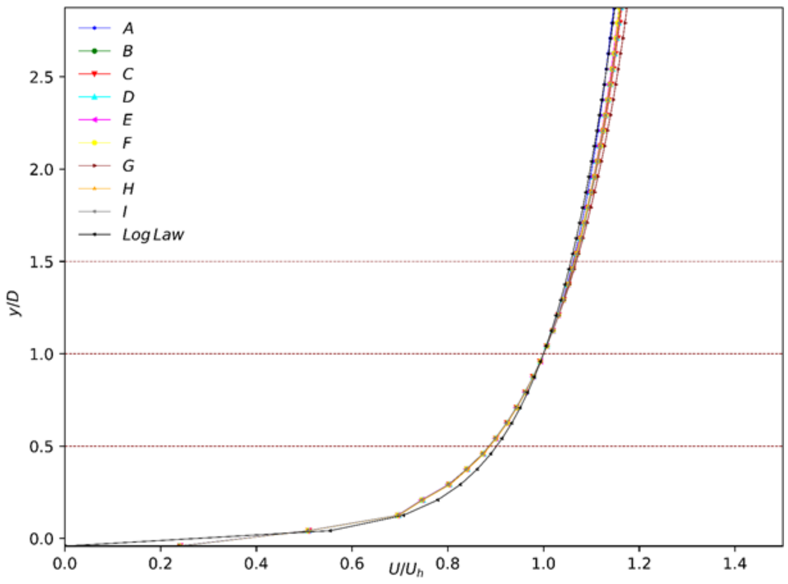

Figure 3.1. Comparison of the inflow profiles from the precursor domain with the logarithmic profile for various wind speed conditions.

Understanding the inflow profile is crucial in wind simulation studies as it forms the foundation for subsequent analyses. Figure 3.1 represents the inflow profile derived from the precursor domain. Each simulation scenario is rigorously compared against a well-established representation in boundary layer meteorology called the log law profile. All the case profiles in this study align with the log law profile and match it very closely, indicating the robustness and accuracy of the simulations. For readers interested in the technicalities of the simulation, section 5.2 and Table 5.1 provide a comprehensive outline of the methodologies, parameters, and configurations employed during the simulation process. The study's performance under varying wind speed conditions is notable. Simulations often exhibit discrepancies when faced with a range of input conditions, but this study consistently and closely adheres to the logarithmic profile regardless of the wind speed conditions. This reinforces the credibility and precision of the simulation framework.

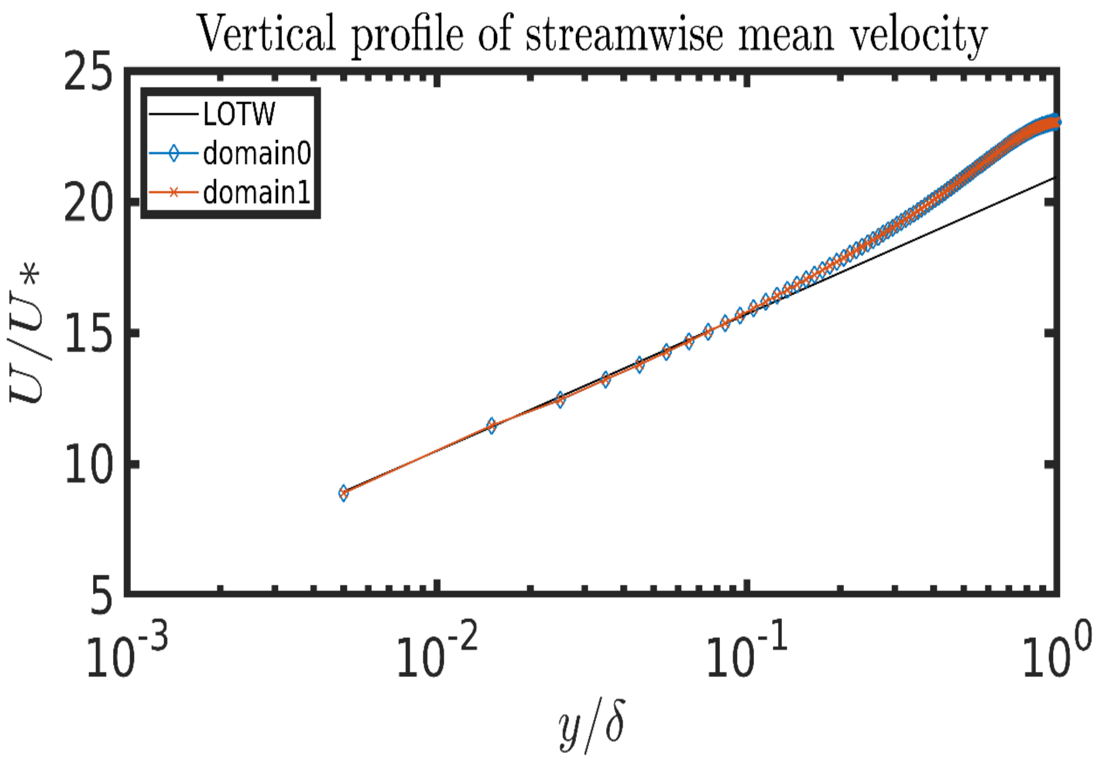

Figure 3.2. Mean velocity profile from precursor/recycling domain (domain0) and test domain (domain1).

Figure 3.2 shows mean velocity profiles from the precursor simulation in logarithmic scale. It represents the comparison of the velocity profiles from both precursor domain and test domain. All the profiles agree well with the standard log-law profile. The simulation configurations for this profile are (Lx=3000, Ly=1000m, Lz=2000m) and (Nx=100, Ny=100, Nz=100), friction velocity u^*=0.45 ms^{-1} and surface roughness y_0=0.1 m. Figure 3.6 represents the mean velocity gradient profile comparison against the theoretical logarithmic profile and the profiles match qualitatively well. The overshoot near the surface due to the wall shear stress model, and is common in wall-modelled flows.

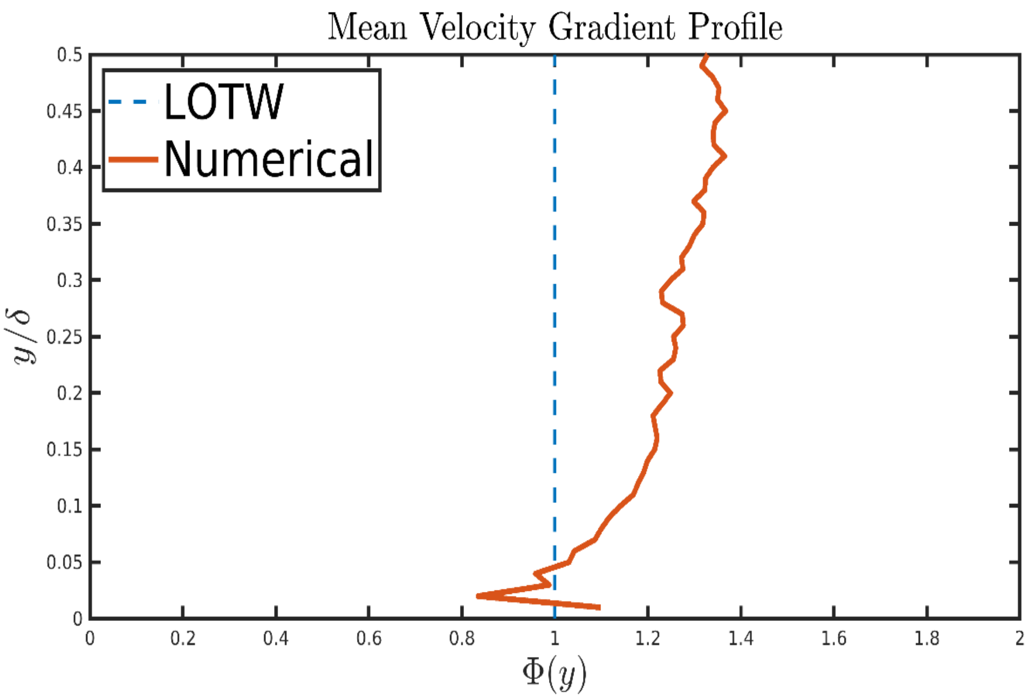

Figure 3.3. Mean velocity gradient profile against logarithmic profile.

The distribution of energy across different scales in fluid dynamics, particularly turbulence, is a crucial study area. It involves assessing the energy spectrum of kinetic energy within turbulent structures of varying sizes, known as eddies.

The energy spectrum of velocity components is analyzed at a specific distance from the wall, defined by the ratio y/δ = 0.1. Here, 'y' represents the distance from the wall, and 'δ' is the boundary layer thickness, a characteristic length scale. Figure 3.4 compares the simulated energy spectra results with established theoretical predictions. The -5/3 slope, also known as the "Kolmogorov -5/3 law," represents the inertial subrange of turbulence. It signifies where larger eddies transfer their energy to smaller ones without being influenced by viscosity. This slope is a universal feature observed in high Reynolds number turbulent flows. The -1 slope represents the energy-containing (or production) range of turbulence, where the most significant and energetic turbulent structures reside. Each of these profiles exhibits slopes of -

1 and -5/3, aligning with theoretical predictions. At the highest resolved wavenumbers, rapid energy decay occurs due to numerical dissipation caused by finite volume discretization.

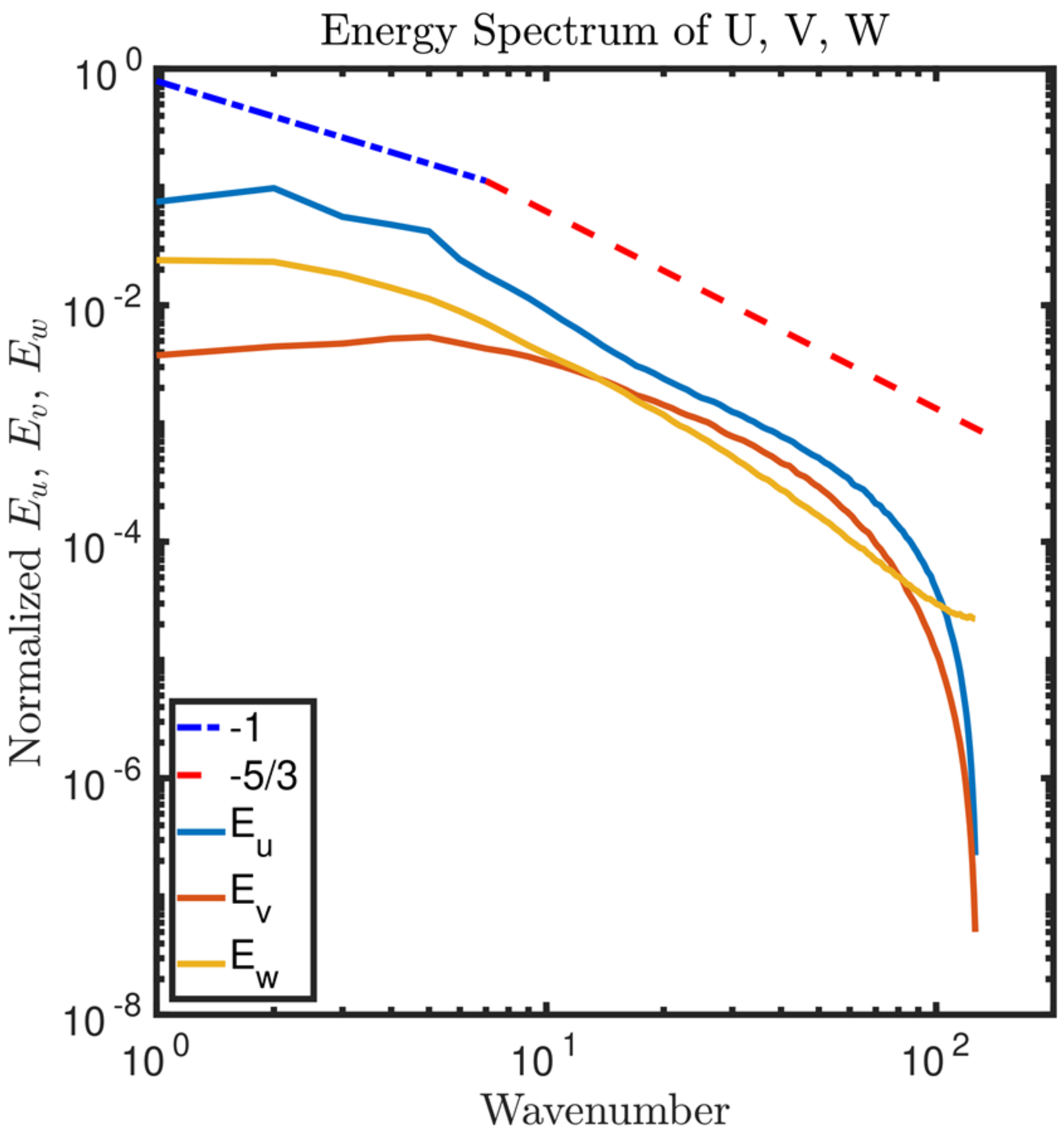

Figure 3.4. Energy spectrum (at y/δ = 0.1) of all the velocity components obtained precursor/recycling domain.

The Reynolds shear stress represents the physical transportation of momentum in the flow. In Figure 3.5, the summation of Reynolds shear stress and SGS shear stress has been compared with the theoretical profile of total streamwise stress. The results show a good match with the theoretical values. The stresses are normalized by the square of friction velocity, u^*.

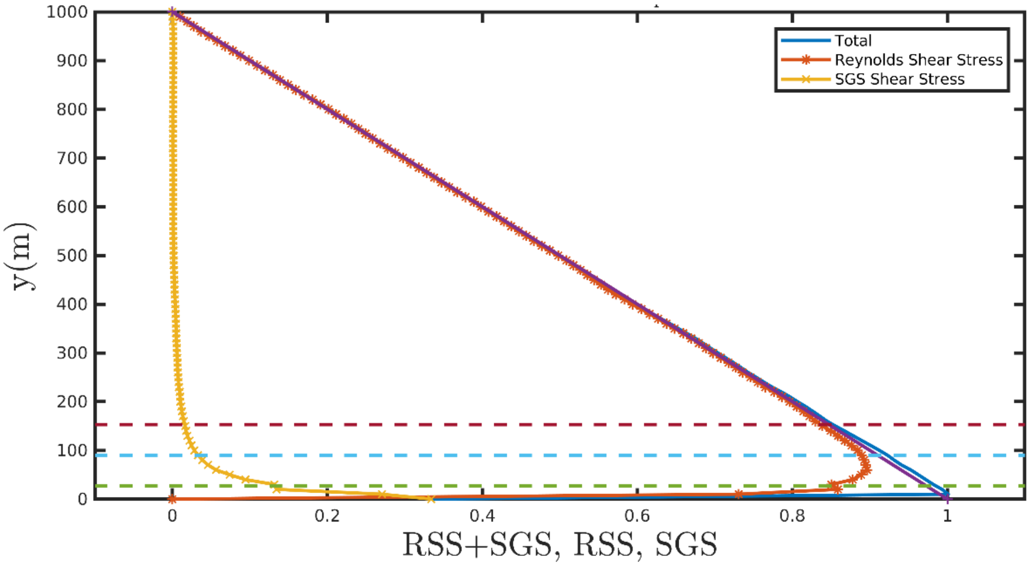

Figure 3.5. The comparison of summation of Reynolds shear stress and SGS shear stress with the theoretical profile of the total streamwise stress.

3.3 Wind Farm Validation

The following results are from a 3x10 wind farm simulation. This is a miniature-scale wind farm simulation using the actuator disk method (ADM) that has been done to validate the solver against EPFL experimental results by Chamorro and Porté-Agel [2010].

For this wind farm test case, the dimensions are (Lx_0 = 5.4 m, Lx_1 = 8.409375 m, Ly = 0.675 m, Lz = 1.8 m), grid points are (Nx_0 = 384, Nx_1 = 598, Ny = 144, Nz = 128), hub height = 0.125 m, diameter = 0.15 m, friction velocity $u^*=0.113\ ms^{-1}$ and surface roughness $y_0=0.03$ mm. The turbines are placed at a separation distance of 5D and 4D in the streamwise and in the spanwise direction, respectively. The first row of turbines is placed at a distance of 5D from the entrance of the test domain.

Table 3.1 The values of C_T and C_T' (obtained from EPFL measurements) for the different rows in the wind farm case.

Case	T_1	T_2	T_3	T_4	T_5
C_T	0.5091	0.5601	0.6406	0.6116	0.5912
C_T'	0.7041	0.8099	1.0015	0.9286	0.8799
Case	T_6	T_7	T_8	T_9	T_{10}
C_T	0.6202	0.6109	0.5898	0.5926	0.5955
C_T'	0.9496	0.9269	0.8768	0.8831	0.8899

Figure 3.6 compares the normalized vertical profiles of the time-averaged streamwise velocity component and the turbulence intensity of the precursor domain LES results against the experimental findings of EPFL wind tunnel tests. The LES inflow profiles have a good qualitative agreement with the wind tunnel measurements, especially around the region of interest (the turbine rotor area). The apparent discrepancies are common when experimental flow conditions are being simulated to match the inflow profiles, and it has been addressed in many previous studies.

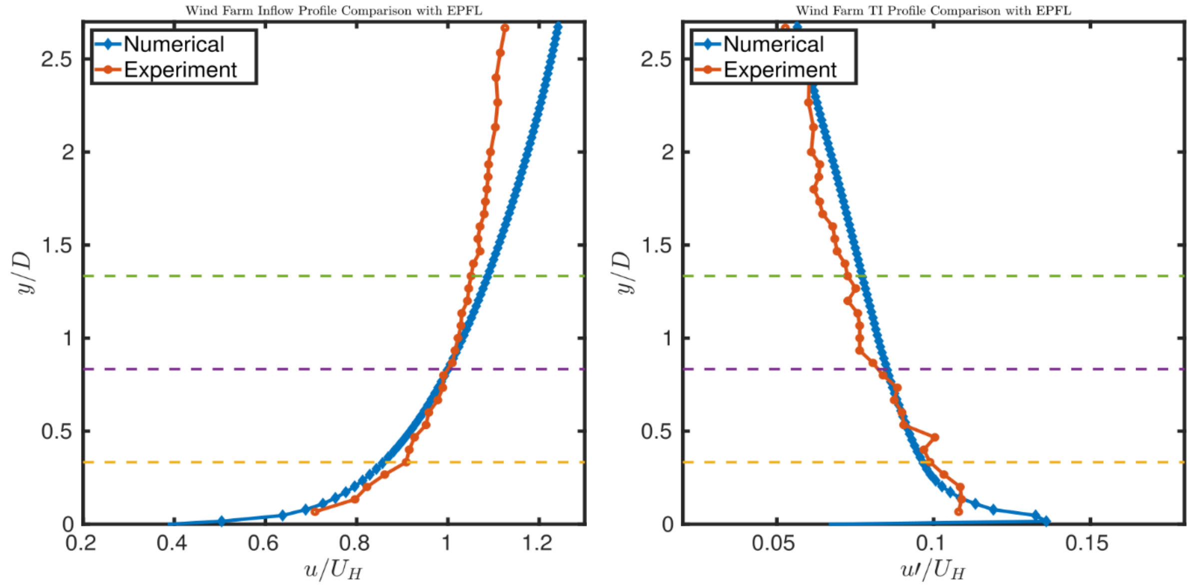

Figure 3.6. Inflow profiles of the velocity and the turbulent intensity compare against the experimental results of EPFL.

Figure 3.7 and Figure 3.8 depict the instantaneous flow field of the streamwise velocity component in a three-dimensional view incorporating three perpendicular slices and in the YZ plane sliced at hub height, respectively. They illustrate the flow field inside the wind farm and the interactions of wake structures behind the turbines. The time-averaged flow field of the streamwise velocity component is presented in Figure 3.9, Figure 3.10, and Figure 3.11, in a three-dimensional view that incorporates three perpendicular slices, in the YZ plane (sliced at hub height), and in the XY plane (slice at the rotor centerline in the middle column of turbines), respectively. How the wakes of upstream turbines are affecting the downstream turbines can be easily observed from these figures. More visualizations, including the turbulence intensity contours of the study, have been provided in the appendix section. They provide more insights into the characteristics of the wakes inside the wind farm.

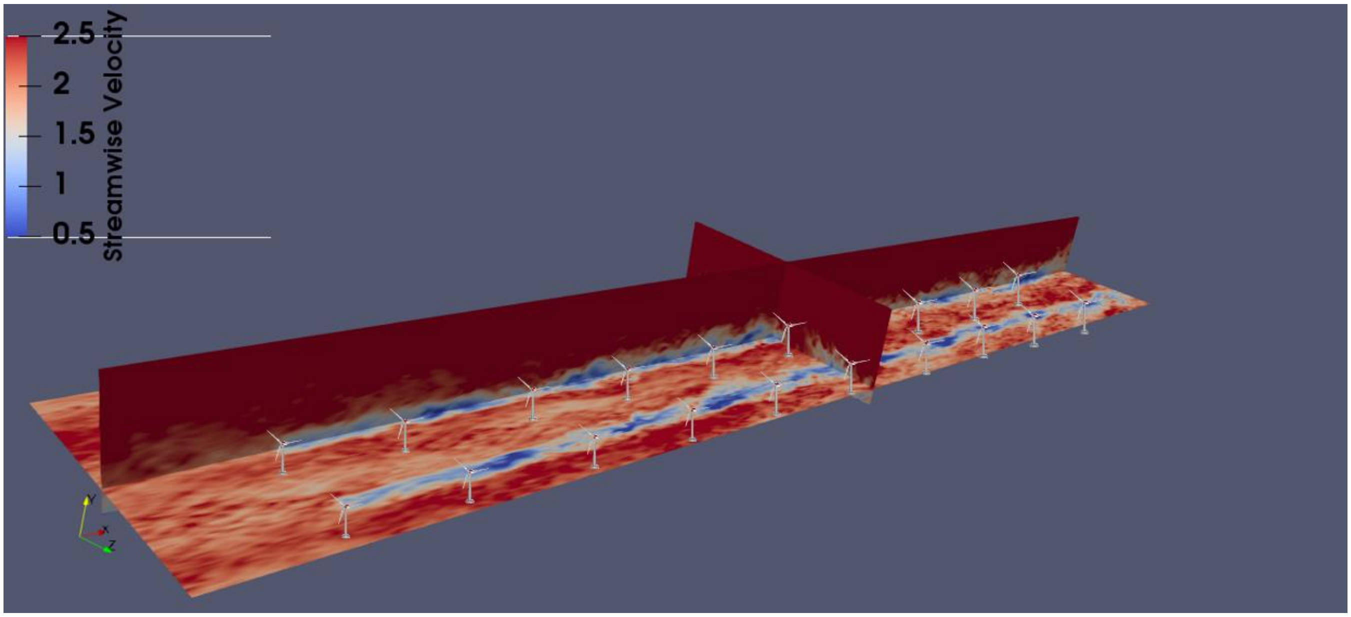

Figure 3.7. Illustration of the instantaneous flow field of the velocity deficit in a three-dimensional view.

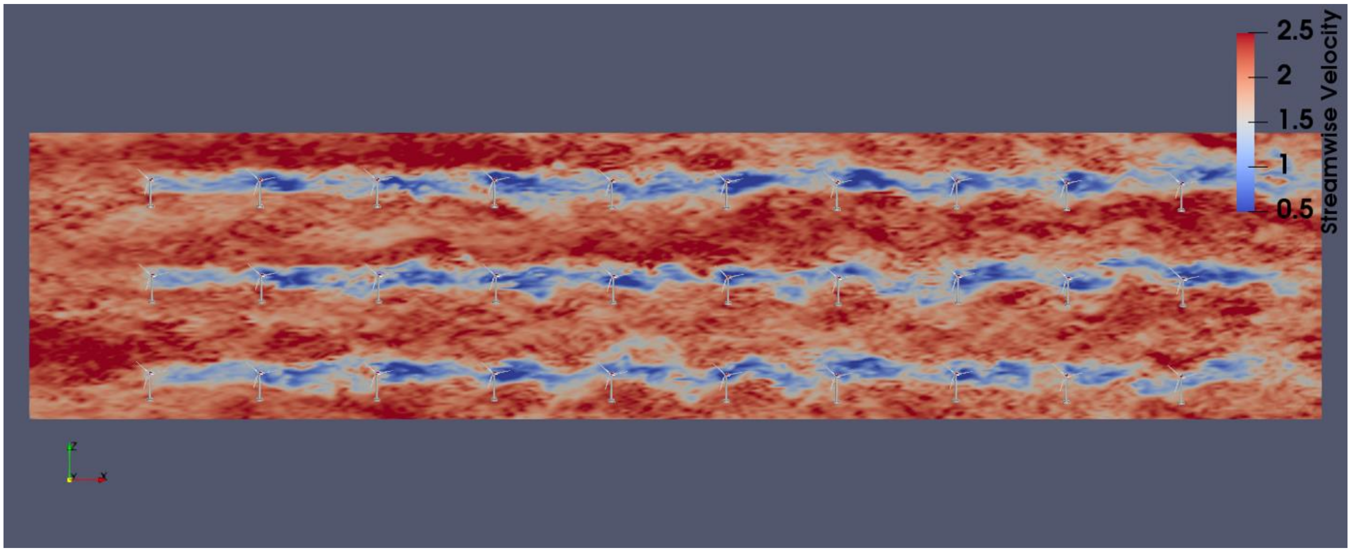

Figure 3.8. Contour of the instantaneous flow field of the velocity deficit in the streamwise direction on XZ plane.

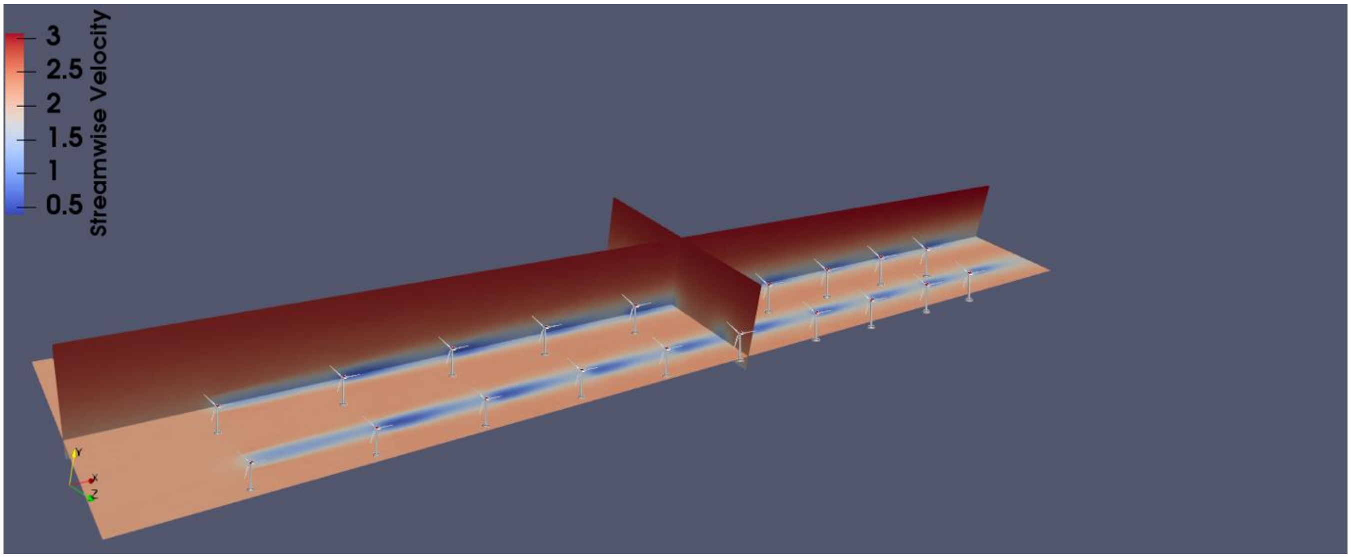

Figure 3.9. Representation of the time-averaged flow field of the velocity deficit in the 3D orientation.

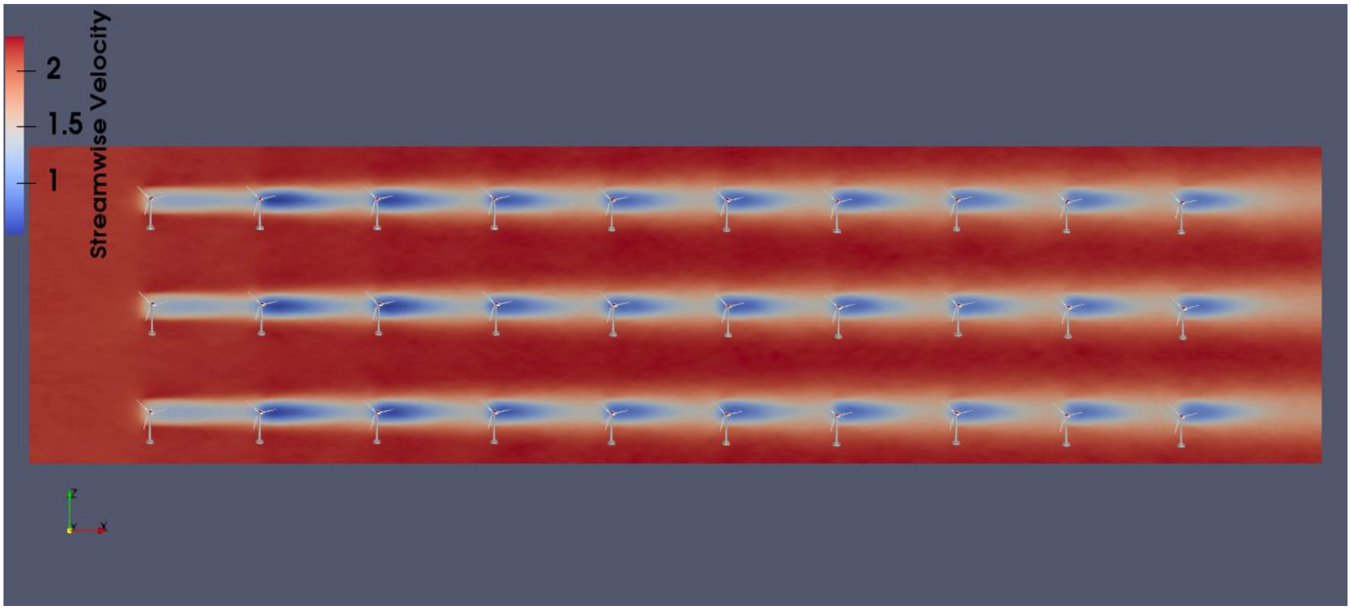

Figure 3.10. Representation of the time-averaged flow field of the velocity deficit in the XZ plane.

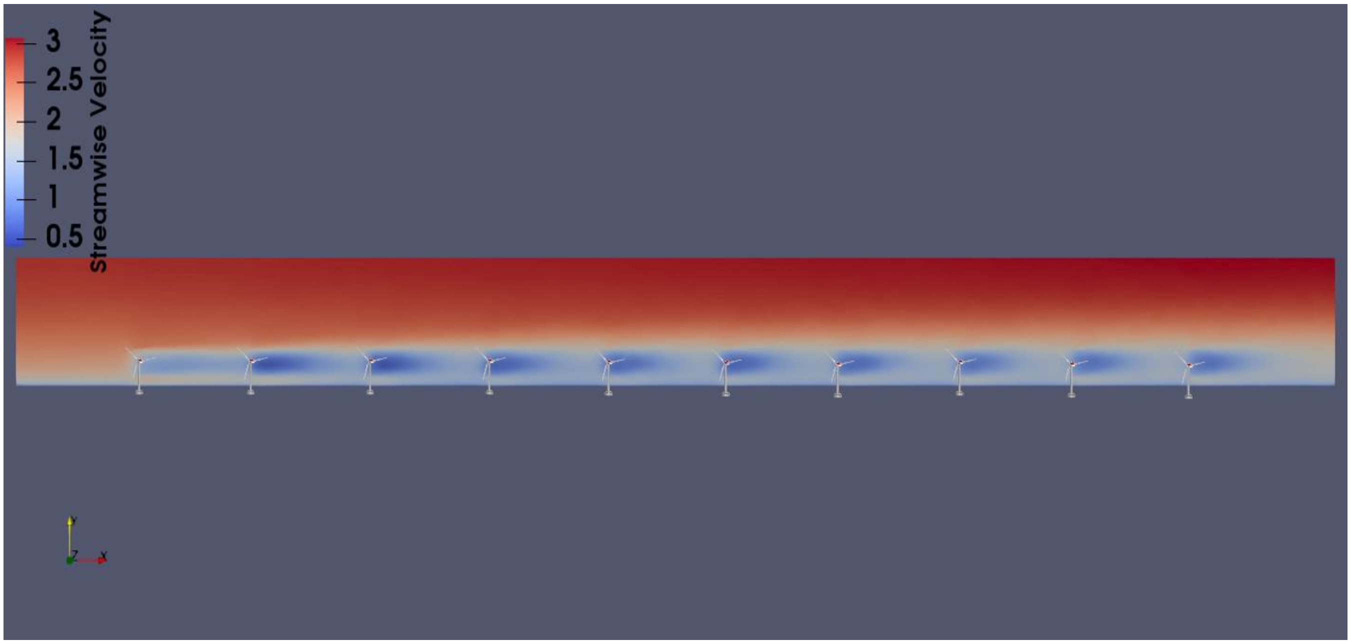

Figure 3.11. Representation of the time-averaged flow field of the velocity deficit in the XY plane.

Figure 3.12 and Figure 3.13 show vertical profiles of the time-averaged, resolved, streamwise velocity component (u) at various downstream sections (1D, 2D, 3D, and 4D). Figure 3.12 provides the velocity deficit profiles from the first five rows and Figure 3.13 provides the last five rows' velocity deficit profiles. The vertical height (Z) and velocity (u) have been normalized by the wind turbine diameter (D) and velocity at the hub height of the wind turbine (U_H), respectively. All the profiles indicate that the numerical results agree well qualitatively with the wind tunnel results, especially in the regions of interest (three horizontal purple lines where the wind turbine lies).

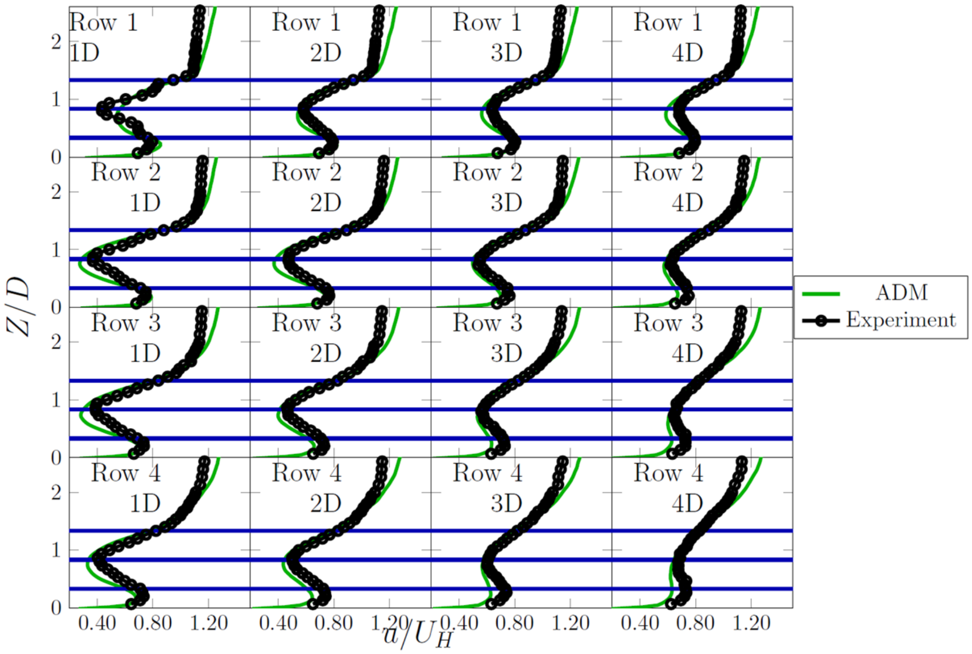

Figure 3.12. Comparison our wind farm simulation using actuator disk. It shows the mean streamwise velocity deficits (u/UH) at different downstream locations of the wind farm.

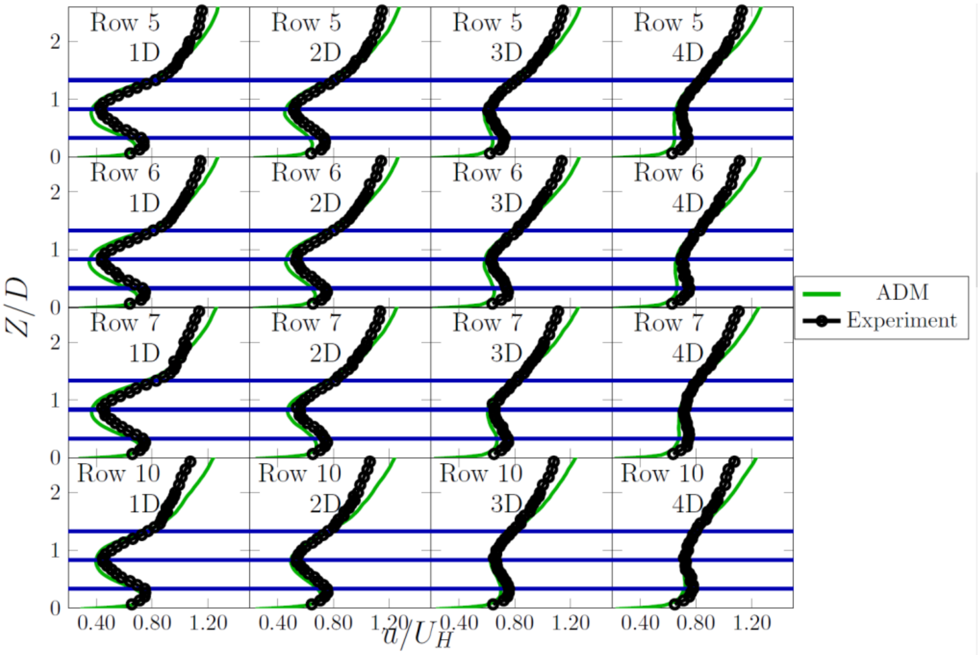

Figure 3.13. Comparison our wind farm simulation using actuator disk. It shows the mean streamwise velocity deficits (u/UH) at different downstream locations of the wind farm.

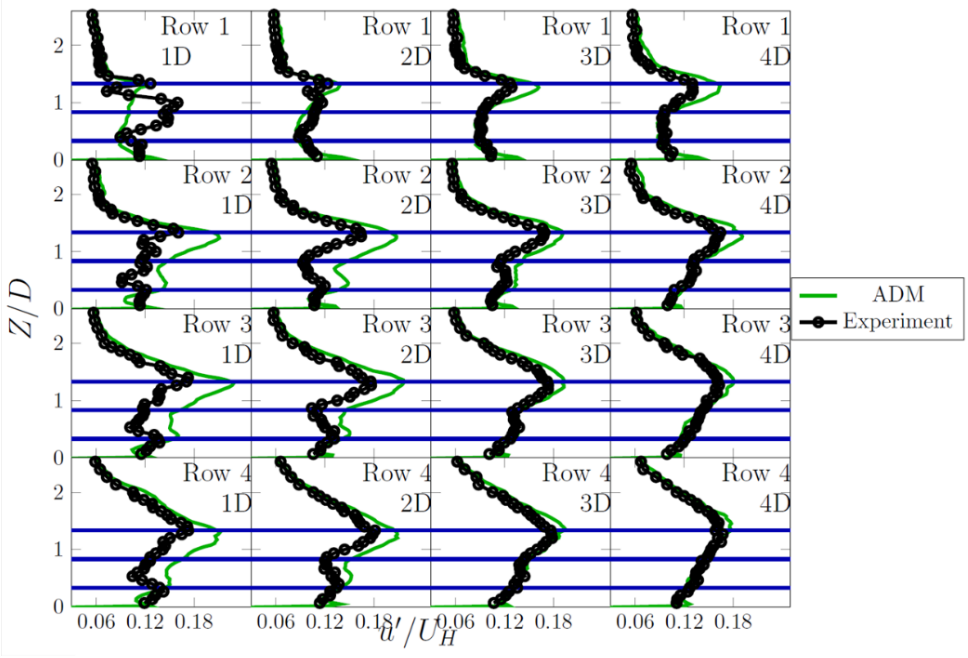

Figure 3.14. Comparison our wind farm simulation using actuator disk. It shows the turbulence intensity profiles (u'/U_H) at different downstream locations of the wind farm.

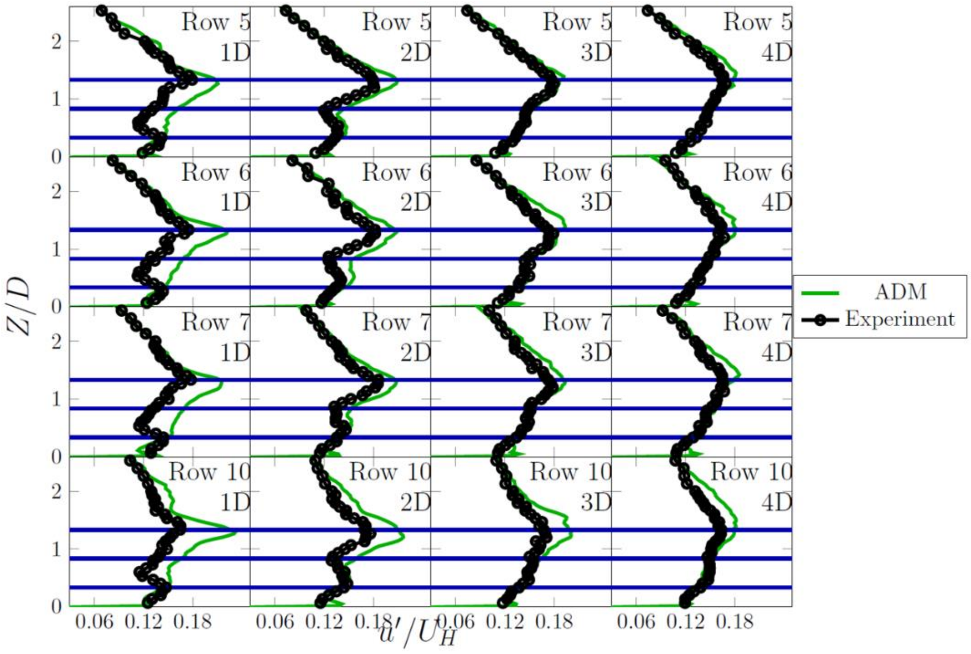

Figure 3.15. Comparison our wind farm simulation using actuator disk. It shows the turbulence intensity profiles (u'/U_H) at different downstream locations of the wind farm.

Figure 3.14 and Figure 3.15 compare the resolved streamwise turbulence intensity (I_x or u'/U_H), defined as the root-mean-square (RMS) of the resolved streamwise velocity fluctuation component divided by the hub height velocity (U_H), with the experimental results. The simulated vertical profiles of the turbulence intensity show a good qualitative agreement with the wind tunnel measurements, particularly in the far-wake regions. This is a common trend when wind turbines are modeled using the actuator disk method (ADM). Additionally, it's worth noting that the maximum turbulence intensity occurs at the top tip of the turbine, where the mean wind shear is high. The current simulations also accurately capture minimum and maximum turbulence intensity locations.

The region near the wind turbine blade is significantly affected by blade aerodynamics, tip vortices, as well as the tower and nacelle. However, these influences are negligible in the far wake region. Therefore, numerical results show better agreement with experimental results, although there are slight deviations compared to the total velocity profile deficit. If the tower and nacelle effects were included in the ADM model, the results would show better agreement with the wind tunnel measurements. We plan to incorporate these features into our solver in the future.

3.4 Yaw Implementation Validation

To assess the effectiveness of the yaw implementation in generating the wake characteristics at various downstream locations, a series of validations have been carried out.

The validity of the yaw implementation has been verified for both utility-scale and miniature turbines, based on both experimental and computational results.

3.4.1 Utility Scale Size

For the utility-scale run, the dimensions are (Lx=2000.0 m, Ly=400.0 m, Lz=700.0 m), grid points are (Nx=200, Ny=40, Nz=70), hub height = 70.0m, diameter = 60.0m. For this current run, the friction velocity (u*) is 0.4 ms^{-1}, the surface roughness (y0) is 0.1m, and the thrust coefficient (C_T) is 0.8. Figure 3.16 shows the comparison of wake profiles against Jimenez et al. [19] for a yaw angle of 30°. The contour plot for the yawed wake velocity is depicted in Figure 3.17. The wake profiles match quite well, even at different downstream positions.

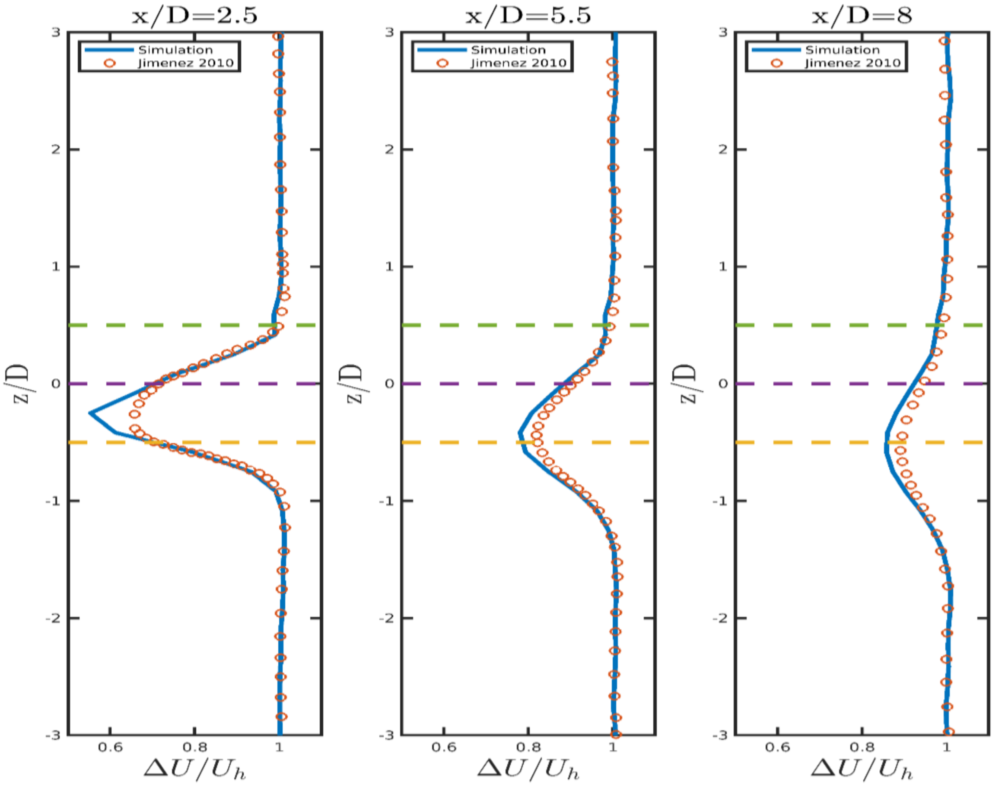

Figure 3.16. Comparison of yawed wake profiles for yaw angle of 30° against Jimenez et al. at different downstream positions.

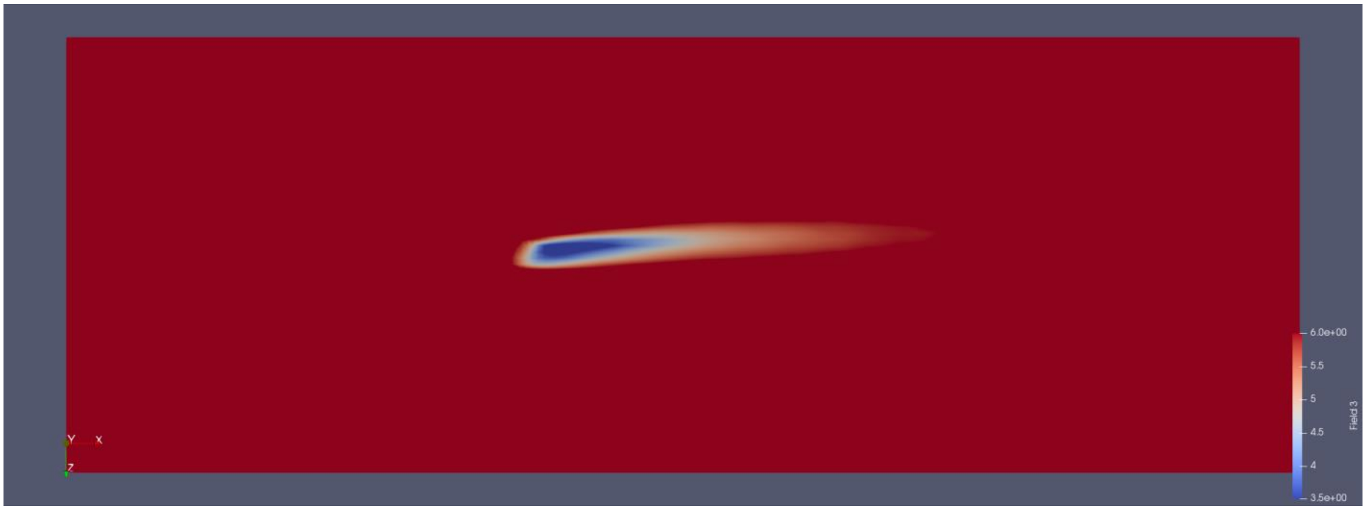

Figure 3.17. Velocity contour of yawed wake for a yaw angle of 30°.

3.4.2 Miniature Scale Size

For the miniature-scale run, the dimensions are (Lx = 3.2 m, Ly = 0.4 m, Lz = 0.8 m), grid points are (Nx = 128, Ny = 32, Nz = 64), hub height = 0.125 m, diameter = 0.15 m. For the current run, the friction velocity (u^*) is 0.226 ms^{-1}, the surface roughness (y_0) is 0.022 mm, and the thrust coefficient (C_T) is 0.66. The yawed wake profiles are compared against both the experimental findings [20] and the simulated (Yawed ADMR and Yawed ADM) results [21]. The yawed wake profiles in Figure 3.18 and the yawed turbulent intensity profiles in Figure 3.19 are in close agreement with both the experimental and the numerical results. The apparent minimum discrepancies are due to the absence of the turbine tower and rotation of the turbine implementation in our actuator disk model (ADM). In such cases, the slightest mismatch is common when ADM is numerically modeled.

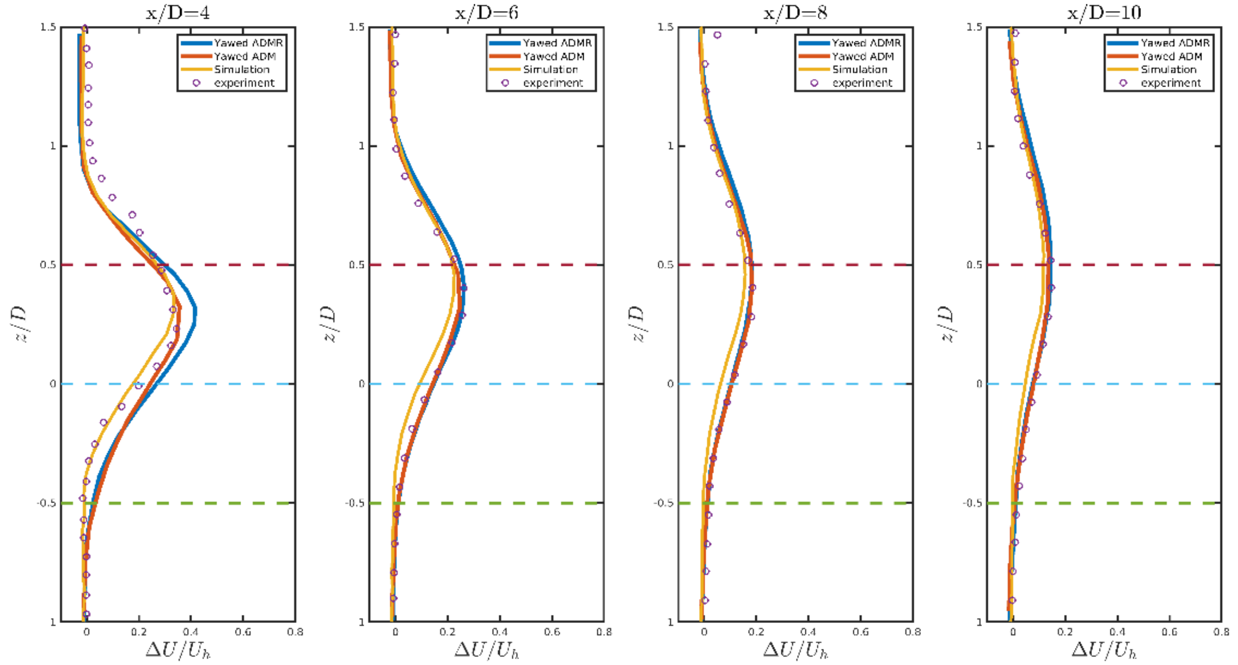

Figure 3.18. Comparison of yawed velocity deficit profiles against experiment and other published numerical results

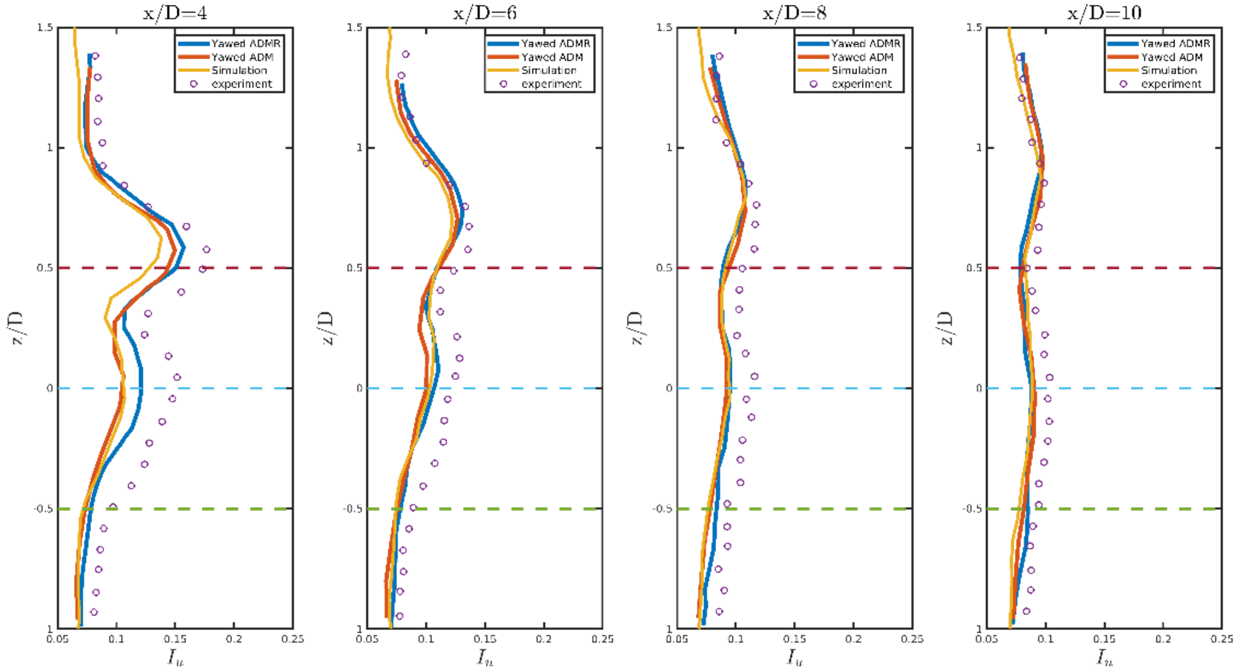

Figure 3.19. Comparison of yawed turbulent intensity (TI) profiles against experiment and other published numerical results.

3.5 Conclusion

All the statistics relevant to LES simulation, wind turbines, and wind farms are validated against benchmarked results. Overall, our simulated results show a good qualitative agreement with theoretical predictions, validated computational findings, and wind tunnel observations for all the velocity deficit and turbulence intensity profiles, indicating the accuracy and validity of our simulations. Despite some slight discrepancies between the simulated and experimental outcomes, the majority of the boundary layer closely resembles each other, especially around the rotor area. This finding suggests that the WIND4D solver is a reliable tool for investigating the physics of wind turbines and wind farms. Therefore, this study highlights the potential of the WIND4D solver for further research in the field of wind energy.

Chapter 4

EXPLORING THE ROLE OF GROUND PROXIMITY IN TURBINE WAKE BEHAVIOR

4.1 Introduction

The gap between the ground and a wind turbine is a crucial factor that affects its performance and environmental (local microclimate) impact. When we talk about how the distance between the bottom edge of the turbine and the ground affects the wake, we are referring to the ground effect and how it influences wake turbulence. The wake is the turbulent air that forms behind the turbine as it extracts energy from the wind.

When a turbine blade comes closer to the ground, the ground effect becomes more noticeable. Ground effect refers to the changes in airflow that occur around an object, like a turbine blade, when it is close to the ground. This can create greater turbulence and altered wake patterns, particularly near the ground.

When a turbine is closer to the ground, the turbulence it creates interacts more closely with the ground. As a result, the wake may break up and dissipate more quickly than if the turbine were situated at a higher position. However, any obstacles or roughness on the ground can intensify the turbulence and make the wake last longer and become more chaotic. At higher altitudes, there may be improved vertical mixing of the wake due to atmospheric turbulence, resulting in faster wake recovery. The mixing process is more aggressive when there's higher turbulence (higher TI) in the wake. This phenomenon refers to the process by which the decelerated air in the wake is replenished with relatively faster-moving air from the surrounding environment at an expedited rate. As a consequence, the wake reverts to its undisturbed, natural state at an accelerated pace.

The reduction in wind speed, also known as velocity deficit, in the wake of a turbine is influenced by its proximity to the ground. A wind turbine positioned closer to the ground may cause a more significant reduction in wind speed near the surface, which can affect the performance of downwind turbines in a wind farm.

The nature of the ground surface can affect wake behavior, with rougher surfaces increasing turbulence. These effects can be more pronounced when the turbine is closer to the ground. The movement of the turbine blade creates a vortex at the tip. When the blade is closer to the ground, the vortex interacts with the ground, affecting its strength and turbulence. The temperature and stability of the air can be impacted by the ground. During the night, the ground cools faster than the air, causing a stable layer of air close to the ground. This stable layer can affect turbulence and wake behavior. The proximity of the turbine blades to this layer can influence the characteristics of the wake.

Wind turbines in close proximity can affect each other's performance and lifespan, with turbines positioned closer to the ground producing wakes that impact other turbines differently compared to higher-positioned turbines. When planning a wind farm and determining the best placement for turbines, it is important to take into account the impact of wake effects, particularly in relation to the ground. By doing so, it is possible to optimize the arrangement of turbines to maximize energy production and minimize wear and tear. Accurate computational models and wind tunnel tests are often utilized to predict and better understand these effects in detail.

The impact of the gap between the turbine's lower edge and the wall on wake recovery remains underexplored within the proper framework of Large Eddy Simulation (LES). Previous studies have mainly used analytical methods, such as the greedy search algorithm combined with the Jensen model, as described by Chen et al. [22]. Wang et al. [23] compared various analytical approaches, such as Park, Larsen, and B-P models. Stanley et al. [24] analytically found that using two varied hub heights optimized performance in densely packed wind turbines with smaller diameters in low wind shear conditions. Vasel-Be-Hagh and Archer [25] compared one case optimized analytically with LES findings. A LES study [26] discovered that large-scale structures from bigger wind turbines positively influence smaller turbines with low hub heights.

To the best of the authors' knowledge, no distinctive studies have rigorously examined the role of ground proximity in turbine wake behavior using a comprehensive numerical framework to analyze wind turbine wakes. The primary objective of this research is to provide a deeper understanding of the influence of the gap between the lower edge of the turbine and the ground on the overall dynamics and characteristics of the wake. The chapter is organized into three sections. Section 4.2 provides a detailed explanation of the case setup applied in the study. In Section 4.3, the results are presented and analyzed. Finally, Section 4.4 offers a brief summary of the entire analysis. The findings of this case study were presented in the APS-DFD meeting [7].

4.2 Case Set-Up

The turbine is positioned 4.0D downstream from the inflow plane, right in the middle of the spanwise direction. The domain has the following dimensions: Lx0 ≈ 24.0D, Lx1 ≈ 16.0D, Ly ≈ 8.0D, and Lz ≈ 16.0D, all in terms of the rotor diameter. The number of grid points corresponds to Nx0 = 300, Nx1 = 200, Ny = 100, and Nz = 200, resulting in a uniform grid size of dx = dy = dz = 10 m in every direction. For these case studies, we used a neutral atmospheric boundary layer without any Coriolis force. The friction velocity (u^*) is 0.45 ms^{-1}, the surface roughness (y_0) is 0.1 m, C_T' is $\frac{36}{31}$. Table 4.1 provides the relevant parameters for the two cases. The schematic of the domain setups with their relevant dimensions is illustrated in Figure 4.1.

Table 4.1. Different parameter values for the two cases.

Case	Rotor Diameter, D	Hub Height, H	Gap
Case 1	126m	90m	0.25D or 27m
Case 2	126m	103.5m	0.35D or 40.5m

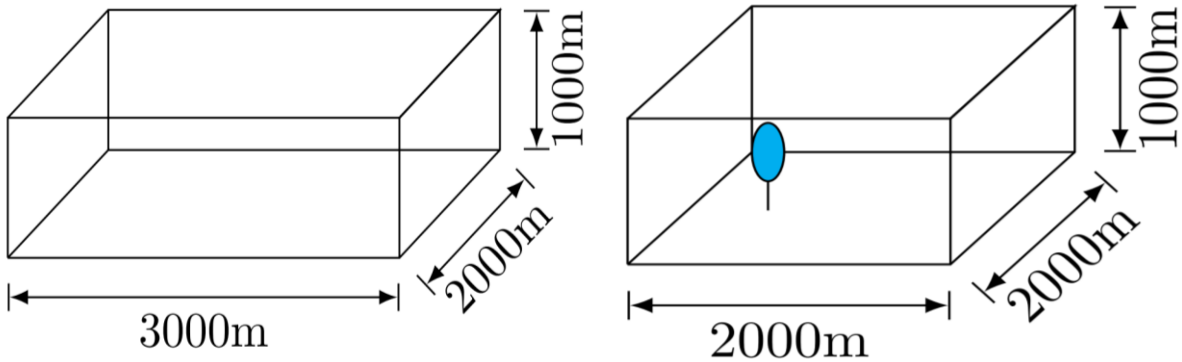

Figure 4.1. Schematic of the computation domain consisting of a precursor domain and a test domain with all the dimensions relevant to this case study.

4.3 Results and Discussion

The subsequent sections systematically present and analyze the study's results to facilitate a comprehensive understanding. First, we present and analyze the flow field statistics through detailed contours and profiles. Then, we provide an interpretation of the turbulence intensity profiles.

4.3.1 Analysis of the Flow Field Contours and the Profiles

Figure 4.2 and Figure 4.3 display the instantaneous contours of streamwise velocity in the XY plane for the cases of 0.25D and 0.35D cross-sections taken at the turbine's centerline, respectively. The contours show that there is more momentum flux passing through the gap for the 0.35D case compared to the 0.25D case. This means that there is greater motion or kinetic energy being conveyed through the clearance region of the turbine edge and the ground surface. The smaller gap leads to more ground interactions, resulting in a complex wake pattern compared to the larger gap.

As the mixing process continues, the slower wind speeds in the center of the wake, known as the "velocity deficit", become "diluted" or "averaged out" with the faster-moving air being mixed in. This gradual process increases wind speeds within the wake, bringing them closer to the undisturbed wind speeds outside of the wake.

As we move higher above the ground, the wind speed tends to increase. This variation in wind speed across different vertical levels is known as wind shear. Turbines that have a greater distance between their rotor blades will operate in a larger part of this wind shear layer. This can have an impact on turbulence and wake dynamics, affecting the overall performance of the turbines. So, the turbine with a larger gap between the lower edge and the ground will experience low wind shear but higher mean wind speeds than the turbine with a smaller gap.

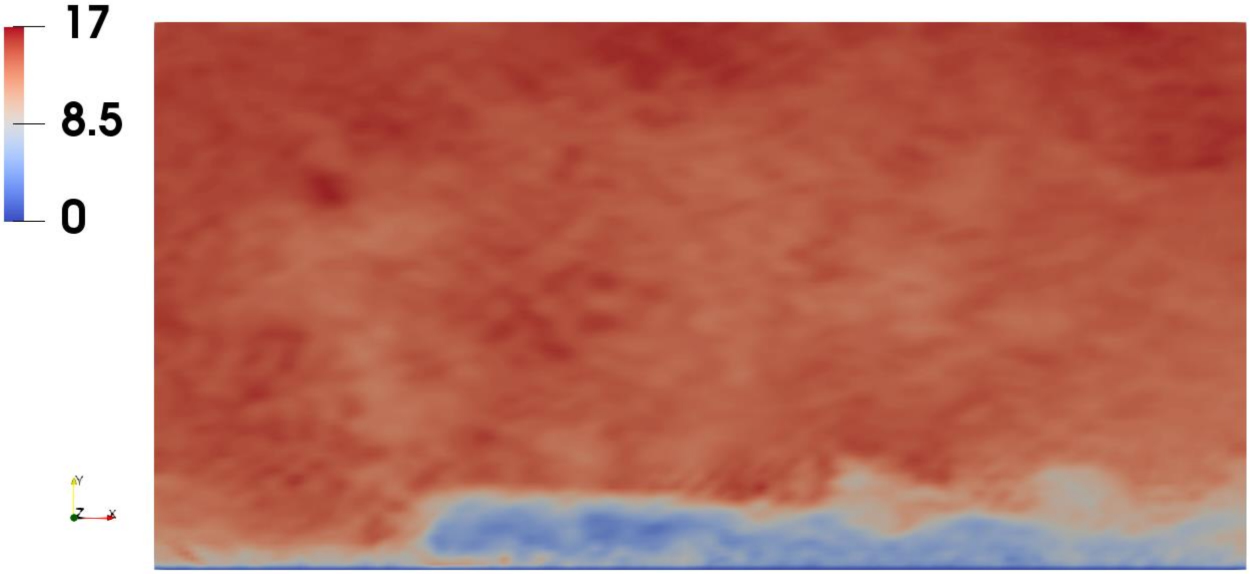

Figure 4.2. Instantaneous contour of streamwise velocity in the XY plane for gap 0.25D cross-sectioned at the centerline of the turbine.

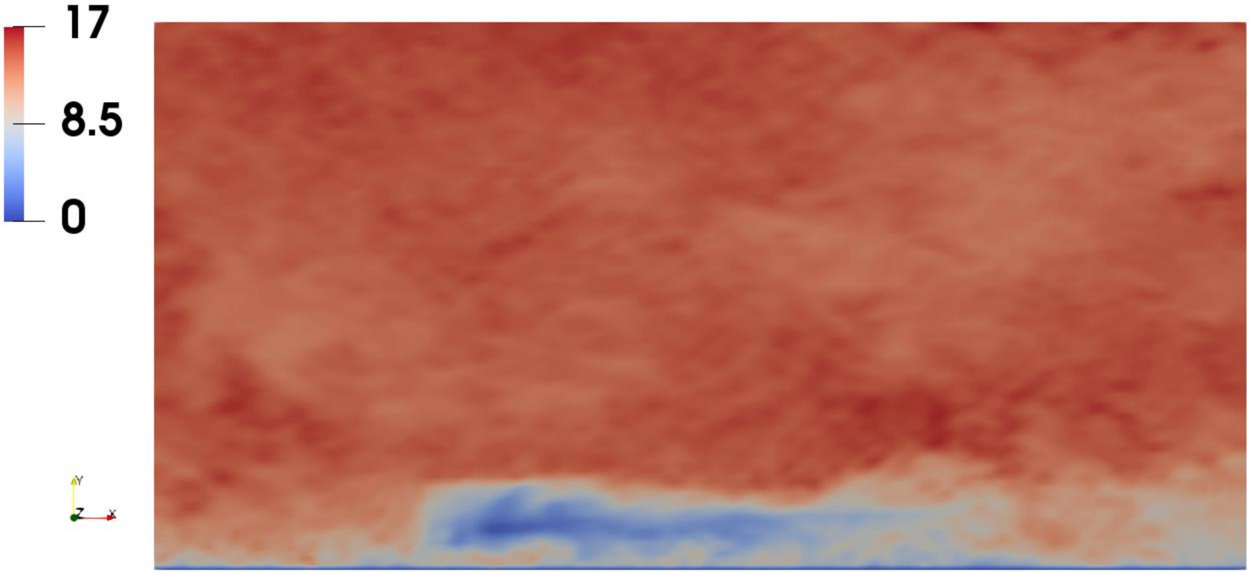

Figure 4.3. Instantaneous contour of streamwise velocity in the XY plane for gap 0.35D cross-sectioned at the centerline of the turbine.

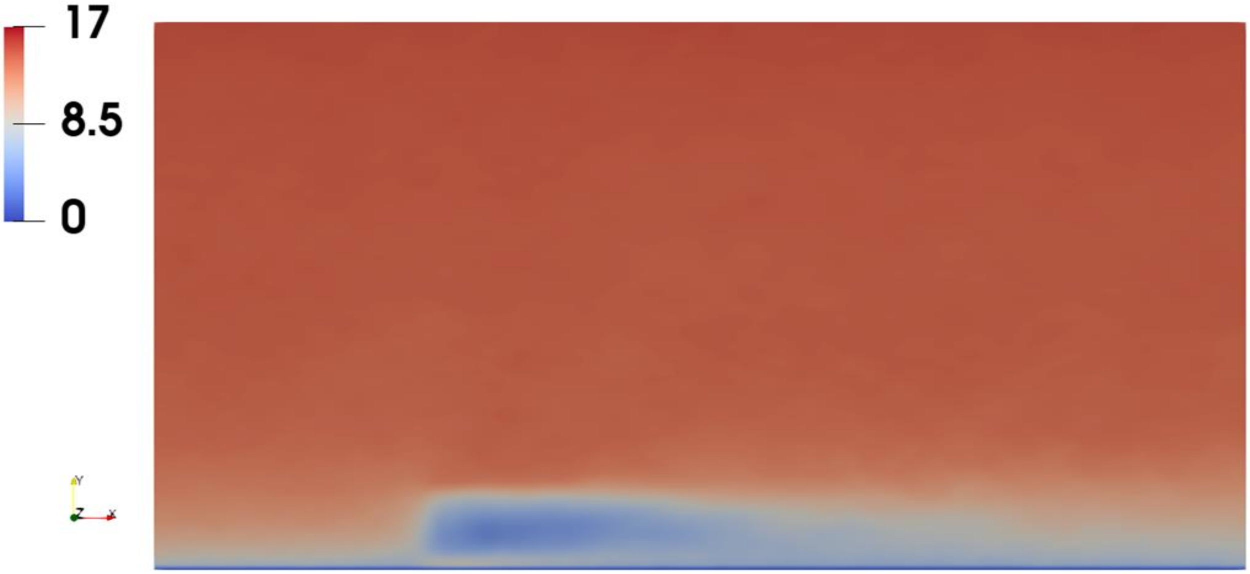

Figure 4.4. Time-averaged contour of streamwise velocity in the XY plane for gap 0.25D cross-sectioned at the centerline of the turbine.

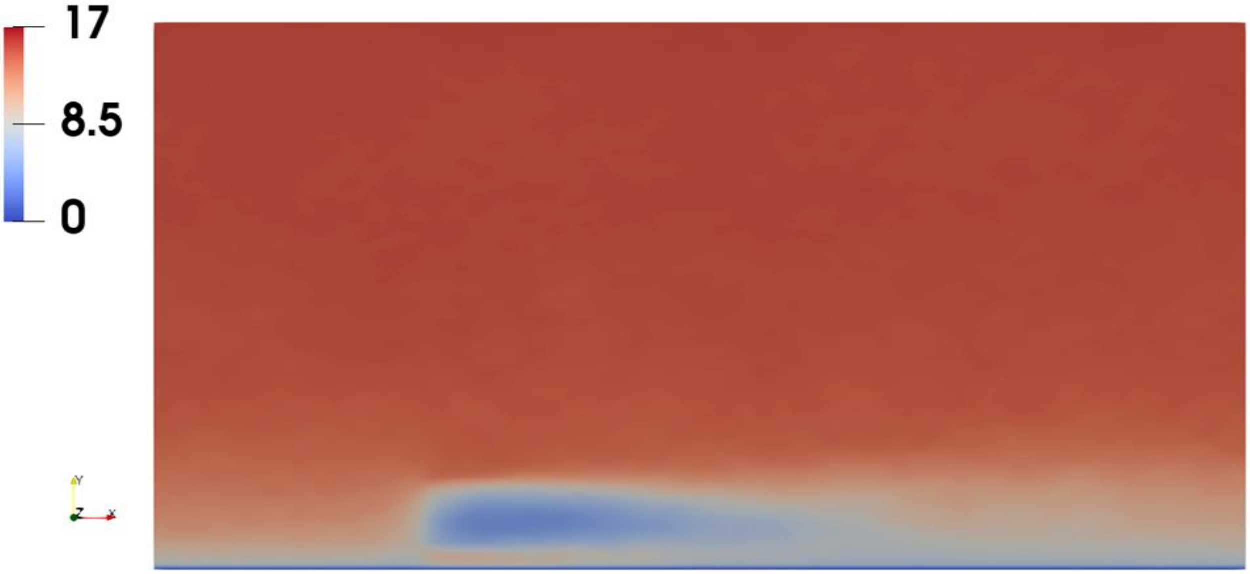

Figure 4.5. Time-averaged contour of streamwise velocity in the XY plane for gap 0.35D cross-sectioned at the centerline of the turbine.

The efficiency of wind farms in harnessing wind from higher altitudes is an important research area. The clearance between the turbine's lower edge and the ground plays a crucial role in this regard. Notably, a larger gap between the turbine and the ground facilitates higher vertical transport of momentum than a smaller gap. Additionally, the vertical kinetic energy flux, which channels high-velocity wind from above the wind farm down to the hub-height level, is more effective when there is a larger gap between the turbine and the ground. This results in a more pronounced magnitude of kinetic energy transfer, enabling a more efficient harnessing of wind from higher altitudes.

The time-averaged representations of the streamwise velocity contours in the XY plane for the 0.35D and 0.25D cases are depicted in Figure 4.4 and Figure 4.5, respectively. These contours have been cross-sectioned at the centerline of the turbine. From analyzing the contour plots of the average flow field, it is evident that the 0.35D case has a higher momentum flux flowing through the gap compared to the 0.25D case. The figures also highlight that the wake in the 0.25D case persists for a longer distance than the 0.35D case. When wind turbines have a smaller gap, the ground effect plays a more significant role in impacting their wakes. The ground acts as a barrier, hindering the vertical mixing of the wake with the free-flowing air above, leaving a larger area of slow-moving air closer to the ground. Turbulent mixing is crucial for wake recovery. In the case of a larger gap, there is more room for turbulent eddies to mix the slowed-down wake with the faster-moving air from above. However, in the case of a smaller gap, the vertical mixing is limited, leading to slower wake recovery.

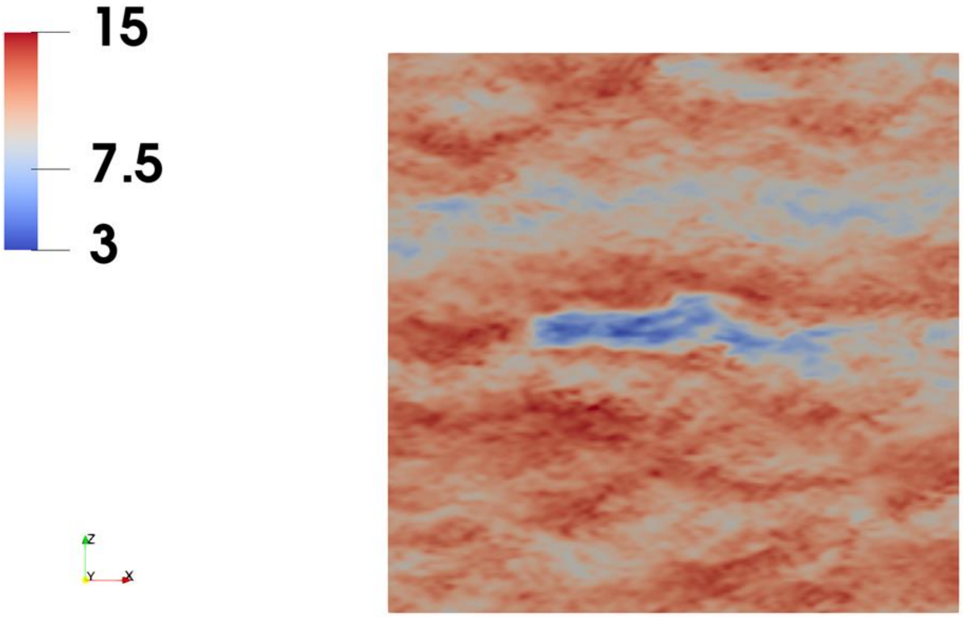

Figure 4.6. Instantaneous contour of streamwise velocity in the XZ plane for gap 0.25D cross-sectioned at the centerline of the turbine at hub height.

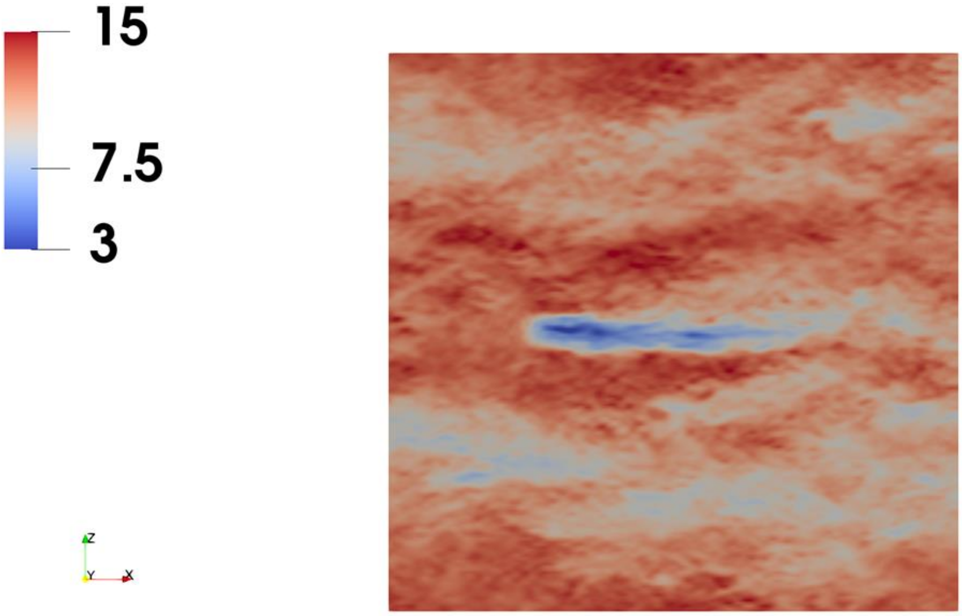

Figure 4.7. Instantaneous contour of streamwise velocity in the XZ plane for gap 0.35D cross-sectioned at the centerline of the turbine at hub height.

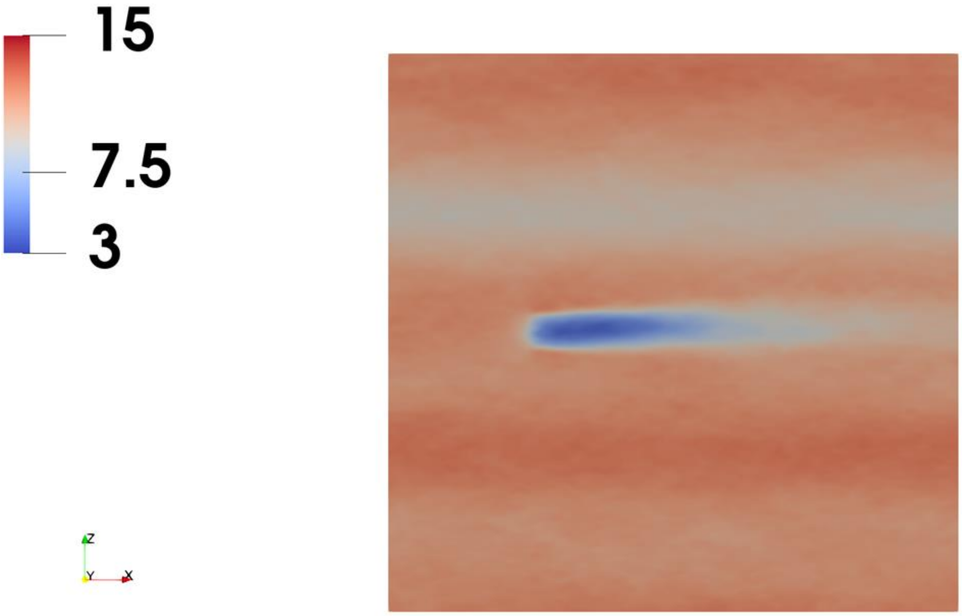

Figure 4.8. Time-averaged contour of streamwise velocity in the XZ plane for gap 0.25D cross-sectioned at the centerline of turbine at hub height.

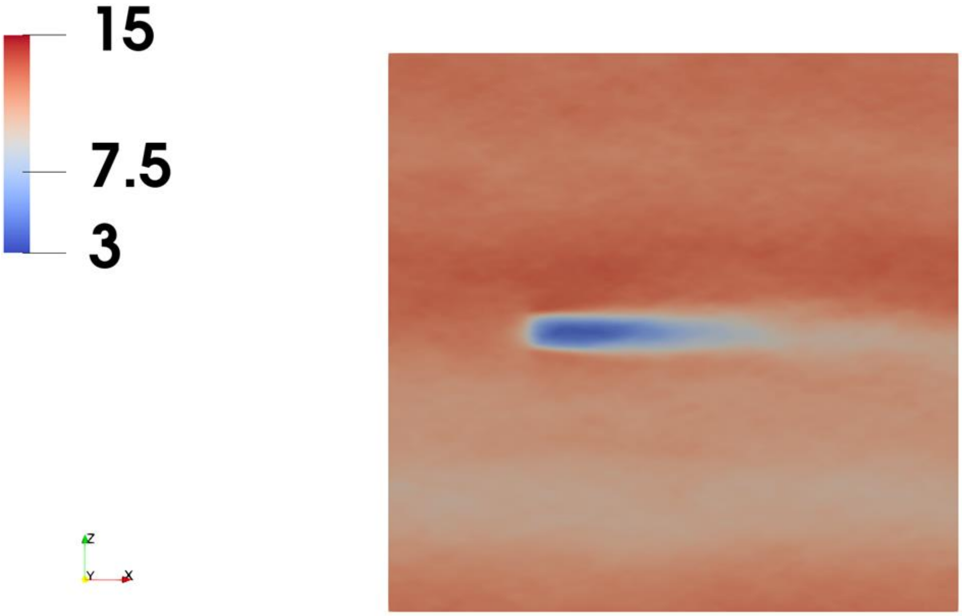

Figure 4.9. Time-averaged contour of streamwise velocity in the XZ plane for gap 0.35D cross-sectioned at the centerline of turbine at hub height.

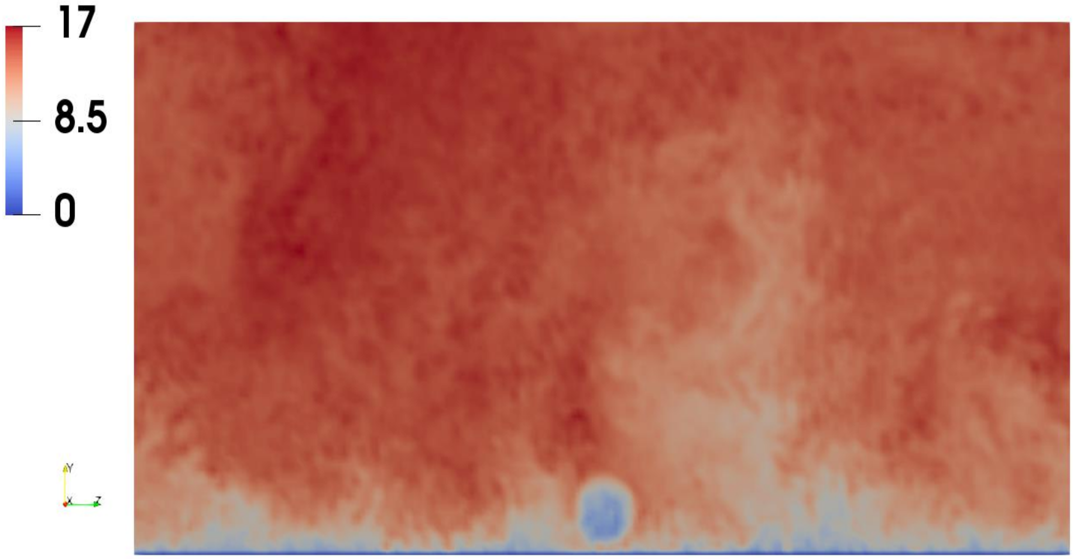

Figure 4.10. Instantaneous contour of streamwise velocity in the YZ plane for gap 0.25D cross-sectioned at the location of turbine.

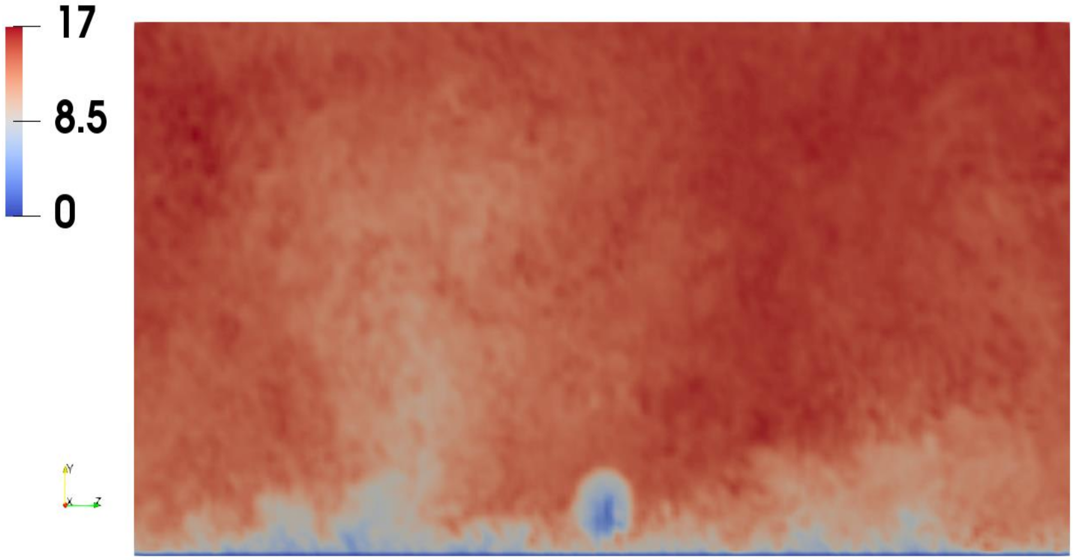

Figure 4.11. Instantaneous contour of streamwise velocity in the YZ plane for gap 0.35D cross-sectioned at the location of turbine.

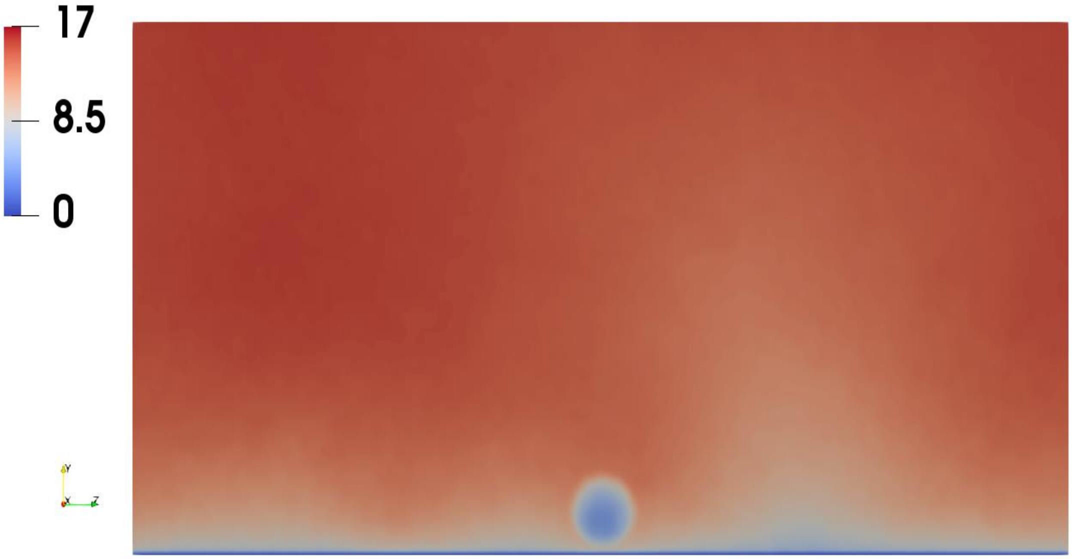

Figure 4.12. Time-averaged contour of streamwise velocity in the YZ plane for gap 0.25D cross-sectioned at the location of turbine.

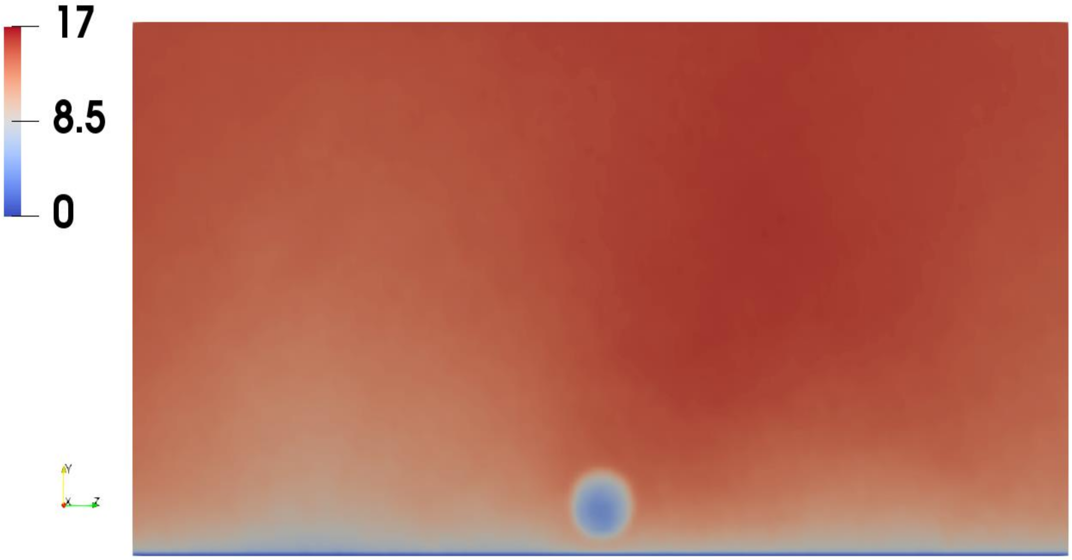

Figure 4.13. Time-averaged contour of streamwise velocity in the YZ plane for gap 0.35D cross-sectioned at the location of turbine.

The streamwise velocity contours for the 0.25D and 0.35D gaps in the XZ plane at the hub height centerline of the turbine are shown in Figure 4.6, Figure 4.7, Figure 4.8, and Figure 4.9, both instantaneous and averaged. The contours provide more information about the wake structures and their interaction with the flow downstream. They also indicate that the length and width of the wake are smaller when the ground clearance is larger compared to when it is smaller.

Figure 4.10 to Figure 4.13 depict the instantaneous and averaged streamwise velocity contours for the 0.25D and 0.35D gaps at the rotor plane of the turbine in the YZ plane. They display wake interactions from the side and ground clearance in each case, along with the shape of the rotor-shaped velocity deficit.

Figure 4.14 and Figure 4.15 display the vertical wake profiles for gaps of 0.25D and 0.35D, respectively, at various downstream positions. The plots show greater acceleration of velocity through the gap for the 0.35D case compared to the 0.25D case. It is noticeable that the wind shear is stronger in the wake area for the bigger gap when compared to the smaller gap. This increased wind shear causes more turbulence in the wake region behind the turbine, resulting in a faster recovery of the velocity deficit.

Figure 4.16 and Figure 4.17 at various downstream positions show the lateral wake profiles at the hub height for gaps of 0.25D and 0.35D, respectively. The plots demonstrate that the velocity outside the rotor plane is more accelerated for the 0.35D case than the 0.25D case. The plotted data indicates that an increase in ground clearance leads to a decrease in the dimensions of the wake, specifically the length and width.

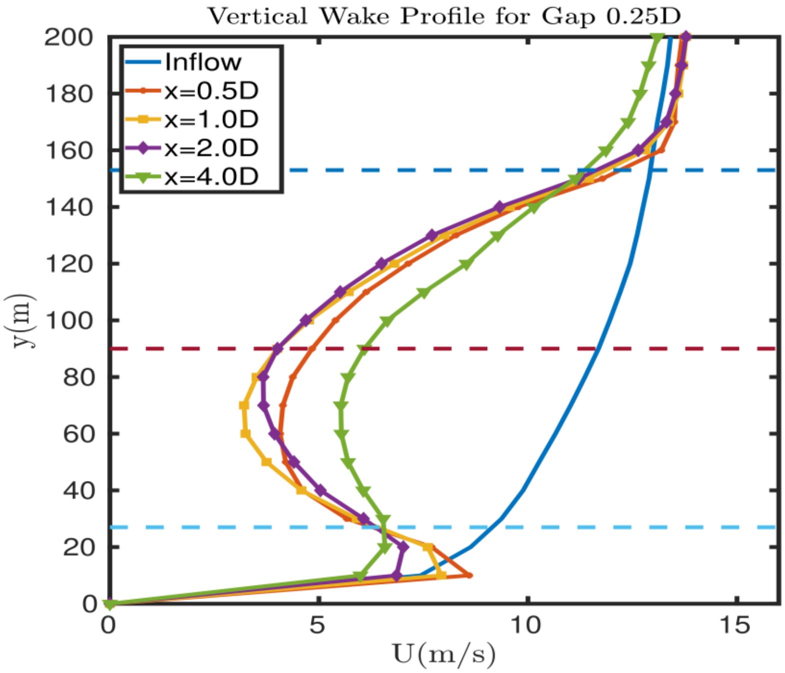

Figure 4.14. Comparison of the vertical wake profile at different downstream positions for a gap of 0.25D, calculated at the centerline of the turbine.

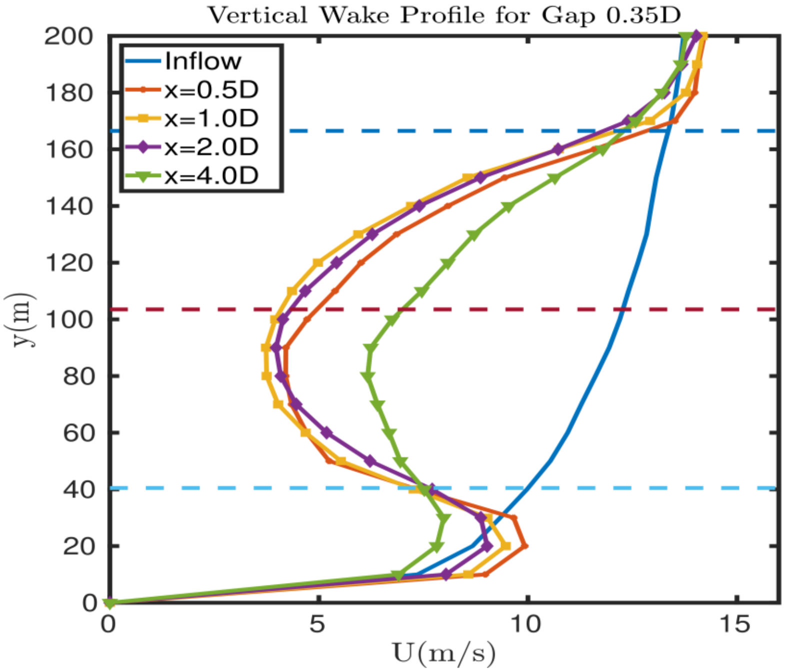

Figure 4.15. Comparison of the vertical wake profile at different downstream positions for a gap of 0.35D, calculated at the centerline of the turbine.

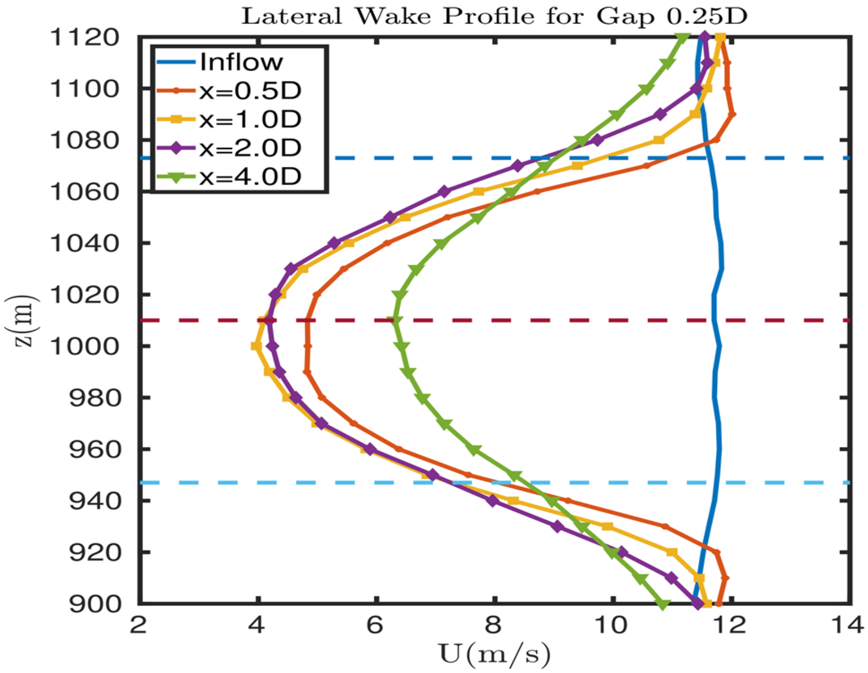

Figure 4.16. Comparison of the lateral wake profile for gap 0.25D at different downstream positions at the hub height of a turbine.

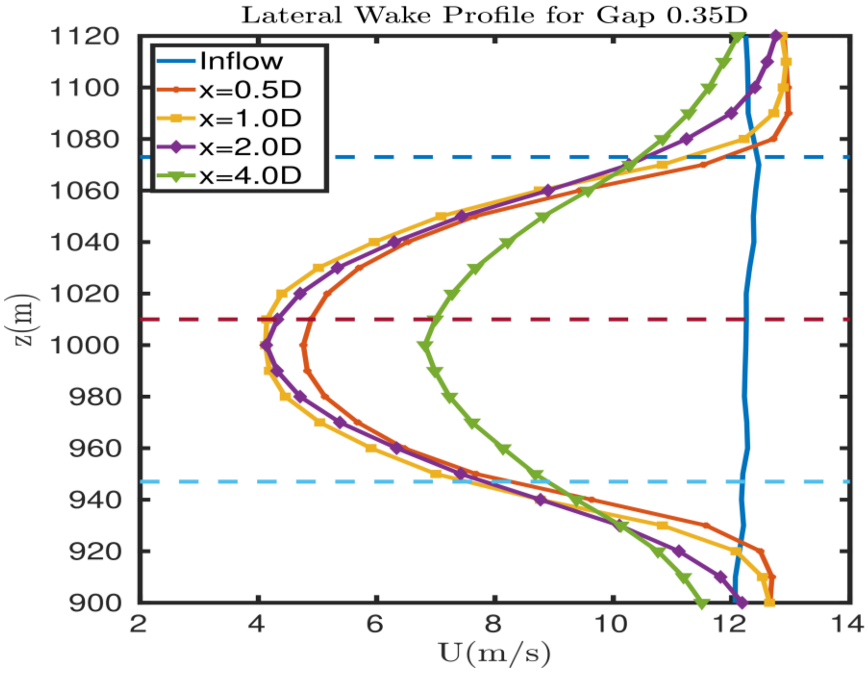

Figure 4.17. Comparison of the lateral wake profile for gap 0.35D at different downstream positions at the hub height of a turbine.

4.3.2 Analysis of the Turbulent Intensity Profiles

Figure 4.18 and Figure 4.19 illustrate the comparison of the vertical turbulent intensity (TI) profiles at different downstream positions for the cases of 0.25D and 0.25D, calculated at the centerline of the turbine. The plots indicate that the 0.35D case exhibits a higher turbulence intensity than the 0.25D case. This suggests that the wake of the former case is recovered faster. A wake with higher turbulence intensity tends to recover faster because the turbulence promotes mixing with the surrounding air. When the wake mixes with the freestream wind (undisturbed wind), it dilutes the wake's velocity deficit, leading to a faster return to a natural state. The turbulence in the wake actively mixes with the surrounding air by pulling in faster-moving air from the edges to its slower-moving center through swirling eddies.

Wind speed usually increases with height above the ground due to surface roughness and other ground-based obstructions. When there is a larger gap, the upper sections of the rotor can access these higher wind speeds. This leads to increased turbulence, promoting better mixing and faster wake recovery. On the other hand, a smaller gap means the entire rotor operates closer to the ground in a region of reduced wind speeds and potentially less turbulence.

Figure 4.20 and Figure 4.21 show lateral turbulent intensity (TI) profiles at different downstream positions, calculated at the turbine's hub height, for two cases: 0.25D and 0.25D. Comparing the 0.35D and 0.25D cases, the lateral profiles also indicate higher turbulence intensity (TI) for the former.

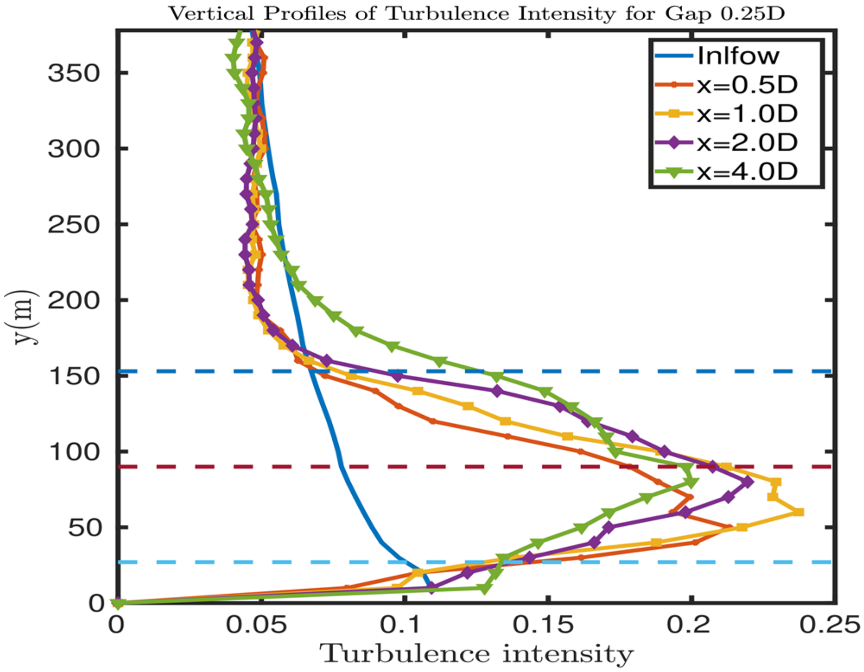

Figure 4.18. Vertical turbulence intensity profile comparison for gap 0.25D at different downstream positions.

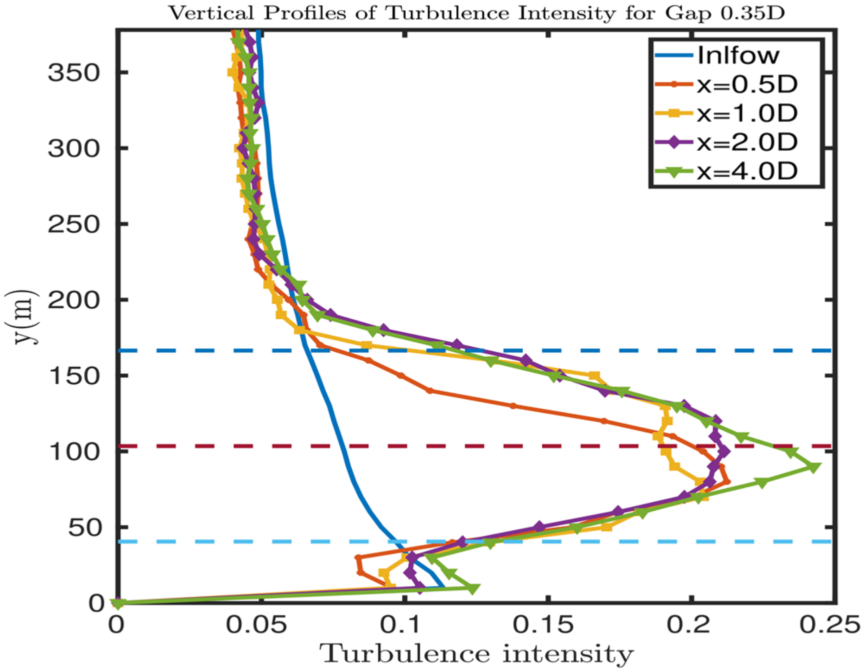

Figure 4.19. Vertical turbulence intensity profile comparison for gap 0.35D at different downstream positions.

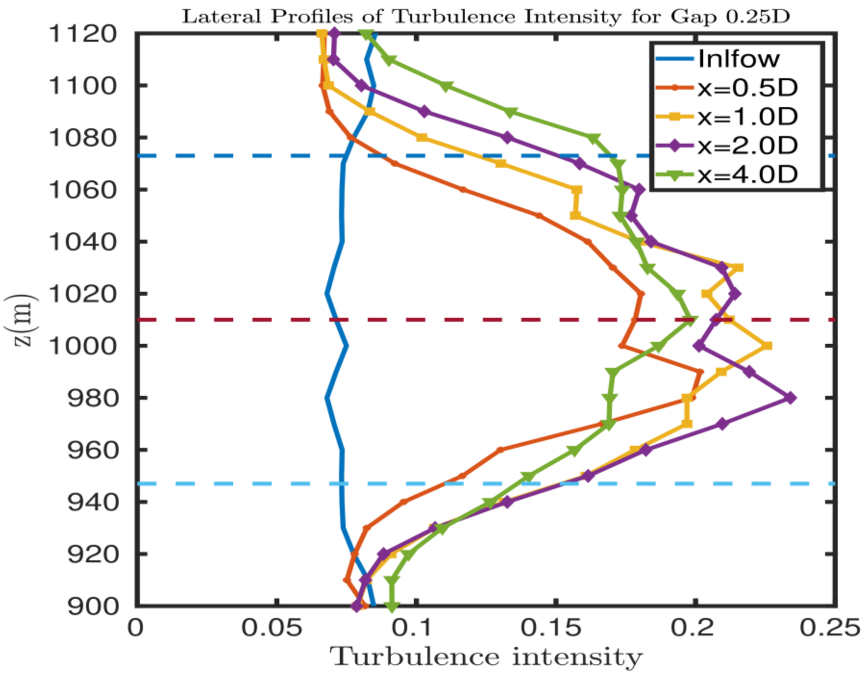

Figure 4.20. Lateral turbulence intensity profile comparison for gap 0.25D at different downstream positions.

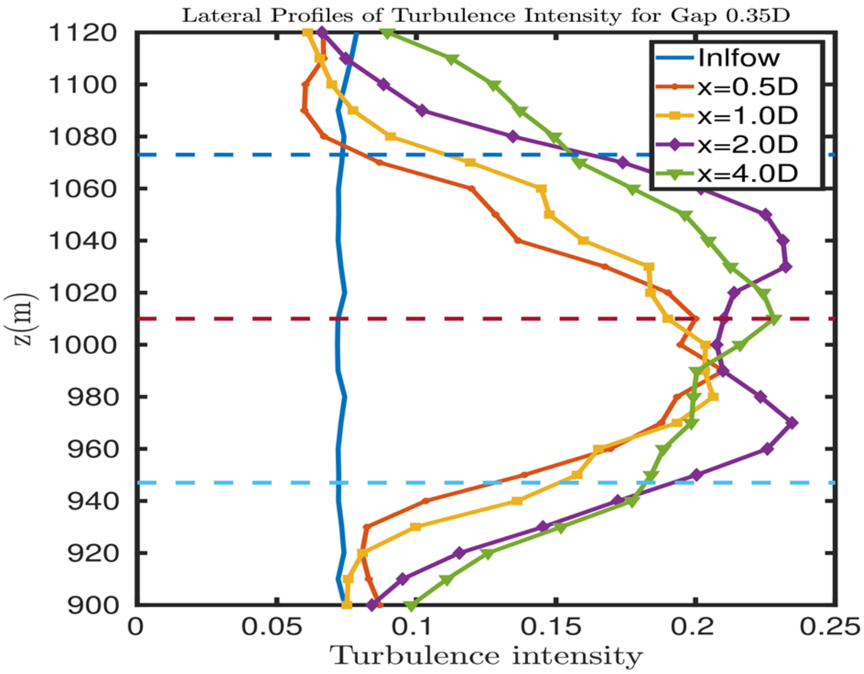

Figure 4.21. Lateral turbulence intensity profile comparison for gap 0.35D at different downstream positions.

4.4 Conclusion

The distance between the rotor disk and the ground plays a critical role in the wake recovery of turbines. A smaller gap between the turbine blades and the ground slows the wake recovery due to reduced vertical mixing, more significant ground effects, and less interaction with high-velocity winds at higher altitudes. On the other hand, a higher gap results in greater downward momentum flux above the hub height and greater upward momentum flux below the hub height compared to the lower gap. The velocity of fluid flow is observed to increase at a greater rate in the larger gap scenario as compared to the shorter gap scenario. The width and length of the wake are smaller with the higher gap case compared to the smaller gap case. The wake region experiences a higher level of turbulent intensity for a larger ground clearance than a smaller ground clearance. In summary, it was observed that the larger gap case (0.35D) facilitated a quicker recovery of the velocity deficit compared to the smaller gap case (0.25D).

Chapter 5

EFFECTS YAW ANGLES AND WIND SPEEDS ON WINDFARM PERFORMANCE

5.1 Introduction

With more initiatives worldwide towards greener energy to mitigate climate change, wind energy has been a leading source. The Intergovernmental Panel on Climate Change (IPCC) special report 15 [27] stated that renewable energy needs to increase from 20% in 2018 to 67% in 2050 to limit global temperature rise to 1.5 °C. More wind farms are being built onshore and offshore to reach that goal. However, proper optimization (i.e., design, operation, control, and grid integration) is still a concern under different conditions of wind farms and the turbulent atmospheric boundary layer (ABL). This is due to the complex interactions between the wind farms and the ABL, whose flow properties are greatly affected by surface roughness, thermal effects, different forcing parameters, among others.

In a wind farm, upstream turbines affect the downstream ones as they extract energy from the upcoming wind while enhancing the turbulence levels and reducing the wind speed in the flow. This phenomenon is known as the wake effect or wake loss, and it can cause a decrease in the overall power output of the wind farm. There are several ways to improve the annual energy production (AEP) of a wind farm, such as pitch and torque control, layout optimization, tilt, and yaw misalignment of wind turbines [28–30]. Wake steering becomes essential, especially when turbines are placed closely, since sparse installations increase costs, particularly cabling. In wake steering, by trading off the power of the upstream turbines, a higher net power of a wind farm is achieved. Wake steering also reduces the fluctuation of wind energy, improving its reliability within the larger power grid. Prior studies [19,28–30] have demonstrated that the degree of wake deflection increases as the flow travels further downstream. The amount of deflection is dictated by the yaw misalignment, the wind speed and direction, the incoming turbulence level, the thermal stability, the thrust coefficient, and other factors (i.e., turbine parameters, surface roughness).

Inflow conditions such as wind speeds, turbulence intensity, and yaw angles affect the flow properties inside the wind farm, thus influencing the power output and the flow-induced dynamic loads of every turbine [31]. Furthermore, the unsteady oscillations of the wake (also known as wake meandering) by eddies larger than the turbine diameter also have important implications for the performance and reliability of wind turbines in a wind farm [32,33]. Under the influences of the different environmental conditions, the turbines experience leading-edge erosion; this affects the aerodynamics and AEP of the wind farm [34,35]. Understanding turbine wake aerodynamics in diverse incoming flow conditions is crucial to enhancing wind farm design, maximizing power output, and minimizing maintenance costs. Several methods are available, including analytical modeling, computational fluid dynamics (CFD), wind-tunnel experiments, and field experiments to study the multi-scale interactions between wind turbines and the atmospheric boundary layer. The experimental and numerical studies [36–38] of single-turbine wakes have shown that the velocity deficit profiles usually have a two-dimensional axisymmetric Gaussian distribution maximum located at hub height in the near wake region. This characteristic of the velocity deficit profiles augments the turbulent mixing of the incoming flow and the wake. When a wind turbine experiences yawed conditions, counter-rotating vortices form in the turbine’s wake, which can interact with the atmospheric boundary layer and cause the wake to take on a kidney shape [39]. The velocity and turbulence levels distribution are thus impacted by the yaw misalignments in all directions [20,40]. The wake characteristics of a yawed flow have been studied using various theoretical and computational models, such as mass and momentum conservation [19], Reynolds-averaged Navier-Stokes (RANS) equations with vortex theory [20], and others [41,42].

As the wake moves downstream, it undergoes several changes. One of these changes is the growth of the wake in both lateral and vertical directions, which is due to the entrainment of the outer flow. Another change in the wake as it moves downstream is the increase in the value of the streamwise velocity component until it eventually recovers to the same value as the surrounding flow [43]. Several studies [31,44,45] have shown that the turbulence intensity level strongly influences the wake recovery rate in the incoming flow. Elevated turbulence levels in the incoming flow lead to better mixing of the wake region with the atmospheric boundary layer. This momentum exchange helps the breakdown of large vortices into smaller ones leading to a faster wake recovery [46]. Higher turbulence levels expedite the faster wake recovery, thus affecting the performances of downstream turbines in wind farms.

When wind flows through a wind turbine, it experiences a change in velocity and pressure as it passes over the rotor blades. This phenomenon causes the wind to separate into layers: the wake region behind the turbine and the atmospheric boundary layer above it. Slower wind speeds and higher turbulence characterize the wake region, where most of the energy extraction occurs. As the wake region moves downstream, it mixes with the surrounding atmospheric layer and creates a shear layer with a significant velocity gradient. Due to the non-uniform logarithmic velocity profile, a non-axisymmetric shear layer is formed, particularly pronounced at the top edge of the turbine. As a result, there is a higher production of turbulent kinetic energy at the upper edge of the wake, leading to an amplification of turbulence levels in that region [5,37,38,47,48]. The turbulence intensity in the wake zone typically has a double Gaussian profile with two peaks at the edges of the wake [44,49]. The transition between near-wake and far-wake occurs from the maxima of the turbulence levels forward, and then turbulence intensity decreases monotonically with downstream distance.

Numerous variables, such as the unpredictability of the local wind speed and the transport properties of turbulence in the wake, affect the best turbine configuration in every wind farm architecture. The biggest factor contributing to the decline in wind farm efficiency is variability in wind speed [50]. After accurately assessing the wind speed variations by appropriate methods (for more details, see [51–54]), their subsequent effects on the aerodynamic characteristics need to be studied. The wake characteristics under high wind speeds while estimating the wind conditions by proper model [55] are also very crucial. How the turbulent wake flow structures within the wind farms under full-wake and partial-wake conditions affect the power output under different wind speeds and yaw angles is underexplored. Most studies [30,56] investigated the performance of wind farms just by changing the layout or yaw angles on a single wind speed mainly by reduced-order models. They found that layout and wake steering are complementary to maximize AEP and minimize wake losses. Field studies are not entirely conclusive when the wake steering effects on the performance of wind turbines are analyzed [57,58]. There have been some studies [59,60] on the effects of steering at variable wind speeds with a few turbines in a row. Howland et al. [59] showed improved power maximization with a row of six turbines at a fixed yaw angle of 20°. Simley et al. [60] found the effectiveness of wake steering in improving energy production was observed for wind speeds ranging from 4–12 ms^{-1} with two turbines, except for 6–8 ms^{-1} due to higher wind direction variability and power loss from yaw misalignment, while its efficacy for wind speeds between 12–14 ms^{-1} remains uncertain due to insufficient data.

To the authors' knowledge, no rigorous studies have been conducted on the combined effect of yaw angle and wind speed on the wind farm's performance and wake physics. Since the performance of wind farms can be significantly affected by the yaw angle and wind speed, understanding these effects is crucial for designing and operating wind farms effectively. Therefore, finding the optimal combination of yaw angle and wind speed is crucial for maximizing wind farms' power output and efficiency. The chapter is structured as follows: Section 5.2 comprehensively explains the numerical details employed in the study. In Section 5.3, the wind farm flow statistics are presented and thoroughly discussed. Finally, Section 5.4 offers a concise summary of the entire analysis. The results presented in this chapter have been published in Energies [8].

5.2 Case Set-Up

The dimensions for all the cases are depicted in Figure 5.1. The grid size in every direction is 10 m. The wind speeds and the yaw angles are listed in Table 5.1. The surface roughness length (y_0) of all the cases is 0.1 m, the value typically used for the flat terrains in onshore wind farms. The diameter (D) and hub height (y_h) of the turbine are 120 m. In the study, each turbine's thrust coefficient C_T (=3/4) was maintained constant across all cases to primarily investigate the influence of varying wind speeds at different yaw angles.

The flow statistics were collected for over 260 flow-through times. The simulations were run over 70 flow-through times to ensure they reached a fully turbulent state. The time window (T) in the time adaptive wind turbine model was 600 s.

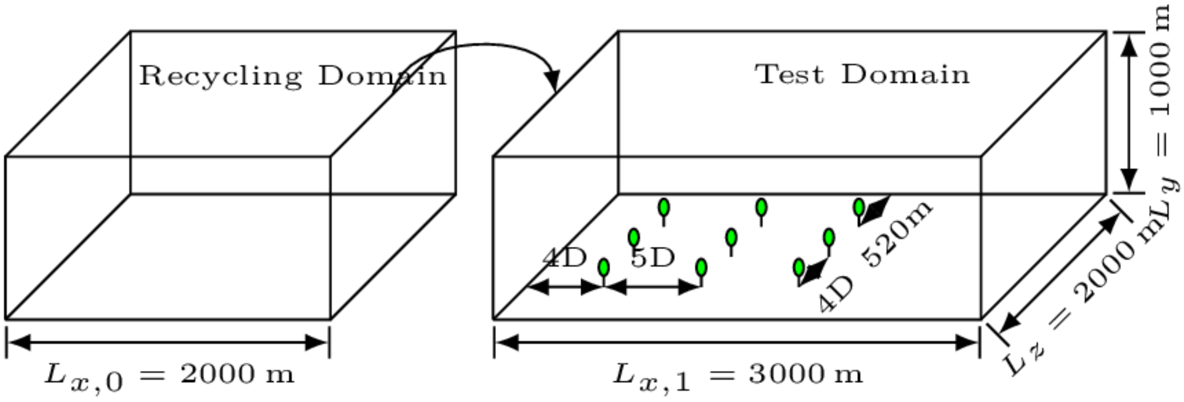

Figure 5.1. Sketch of the computation domain consisting of a recycling domain and a test domain with all the dimensions relevant to this case study.

Table 5.1. All the simulation cases of the present study with their respective wind speeds and yaw angles.

ABL Cases	**Wind Speeds, U_∞; u (ms^{-1})**	**Yaw Angles, γ (°)**
case A	7.3; 0.412	30
case B	7.3; 0.412	20
case C	7.3; 0.412	0
case D	10.4; 0.587	30
case E	10.4; 0.587	20
case F	10.4; 0.587	0
case G	4.3; 0.243	30
case H	4.3; 0.243	20
case I	4.3; 0.243	0

5.3 Results and Discussion

All the findings from this study are discussed in the following sections systematically for a better understanding of it.

5.3.1 Analysis of the Contours of the Flow Fields and Turbulence Intensity

Figure 5.2 displays the time-averaged velocity deficit field in the XZ plane at hub height for all cases, showing how the wake steering affects the deflection of the wake downstream of the wind farm. The secondary effects of the wake steering cause an additional deflection of the wake in the downstream direction of the wind farm. When the turbine converts a portion of the incoming turbulent kinetic energy (TKE) into power output, a low-speed zone (also known as the wake region) forms behind it. The wake then extends downstream and widens due to turbulence mixing, allowing the wind to recover before reaching the next turbine. The momentum exchange between the wake region and the ambient flow increases with increasing yaw angle. However, the relative exchange does not increase significantly with increasing speeds, leading to a little mismatch in self-similarity in velocity deficit profiles (normalized by hub height velocity, $\mathbf{U_h}$).

The velocity deficit contours reveal a high-speed channel of unperturbed velocity containing a significant amount of kinetic energy that passes through space between the columns of the turbine in wind farms for non-yawed cases, as depicted in Figure 5.2. In contrast, for yawed cases, this energy is extracted more and more as the flow moves downstream with an increasing yaw angle. It is worth noting that even with the largest yaw angles, the lateral wake interactions are minimal to zero. Therefore, the spanwise distance between turbine columns is sufficient to avoid these interactions.

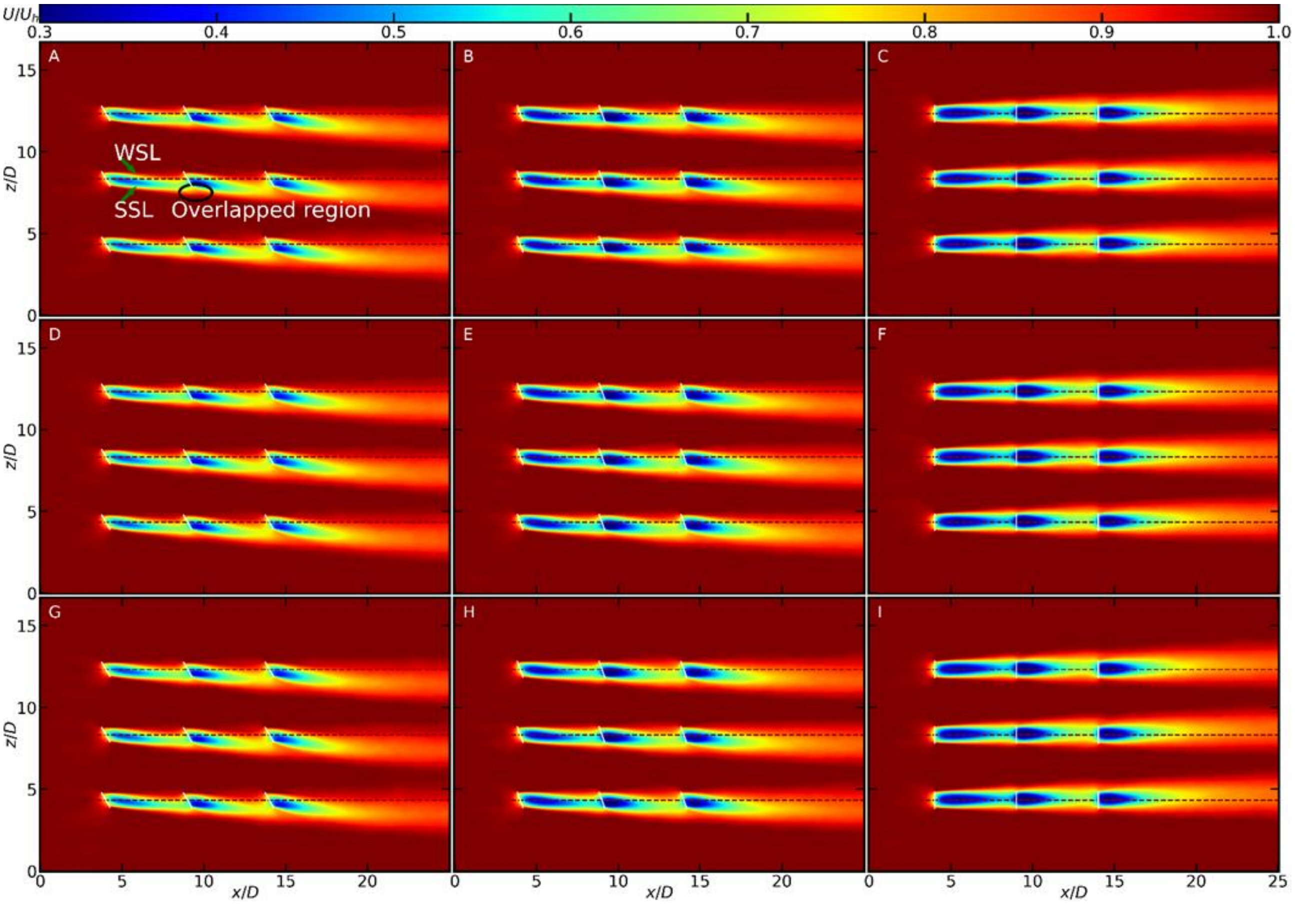

Figure 5.2. Visualization of wake of all the cases at hub height in XZ plane. The diameter normalizes all the dimensions. The white and maroon lines represent the turbines and the connected centers of the turbines in a column, respectively.

The turbulence intensity distributions in the XZ plane at hub height for all cases are presented in Figure 5.3. The turbulence intensity is the ratio of the standard deviation, $\boldsymbol{\sigma_u}$ (or root mean square) of the local fluctuating velocities to the mean unperturbed velocity at hub height, $\mathbf{U_h}$. In all the cases, TI is higher at the wake edges and shear layers due to a higher production rate of turbulent kinetic energy (TKE) than its dissipation. This rise in turbulence levels is primarily due to shear layers and momentum flux transfer from the incoming atmospheric boundary layer into the wake region. The accumulation of TI in the downstream direction leads to a quick recovery of the wakes and a shortening of the near-wake lengths.

A dual-peak turbulence distribution is observed, with enhanced shear layers at the edges of the turbine. Under yawed conditions, this distribution becomes asymmetric, and the asymmetry increases with increasing yaw angles. This results in an asymmetric wake recovery, as evident in the velocity-deficit profiles and contour plots.

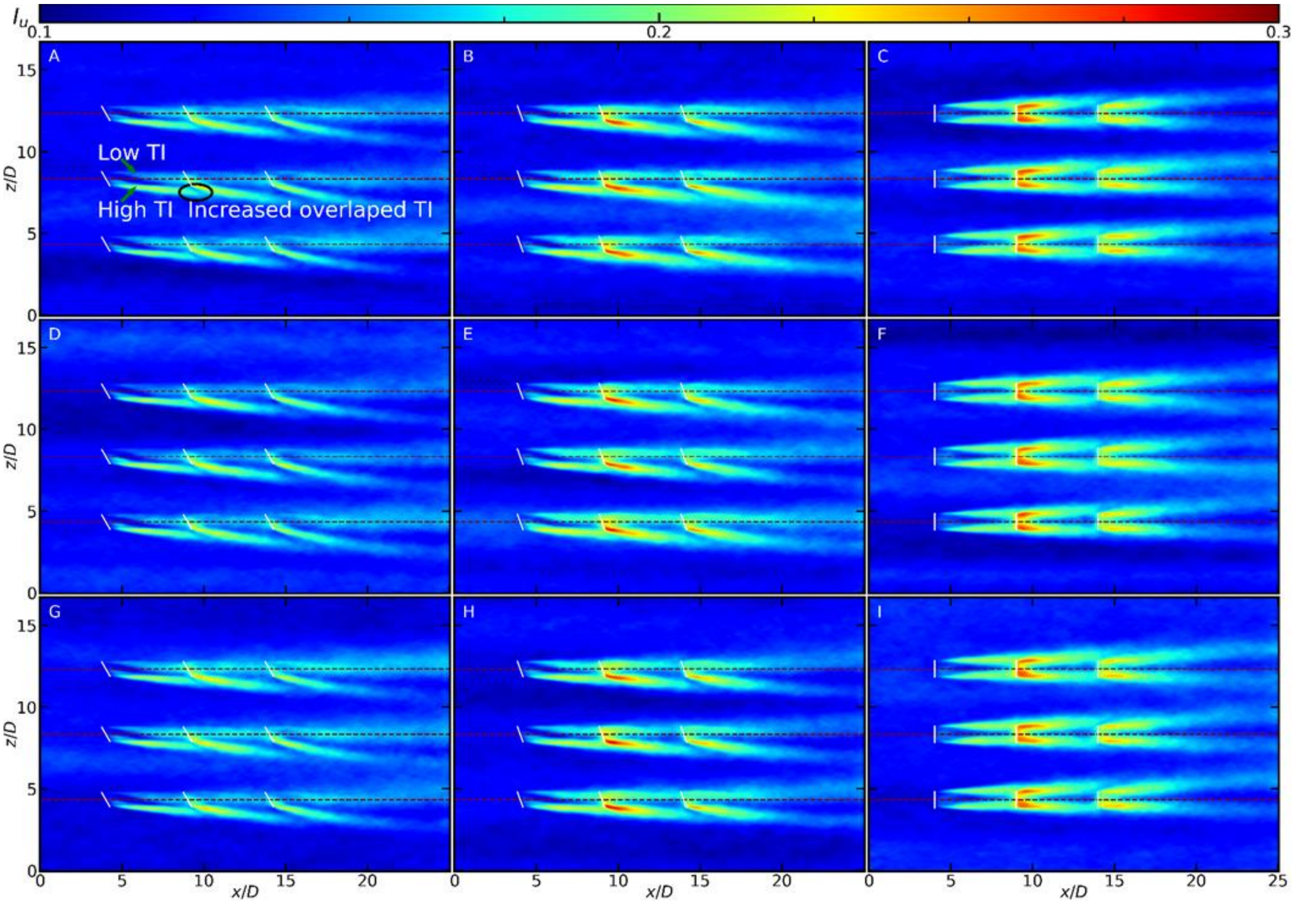

Figure 5.3. Turbulence intensity contours of the XZ planes at hub height of all the cases.

Compared to non-yawed cases, yawed cases have more added turbulence (turbine-wake-induced turbulence intensity) downstream. This added turbulence increases wake width with no significant decrease in velocity deficit downstream.

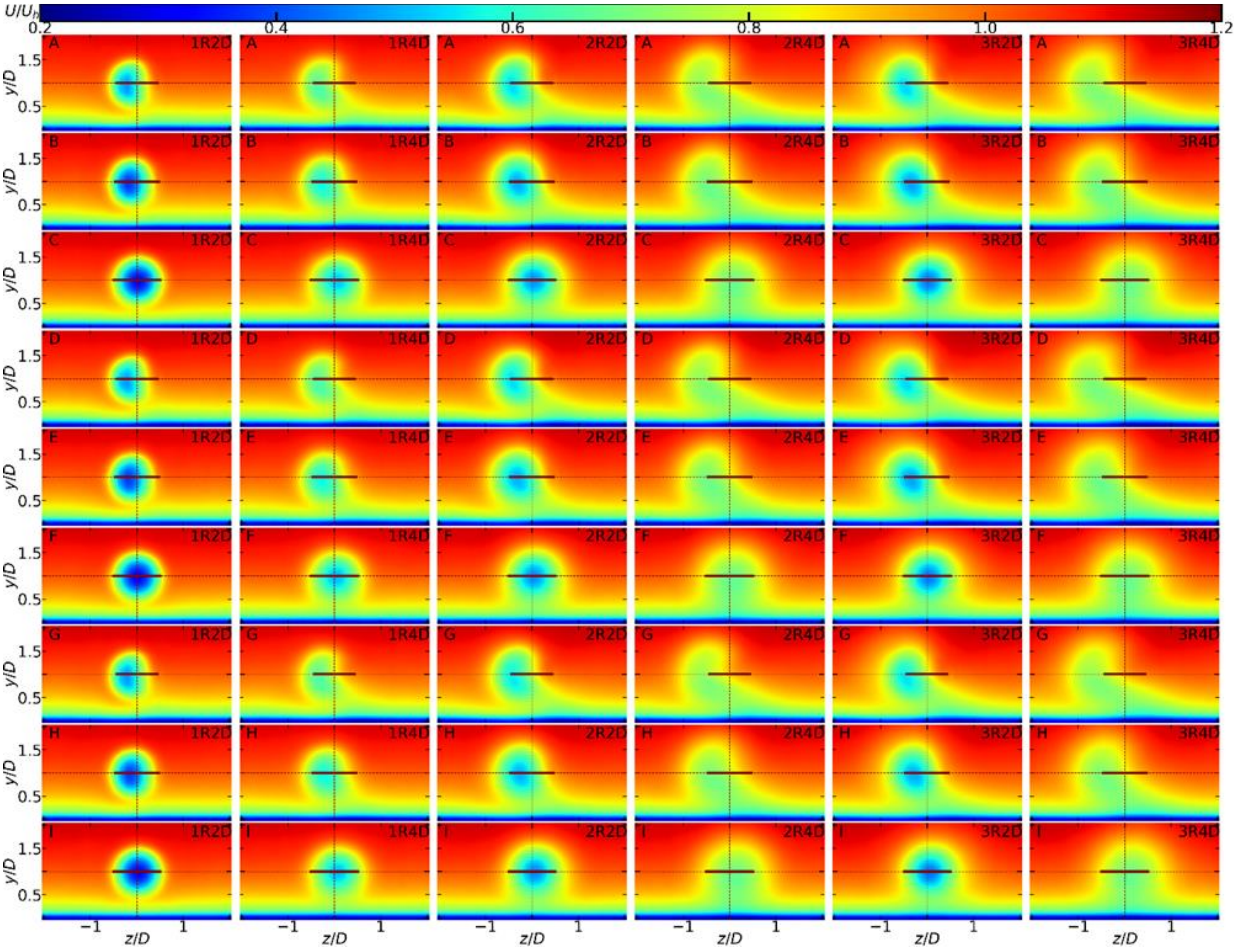

Figure 5.4. Contour of the streamwise velocity deficits of the YZ plane at two downstream positions of each row for all the cases. In the labels “xRyD”, x and y represent the row number and the downstream distance from the same row, respectively.

Figure 5.4 displays the streamwise velocity contours in the YZ plane at 2D and 4D distances from each turbine of each row for all the cases. Yawed cases generate a pair of counter-rotating vortices at the top and bottom of the turbine rotor, and these vortices shift the wakeline away from the center as the wake moves downstream. The vortices eventually turn into a curled shape at further downstream locations. Although the yaw angles significantly influence the shape of the vortices, the influence of wind speeds is insignificant. The curled wake shape becomes more pronounced with increasing yaw angles, and slightly larger vortices are produced at higher wind speeds. That is why the wake moves less from the centerline for lower wind speeds, and this behavior is also evident in Figure 5.10 further below.

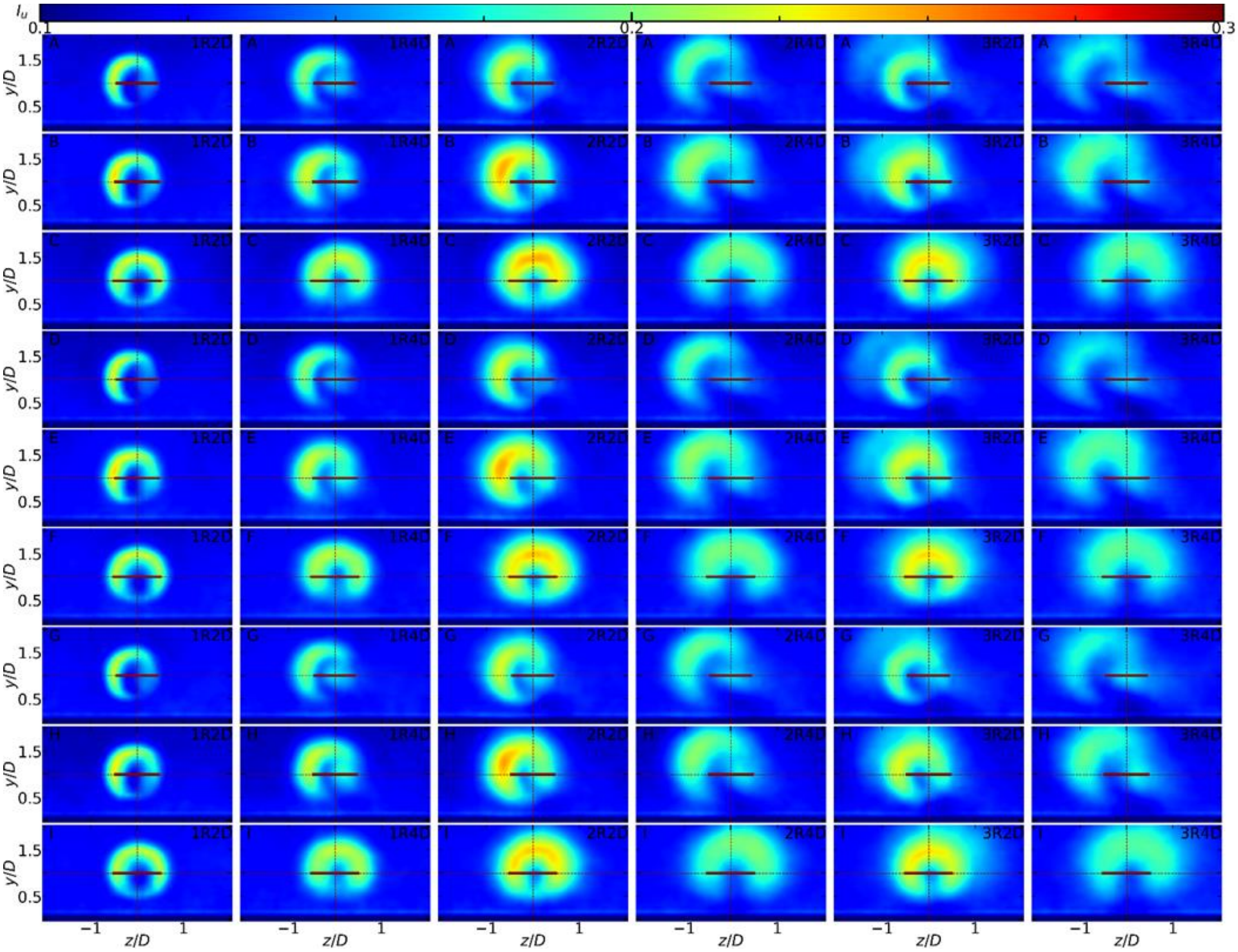

Figure 5.5. Contour of the turbulence intensity of the YZ plane at two downstream positions of each row for all the cases.

Figure 5.5 shows the turbulence intensity (TI) of the streamwise velocity in the YZ cross-sectional planes at different downstream positions of the wind farm. The distribution of the TI also exhibits the evolution of the curled shape phenomenon. In the wake of a turbine, the entrainment of surrounding fluid causes a significant impact on the TI of the flow. At the upper edge of the wake, the entrainment of high-momentum fluid from the boundary layer results in an increase in TI due to increased shear and turbulence generation. Conversely, at the lower edge of the wake, the entrainment of low-momentum fluid from the boundary layer leads to a decrease in TI due to reduced shear and turbulence generation.

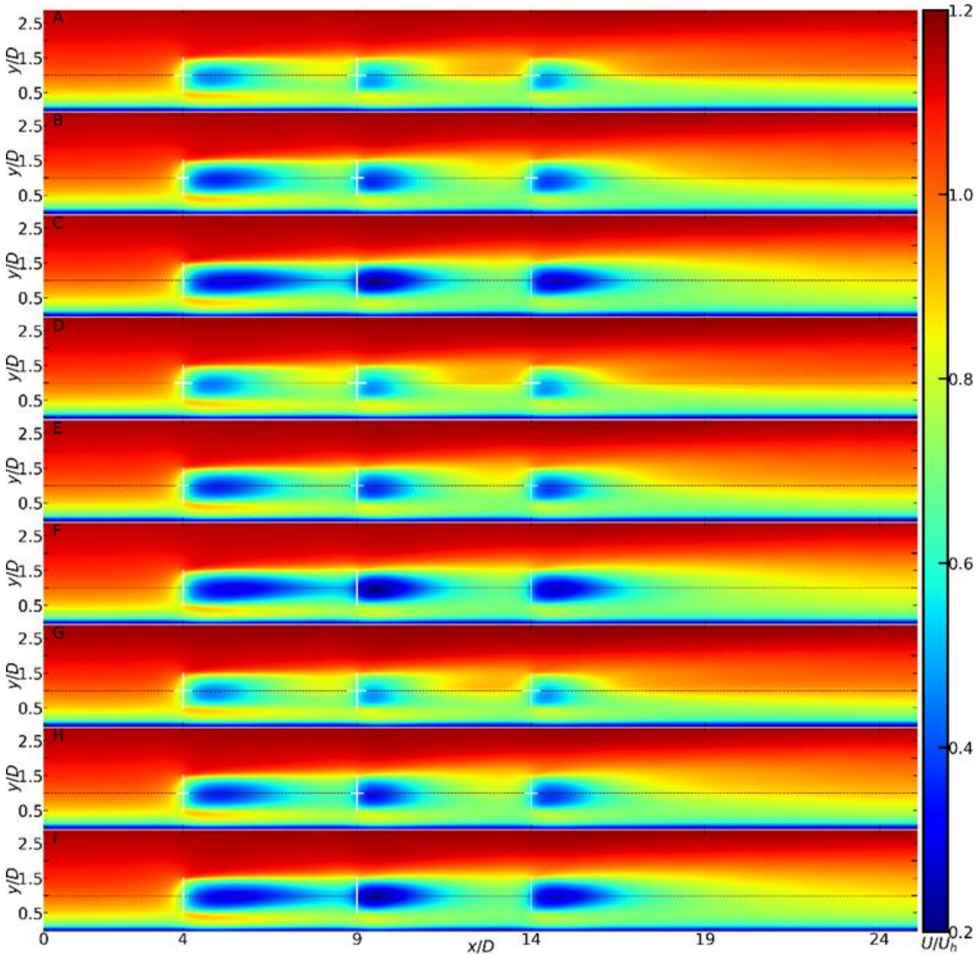

Figure 5.6. Contour of the velocity deficits of the XY plane for all the cases.

The displacement of the wake in the XY plane of streamwise velocity is observed to exhibit vertical characteristics, as demonstrated by Figure 5.6. This displacement is primarily caused by interactions between counter-rotating vortices, the ground, and the rotation of the wake, with the most prominent effects being observed under yawed conditions. The extent of this displacement is directly proportional to the magnitude of the yaw angle. The direction of the displacement depends on the orientation of the counter-rotating vortices, which is a function of the sign of the yaw angle. The vertical displacement of the wake is critical to the overall wake deflection, which is further instrumental in mitigating wake losses downstream. Wind shear differences in the vertical direction exhibit significant variation with changing yaw angles but are relatively small with variations in wind speeds in the wake region. The accelerations at the wake edges are determined to be negligible for all three wind speeds at any specific yaw angles at any downstream position. Given their minimal effects on wake recovery, these accelerations' contributions to turbines' power output are also insignificant. The presence of these accelerations under neutral atmospheric conditions is primarily attributed to the adjacent upstream wakes in wind farms.

In a fully developed wake region, the vertical kinetical energy flux brings the high-speed wind down to the upstream of the turbine at the hub height level. This energy flux results from the complex interplay of atmospheric turbulence, wake-induced turbulence, and the cumulative growth of the boundary layer due to wake, as illustrated in Figure 5.6 and Figure 5.7. The vertical kinetical energy flux increases as the flow moves downstream, as evident from the increased turbulence levels and boundary layer growth. The turbulence intensity profiles and contour plots consistently indicate elevated turbulence levels near the upper edges of the rotor due to stronger wind shear, which leads to turbulent mixing, eddy formation, and vortex generation.

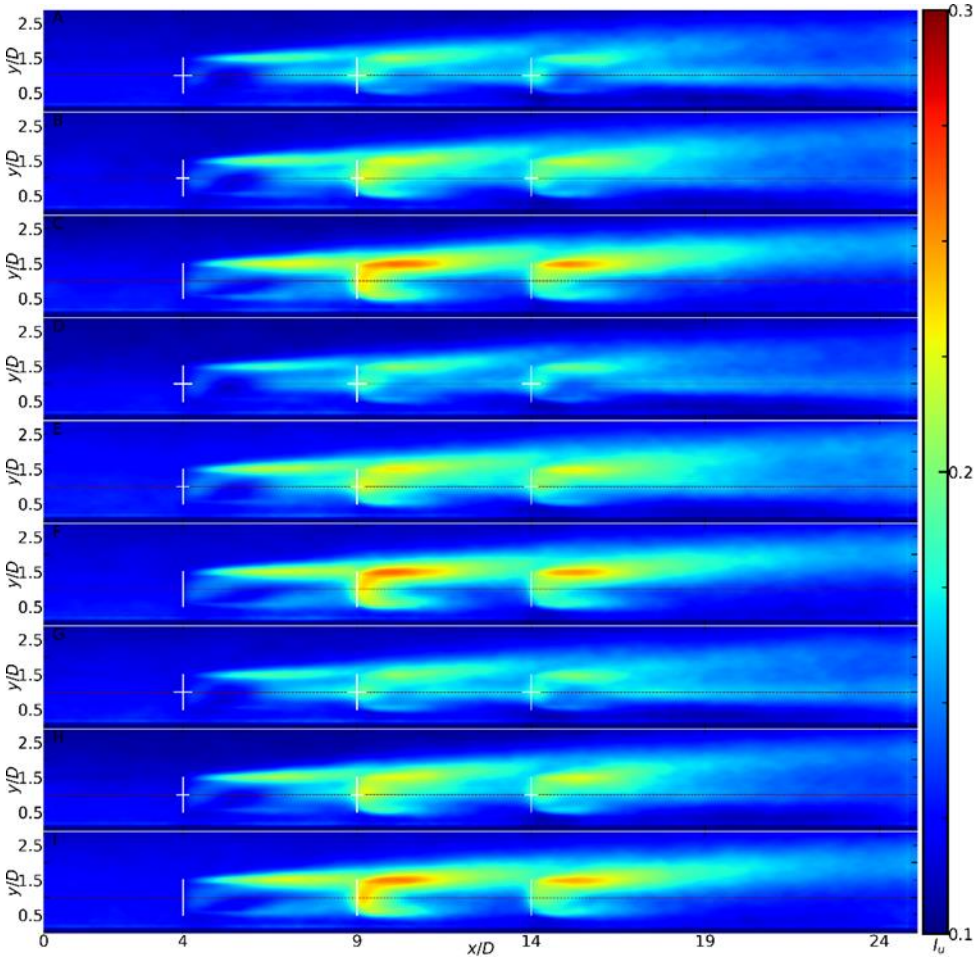

Figure 5.7. Contour of the turbulence intensity of the XY plane for all the cases.

Figure 5.8 presents a comparative assessment of the wake width at downstream locations of 2D and 4D for each row of turbines for all cases studied. The results indicate that the wake width gradually increases beyond 4D downstream of the third row, contributing to the expansion of the wind-farm wake. This phenomenon is attributed to the increased turbulence mixing in the downstream flow by mean-wind advection and turbulent transport. The velocity deficit profiles exhibit a two-dimensional Gaussian axisymmetric behavior for non-yawed cases, consistent with previous research [37,61]. However, the lateral profiles of the yawed cases are non-axisymmetric, and the degree of asymmetry increases as the flow advances downstream and the yaw angle increases. Thus, the wind-farm wake characteristics are influenced by the yaw angle and the downstream distance, and these factors significantly affect the wake width and its expansion.

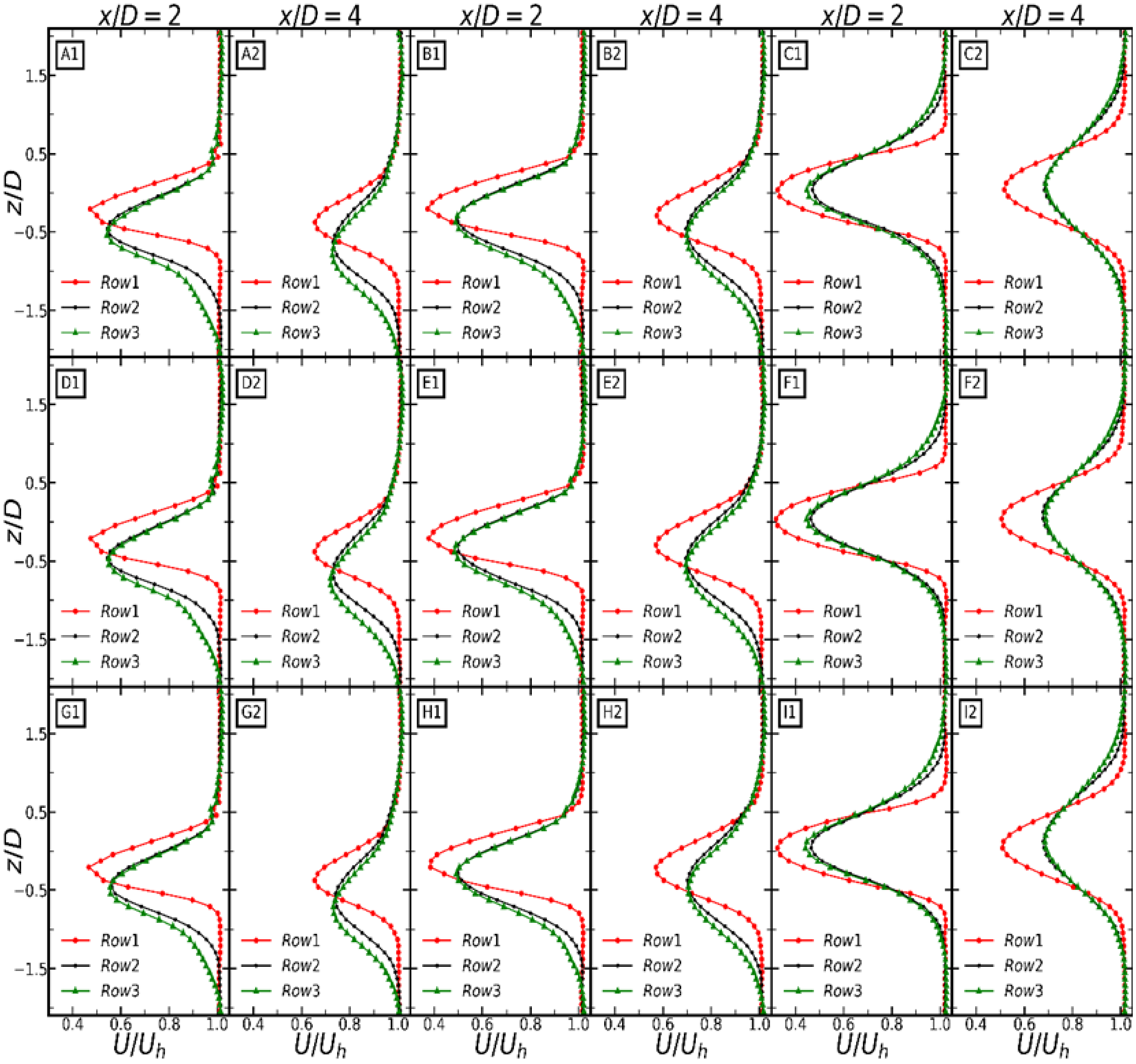

Figure 5.8. Comparison of velocity deficits among the rows at two downstream positions for all the cases. A1 and A2 refer to two downstream positions (2D, 4D) of case A, others (B1, B2…) follow the same pattern.

5.3.2 Analysis of the Plots of the Flow Fields and Turbulence Intensity

Figure 5.9 compares the lateral turbulence intensity profiles for three rows at two downstream positions (2D and 4D) in all cases studied. The results show that, after all three rows, the near-wake region around 2D downstream positions exhibits higher turbulence levels. The TI experiences variations in both magnitude and spatial distribution as the flow progresses downstream. Turbulent mixing reduces the turbine-wake-induced turbulence levels downstream, resulting in a more uniform velocity profile with reduced fluctuations, particularly in the far downstream region where turbulent structures have dissipated and mixed with the mean flow. This diffusion and merging of turbulent fluctuations with the mean flow are responsible for reducing total TI downstream. These findings suggest that the wind-farm wake characteristics are influenced by turbulent mixing and the downstream distance, which affects the spatial distribution and magnitude of TI in the wake region.

The wake losses are observed to be nearly identical for all velocities in the non-yawed cases, as illustrated in Figure 5.10. This phenomenon is also reflected in the power output results, as depicted in Figure 5.14 below. Furthermore, Figure 5.10 highlights that the wake deflection is more prominent for higher speeds in the yawed cases. Given the lesser wake steering for lower speeds, the blockage losses are higher for them. This wake behavior significantly impacts the power output, particularly for the yaw angle of 20°. The relative power output experiences a decline for the lower speeds, particularly for speed 4.3 ms^{-1}. Notably, the difference in the lateral spreads of the wakes for different wind speeds is insignificant even farther downstream of the turbines, especially for higher wind speeds. As the yaw angle reduces, the lateral wake spread becomes more noticeable due to the lesser mixing of momentum of the wake and undisturbed flow from both above and sideways. This characteristic of the wake considerably influences the power output of each turbine.

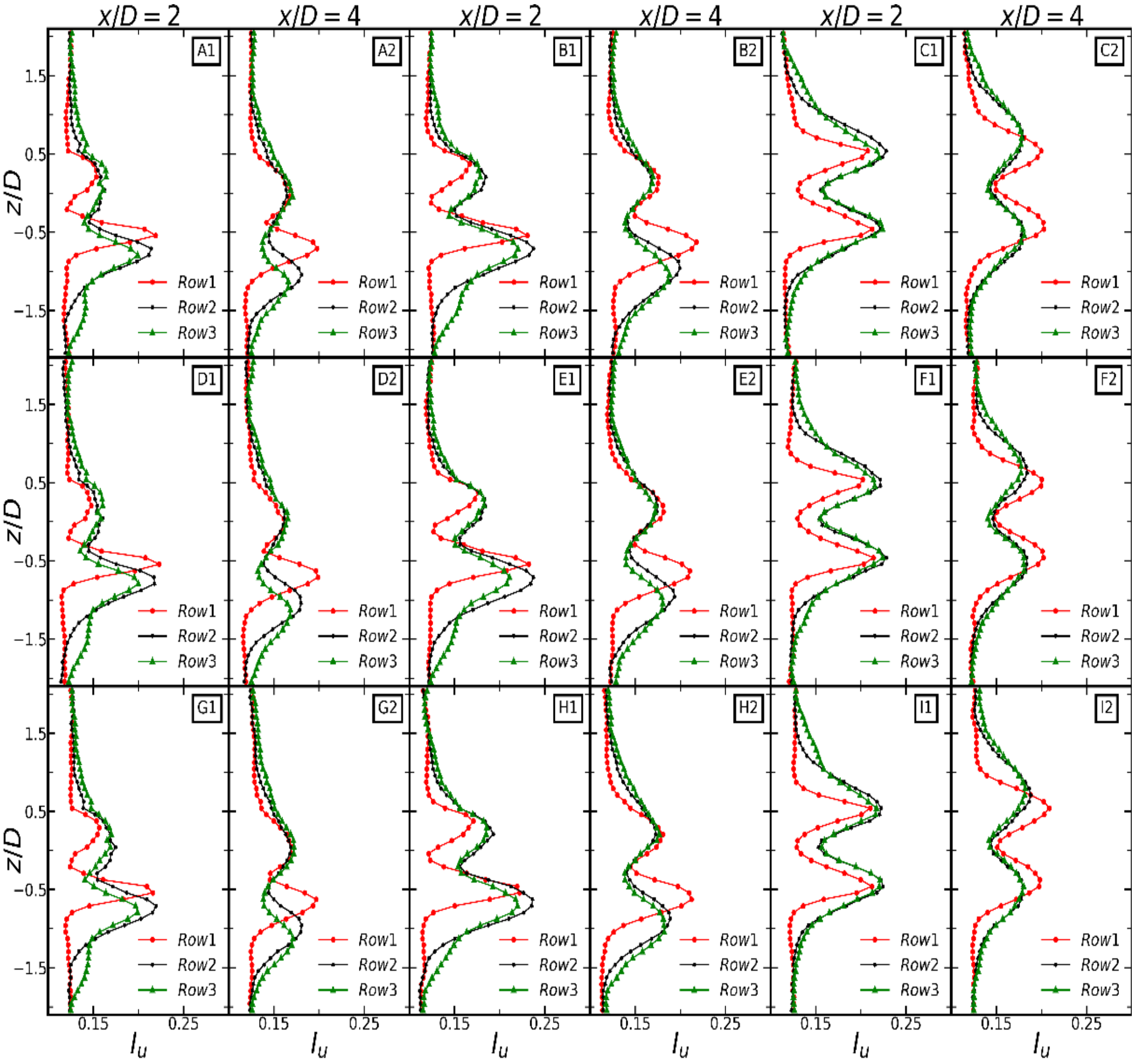

Figure 5.9. Comparison of turbulence intensity among the rows at two downstream positions for all the cases. A1 and A2 refer to two downstream positions (2D, 4D) of case A, others (B1, B2…) follow the same pattern.

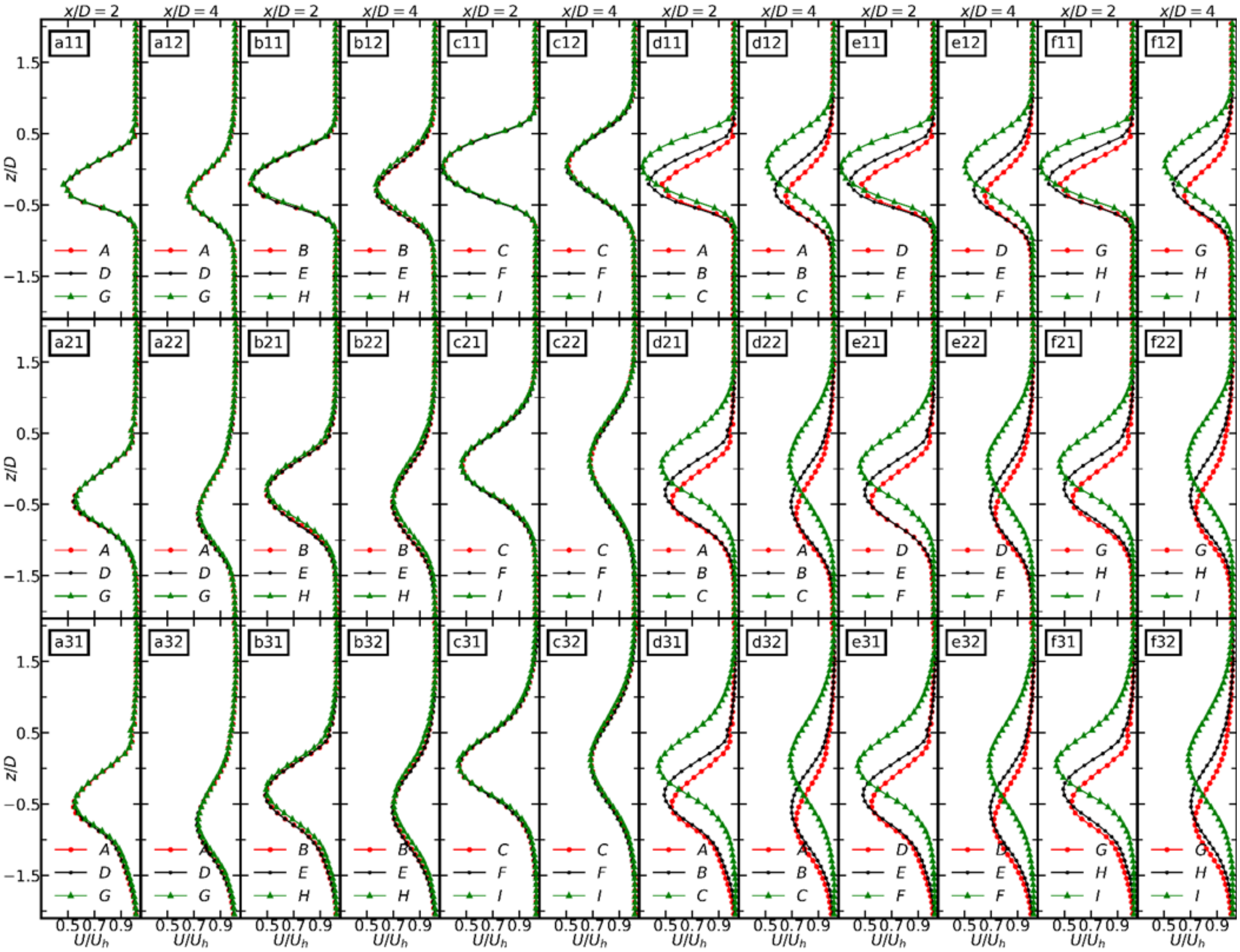

Figure 5.10. Comparison of the velocity deficits for different yaw angles and wind speeds, at downstream, for the three rows. Each row in the figure refers to each row of the wind farm.

The turbulence intensity profiles in the XZ plane at hub height exhibit similar trends to the velocity deficits, as illustrated in Figure 5.10 and Figure 5.11. The wind speed and yaw angle variations affect the magnitude and location of the maximum TI, influencing wind turbines and wind farms' performance and efficiency. The elevated wind speeds displace the maximum TI away from its original position due to increased mixing and turbulence, leading to downstream expansion and shift of the wake. The profiles exhibit more deflection as the wind speeds increase, particularly for the yaw angle of 20°. As the flow convects further downstream, the difference in the deflection of the profiles becomes more noticeable with the change in wind speeds at any yaw angle. This wake behavior can more significantly impact power output when additional turbine rows are placed after the third row, and the difference in power output can be more pronounced.

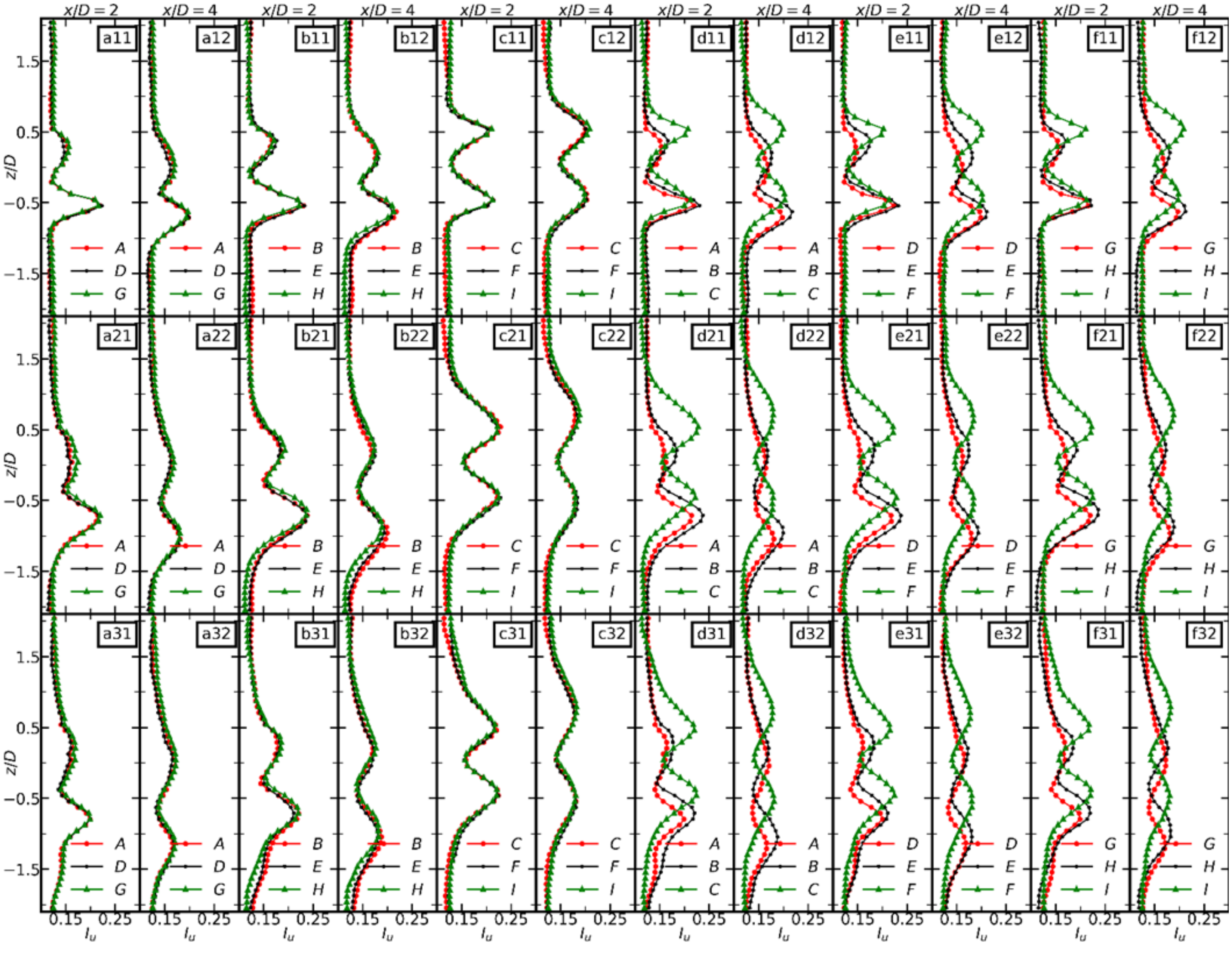

Figure 5.11. Comparison of the turbulence intensity for different yaw angles and wind speeds, at downstream, for the three rows. Each row in the figure refers to each row of the wind farm.

The impact of wind speed on the vertical velocity deficits is shown in Figure 5.12, which indicates that there is only a weak correlation between these two parameters, except for the yaw angle of 20°. Typically, weaker shear layers are formed at lower wind speeds, resulting in less mixing between the wake region and the incoming atmospheric boundary layer. This

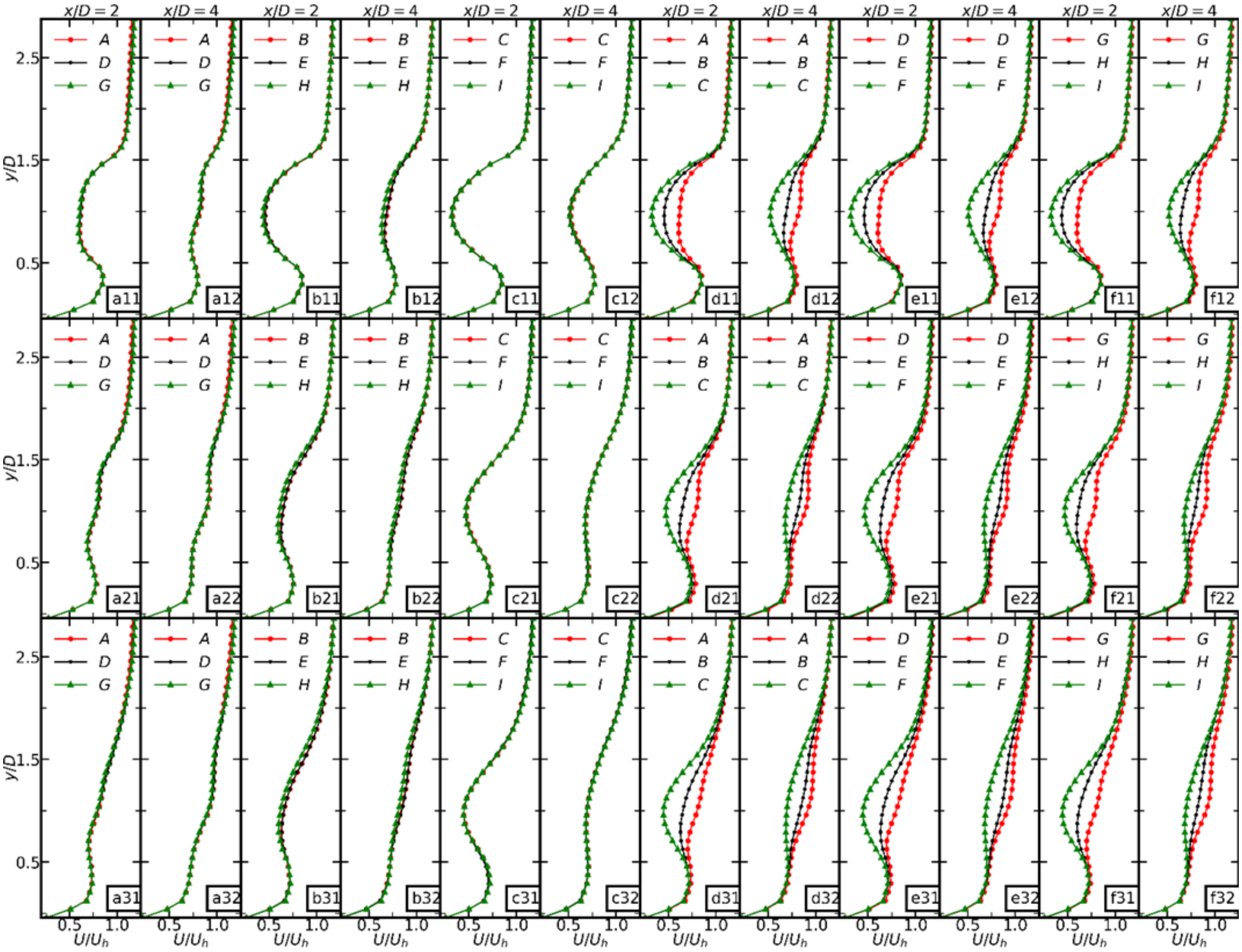

Figure 5.12. Comparison of the vertical profiles of velocity deficits for different yaw angles and wind speeds, at downstream, for the three rows. Each row in the figure refers to each row of the wind farm.

wake behavior significantly impacts power output, as illustrated in Figure 5.14. However, the effects of this behavior are mitigated in the far wake region by the lateral transport of the flow.

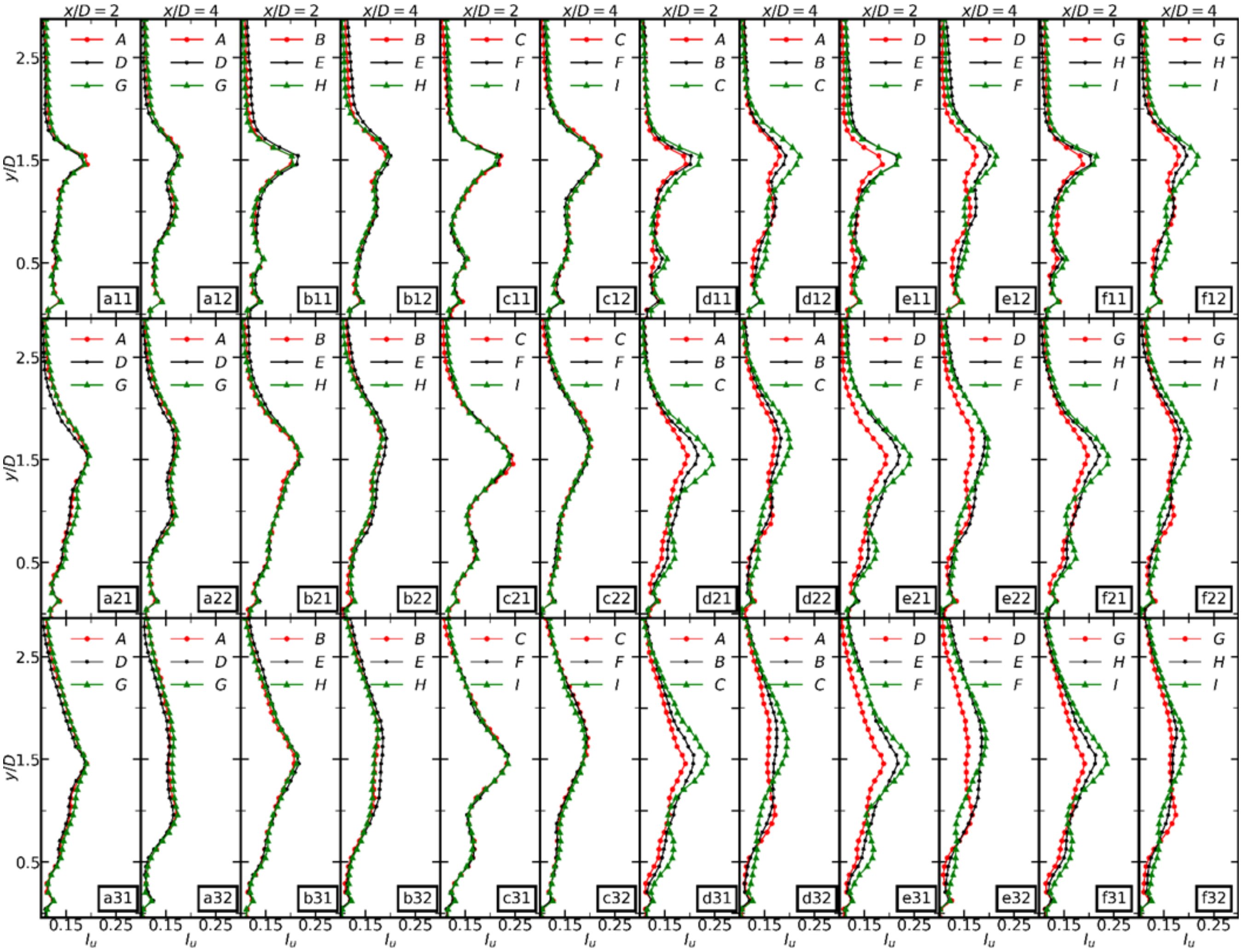

Figure 5.13. Comparison of the vertical profiles of turbulence intensity for different yaw angles and wind speeds, at downstream, for the three rows. Each row in the figure refers to each row of the wind farm.

The results presented in Figure 5.13 indicate that the vertical turbulence intensity profiles do not exhibit a significant dependence on wind speed variations for different yaw angles. However, changes in yaw angles affect the TI profiles at any specific wind speed.

Increasing yaw angles increases turbulence levels, particularly at the turbine edges. Mixing wake turbulence with lateral turbulence in the far wake region mitigates these effects, leading to wake recovery. On the other hand, stronger shear introduces more momentum into the wake, resulting in more eddies and vortices, thereby increasing turbulence intensities when the shear is stronger.

5.3.3 Analysis of the Relative Power Output of Wind Farms

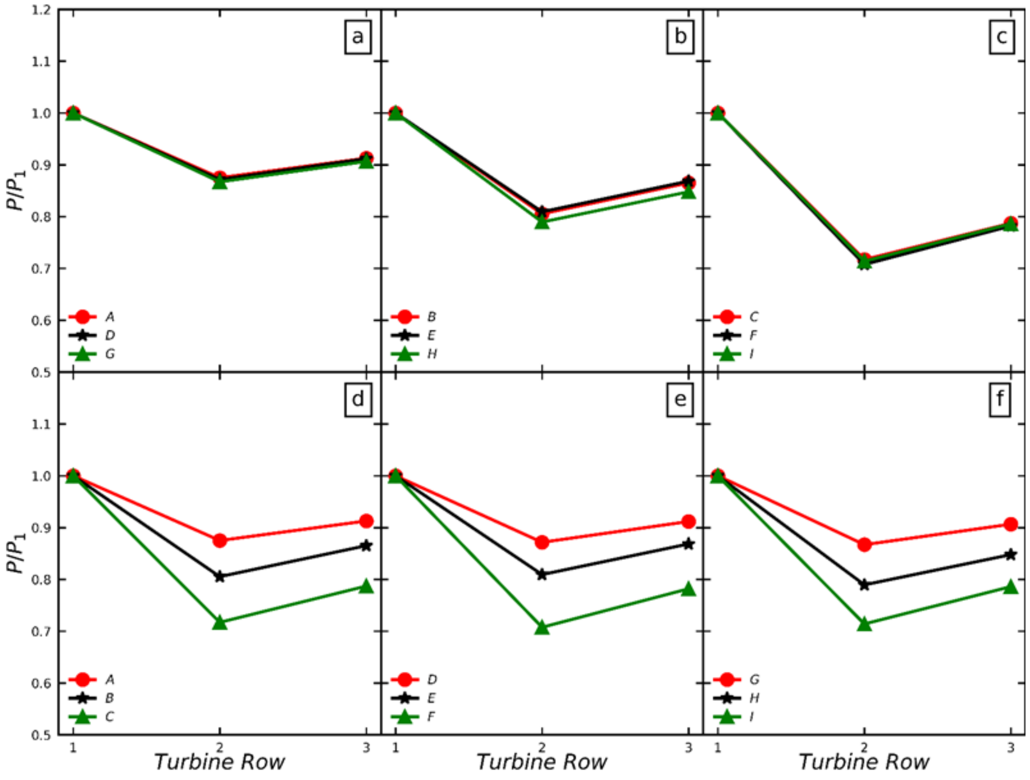

Figure 5.14. Relative power output comparisons for the different speeds and yaw-angles. The subfigures a, b, and c refer to the comparison among three wind speeds at 30°, 20°, and 0° yaw angles, respectively. The subfigures d, e, and f compare three yaw angles at 7.3 ms^{-1}, 10.4 ms^{-1}, and 4.3 ms^{-1} wind speeds, respectively.

In Figure 5.14, the power output of turbines within the wind farm is presented, which has been normalized by the power output of a representative upstream turbine. The power values have been averaged over time and across the same row of turbines. The analysis investigates the effect of different yaw angles at various wind speeds on the power output of the turbines.

The variability in incoming turbulence has been identified as a potential factor contributing to the observed difference in power output between the second and third rows of wind turbines. This can be attributed to the fact that turbulence can significantly impact the efficiency of wind turbines by causing unpredictable wind speeds, which can lead to reduced power output. In all cases considered, the power output of the second row of turbines was found to be lower than that of the third row. This trend can be explained by the relatively slow recovery of wakes behind the first row, which is characterized by a high-velocity deficit and low turbulence levels, compared to the second row. Beyond the second row, however, the increased turbulence levels facilitate a faster recovery of wakes, resulting in greater power generation. These findings highlight the importance of considering turbulence levels and wake dynamics in optimizing the design and placement of wind turbines for maximum power generation.

In the absence of yaw misalignment of turbines, full wake interactions demonstrate weak dependence on wind speeds. Similarly, partial wake interactions exhibit limited sensitivity to wind speeds for a yaw angle of 30°. However, when the turbines are yawed at 20°, partial wake interactions show a slightly stronger dependence on wind speeds, particularly at lower wind speeds. Notably, at wind speeds of 4.3 ms^{-1}, the relative partial wake interactions are comparatively stronger for lower wind speeds. The downstream turbines' gradual decrease in power output indicates that greater momentum extraction from the fluid flow than entrainment occurs. These wake interactions' impact is evident in the power output of wind turbines, as depicted in Figure 5.14.

5.4 Conclusions

In this study, we performed nine large eddy simulation (LES) cases of the neutrally stratified atmospheric boundary layer (ABL) flow through a three-by-three wind farm. The study's primary purpose was to analyze the effects of the variability of wind speeds at different yaw angles on the wind farm's wake characteristics and power output. All the LESs cases have almost the same turbulence intensity of 12.0% at hub height, and the three wind speeds are about 7.3 ms^{-1}, 10.4 ms^{-1}, 4.3 ms^{-1}, and the three yaw angles are 30°, 20°, and 0°. Wind speed variations have little influence in wake characteristics for any yaw angle, except for the wind speed 4.3 ms^{-1} at the yaw angle of 20°. The wake deflection is higher at higher wind speeds and with yawed wind turbines. However, the degree of wake steering is reduced at lower wind speeds, resulting in increased blockage losses. At lower wind speeds, the turbulence intensity profiles show reduced deflection, particularly at the yaw angle of 20 degrees when the wind speed is 4.3 ms^{-1}. As the flow progresses downstream, the difference in the degree of deflection between the profiles becomes more apparent, regardless of the yaw angle, due to the varying wind speeds. This wake behavior significantly affects the power generated, especially when the turbines are yawed. The power losses are higher for the lower wind speeds, especially for the yaw angle of 20° at the wind speed of 4.3 ms^{-1}.

Chapter 6

CONCLUSION

The dissertation presents the development of a code called WIND4D, which uses Finite Volume Method (FVM) and Concurrent Precursor Method (CPM) for both Direct Numerical Simulation (DNS) and Large Eddy Simulation (LES). The study focuses on the wake characteristics of single-turbine and wind farms in a neutral atmospheric boundary layer. A Time Adaptive Actuator Disk Method (ADM) was used to simulate the turbine thrust force, and to model the effects of the wind turbine's vertical orientation change, yaw implementation was added to the solver.

A thorough validation process was conducted to ensure that the LES solver accurately produces the statistics of wind turbine and wind farm wakes. The precursor domain's statistics, such as mean velocity profile, mean velocity gradient profile, Reynold stress profile, and SGS stress profile, align well with theoretical predictions and other benchmark results, be it experimental or numerical. The wind farm velocity deficit and turbulence intensity profiles exhibit good agreement with wind tunnel measures, particularly around the rotor area. Both utility-scale and miniature-scale wind turbine statistics, such as mean velocity deficit profiles and turbulence intensity, correspond well with both experimental and other validated simulation results.

The distance between the lower edge of a wind turbine and the ground, known as ground clearance, has a significant impact on the characteristics of the wind turbine. The study focused on two different cases, one with a 0.25D gap (hub height 90m) and the other with a 0.35D gap (hub height 103.5m), both of which were analyzed using the same parameters. When the gap is larger, the wind speed gets more accelerated due to the higher momentum flux passing through the clearance, compared to when the gap is smaller. Additionally, due to the higher vertical kinetic energy mixing from both above and below the turbine in the wake region, the larger ground clearance case results in a higher turbulence intensity compared to the smaller one. It has been observed that the larger gap facilitates a faster wake recovery than the smaller gap. The results of this study provide valuable insights into the significance of ground clearance in wind turbine design and operation.

The last part of the study aimed to investigate the impact of wind speed variability at different yaw angles on the power output and wake characteristics of a wind farm. The study involved nine large eddy simulations, with all the LES cases having a turbulence intensity of 12.0% at hub height. The findings showed that wind speed variations had little impact on wake characteristics for any yaw angle except for the wind speed of 4.3 ms^{-1} at a yaw angle 20°. At higher wind speeds, wake deflection was higher when wind turbines were yawed, while at lower wind speeds, the degree of wake steering decreased, leading to increased blockage losses. The study also observed that the wake behavior significantly affected the power generated, particularly when the turbines were yawed, with power losses being higher for lower wind speeds, especially for the yaw angle of 20° at a wind speed of 4.3 ms^{-1}.

In the future, it is recommended to conduct various studies to investigate the combined impacts of wakes in the wind farm. For instance, studying the wind farm performance at higher wind speeds with varying yaw angles than the considered wind speeds in the current study would be beneficial. It would also be interesting to observe how wind farms behave around the cut-out wind speed, especially in extreme weather conditions.

To identify the optimal gap, a more comprehensive study with a higher-resolution grid is required. Additionally, future studies should explore the relationship between rotor gap, aerodynamic surface roughness, and atmospheric stability. Once a better understanding of the rotor disk gap is established, the study should expand to include arrays of turbines.

Furthermore, all the case studies of this dissertation can be further investigated by modeling the wind turbine tower and the nacelle. These investigations can also be extended to modeling the rotation of the rotor. A further study with the actuator line method (ALM) can provide more insights into the near wake.

REFERENCES

[1] Vermeer, L. J., Sørensen, J. N., and Crespo, A., 2003, "Wind Turbine Wake Aerodynamics," Progress in Aerospace Sciences, **39**(6), pp. 467–510.

[2] Barthelmie, R. J., Frandsen, S. T., Nielsen, M. N., Pryor, S. C., Rethore, P.-E., and Jørgensen, H. E., 2007, "Modelling and Measurements of Power Losses and Turbulence Intensity in Wind Turbine Wakes at Middelgrunden Offshore Wind Farm," Wind Energy, **10**(6), pp. 517–528.

[3] Nygaard, N. G., 2014, "Wakes in Very Large Wind Farms and the Effect of Neighbouring Wind Farms," J. Phys.: Conf. Ser., **524**(1), p. 012162.

[4] Calaf, M., Meneveau, C., and Meyers, J., 2010, "Large Eddy Simulation Study of Fully Developed Wind-Turbine Array Boundary Layers," Physics of Fluids, **22**(1), p. 015110.

[5] Porté-Agel, F., Wu, Y.-T., Lu, H., and Conzemius, R. J., 2011, "Large-Eddy Simulation of Atmospheric Boundary Layer Flow through Wind Turbines and Wind Farms," Journal of Wind Engineering and Industrial Aerodynamics, **99**(4), pp. 154–168.

[6] Churchfield, M., Lee, S., Moriarty, P., Martinez, L., Leonardi, S., Vijayakumar, G., and Brasseur, J., 2012, "A Large-Eddy Simulation of Wind-Plant Aerodynamics," *50th AIAA Aerospace Sciences Meeting Including the New Horizons Forum and Aerospace Exposition,* American Institute of Aeronautics and Astronautics.

[7] Das, R., and Lee, S., 2019, "Numerical Perspectives on Wind Turbine Wakes," p. G42.005.

[8] Das, R. C., and Shen, Y.-L., 2023, "Analysis of Wind Farms under Different Yaw Angles and Wind Speeds," Energies, **16**(13), p. 4953.

[9] Smagorinsky, J., 1963, “GENERAL CIRCULATION EXPERIMENTS WITH THE PRIMITIVE EQUATIONS: I. THE BASIC EXPERIMENT,” Monthly Weather Review, **91**(3), pp. 99–164.

[10] Deardorff, J. W., 1970, “A Numerical Study of Three-Dimensional Turbulent Channel Flow at Large Reynolds Numbers,” Journal of Fluid Mechanics, **41**(2), pp. 453–480.

[11] Bou-Zeid, E., Meneveau, C., and Parlange, M., 2005, “A Scale-Dependent Lagrangian Dynamic Model for Large Eddy Simulation of Complex Turbulent Flows,” Physics of Fluids, **17**(2), p. 025105.

[12] Falgout, R. D., and Yang, U. M., 2002, “Hypre: A Library of High Performance Preconditioners,” *Computational Science — ICCS 2002*, P.M.A. Sloot, A.G. Hoekstra, C.J.K. Tan, and J.J. Dongarra, eds., Springer, Berlin, Heidelberg, pp. 632–641.

[13] Mason, P. J., and Thomson, D. J., 1992, “Stochastic Backscatter in Large-Eddy Simulations of Boundary Layers,” Journal of Fluid Mechanics, **242**, pp. 51–78.

[14] K, L. D., 1967, “The Representation of Small-Scale Turbulence in Numerical Simulation Experiments,” Proc. IBM Sci. Comput. Symp. on Environmental Science, pp. 195–210.

[15] Germano, M., Piomelli, U., Moin, P., and Cabot, W. H., 1991, “A Dynamic Subgrid-scale Eddy Viscosity Model,” Physics of Fluids A: Fluid Dynamics, **3**(7), pp. 1760–1765.

[16] Porté-Agel, F., Meneveau, C., and Parlange, M. B., 2000, “A Scale-Dependent Dynamic Model for Large-Eddy Simulation: Application to a Neutral Atmospheric Boundary Layer,” Journal of Fluid Mechanics, **415**, pp. 261–284.

[17] Meneveau, C., Lund, T. S., and Cabot, W. H., 1996, “A Lagrangian Dynamic Subgrid-Scale Model of Turbulence,” Journal of Fluid Mechanics, **319**, pp. 353–385.

[18] Sørensen, J. N., and Myken, A., 1992, "Unsteady Actuator Disc Model for Horizontal Axis Wind Turbines," Journal of Wind Engineering and Industrial Aerodynamics, **39**(1), pp. 139–149.

[19] Jiménez, Á., Crespo, A., and Migoya, E., 2010, "Application of a LES Technique to Characterize the Wake Deflection of a Wind Turbine in Yaw," Wind Energy, **13**(6), pp. 559–572.

[20] Bastankhah, M., and Porté-Agel, F., 2016, "Experimental and Theoretical Study of Wind Turbine Wakes in Yawed Conditions," Journal of Fluid Mechanics, **806**, pp. 506–541.

[21] Lin, M., and Porté-Agel, F., 2019, "Large-Eddy Simulation of Yawed Wind-Turbine Wakes: Comparisons with Wind Tunnel Measurements and Analytical Wake Models," Energies, **12**(23), p. 4574.

[22] Chen, Y., Li, H., Jin, K., and Song, Q., 2013, "Wind Farm Layout Optimization Using Genetic Algorithm with Different Hub Height Wind Turbines," Energy Conversion and Management, **70**, pp. 56–65.

[23] Wang, L., Tan, A. C. C., Cholette, M., and Gu, Y., 2016, "Comparison of the Effectiveness of Analytical Wake Models for Wind Farm with Constant and Variable Hub Heights," Energy Conversion and Management, **124**, pp. 189–202.

[24] Stanley, A. P. J., Ning, A., and Dykes, K., 2019, "Optimization of Turbine Design in Wind Farms with Multiple Hub Heights, Using Exact Analytic Gradients and Structural Constraints," Wind Energy, **22**(5), pp. 605–619.

[25] Vasel-Be-Hagh, A., and Archer, C. L., 2017, "Wind Farm Hub Height Optimization," Applied Energy, **195**, pp. 905–921.

[26] Chatterjee, T., and Peet, Y., 2019, "Exploring the Benefits of Vertically Staggered Wind Farms: Understanding the Power Generation Mechanisms of Turbines Operating at Different Scales," Wind Energy, **22**(2), pp. 283–301.

[27] IPCC, Allen, M., Babiker, M., Chen, Y., de Coninck, H., Connors, S., van Diemen, R., Dube, O., Ebi, K., Engelbrecht, F., Ferrat, M., Ford, J., Forster, P., Fuss, S., Guillén Bolaños, T., Harold, J., Hoegh-Guldberg, O., Hourcade, J.-C., Huppmann, D., and Zickfeld, K., 2018, "Summary for Policymakers. In: Global Warming of 1.5°C. An IPCC Special Report."

[28] Medici, D., and Dahlberg, J. Å., 2003, "Potential Improvement of Wind Turbine Array Efficiency by Active Wake Control (AWC)," pp. 65–84.

[29] Adaramola, M. S., and Krogstad, P.-Å., 2011, "Experimental Investigation of Wake Effects on Wind Turbine Performance," Renewable Energy, **36**(8), pp. 2078–2086.

[30] Gebraad, P. M. O., Teeuwisse, F. W., van Wingerden, J. W., Fleming, P. A., Ruben, S. D., Marden, J. R., and Pao, L. Y., 2016, "Wind Plant Power Optimization through Yaw Control Using a Parametric Model for Wake Effects—a CFD Simulation Study," Wind Energy, **19**(1), pp. 95–114.

[31] Wu, Y.-T., Lin, C.-Y., and Chang, T.-J., 2020, "Effects of Inflow Turbulence Intensity and Turbine Arrangements on the Power Generation Efficiency of Large Wind Farms," Wind Energy, **23**.

[32] Churchfield, M. J., Lee, S., Michalakes, J., and Moriarty, P. J., 2012, "A Numerical Study of the Effects of Atmospheric and Wake Turbulence on Wind Turbine Dynamics," Journal of Turbulence, **13**, p. N14.

[33] Larsen, G. C., Madsen, H. Aa., Thomsen, K., and Larsen, T. J., 2008, “Wake Meandering: A Pragmatic Approach,” Wind Energy, **11**(4), pp. 377–395.

[34] Mishnaevsky, L., Hasager, C. B., Bak, C., Tilg, A.-M., Bech, J. I., Doagou Rad, S., and Fæster, S., 2021, “Leading Edge Erosion of Wind Turbine Blades: Understanding, Prevention and Protection,” Renewable Energy, **169**, pp. 953–969.

[35] Carraro, M., De Vanna, F., Zweiri, F., Benini, E., Heidari, A., and Hadavinia, H., 2022, “CFD Modeling of Wind Turbine Blades with Eroded Leading Edge,” Fluids, **7**(9), p. 302.

[36] Medici, D., and Alfredsson, P. H., 2006, “Measurements on a Wind Turbine Wake: 3D Effects and Bluff Body Vortex Shedding,” Wind Energy, **9**(3), pp. 219–236.

[37] Chamorro, L. P., and Porté-Agel, F., 2009, “A Wind-Tunnel Investigation of Wind-Turbine Wakes: Boundary-Layer Turbulence Effects,” Boundary-Layer Meteorol, **132**(1), pp. 129–149.

[38] Wu, Y.-T., and Porté-Agel, F., 2011, “Large-Eddy Simulation of Wind-Turbine Wakes: Evaluation of Turbine Parametrisations,” Boundary-Layer Meteorol, **138**(3), pp. 345–366.

[39] Howland, M. F., Bossuyt, J., Martínez-Tossas, L. A., Meyers, J., and Meneveau, C., 2016, “Wake Structure in Actuator Disk Models of Wind Turbines in Yaw under Uniform Inflow Conditions,” Journal of Renewable and Sustainable Energy, **8**(4), p. 043301.

[40] Fleming, P. A., Gebraad, P. M. O., Lee, S., van Wingerden, J.-W., Johnson, K., Churchfield, M., Michalakes, J., Spalart, P., and Moriarty, P., 2014, “Evaluating Techniques for Redirecting Turbine Wakes Using SOWFA,” Renewable Energy, **70**, pp. 211–218.

[41] Shapiro, C. R., Gayme, D. F., and Meneveau, C., 2018, “Modelling Yawed Wind Turbine Wakes: A Lifting Line Approach,” Journal of Fluid Mechanics, **841**, p. R1.

[42] Qian, G.-W., and Ishihara, T., 2018, “A New Analytical Wake Model for Yawed Wind Turbines,” Energies, **11**(3), p. 665.

[43] Aitken, M. L., and Lundquist, J. K., 2014, “Utility-Scale Wind Turbine Wake Characterization Using Nacelle-Based Long-Range Scanning Lidar,” Journal of Atmospheric and Oceanic Technology, **31**(7), pp. 1529–1539.

[44] Maeda, T., Kamada, Y., Murata, J., Yonekura, S., Ito, T., Okawa, A., and Kogaki, T., 2011, “Wind Tunnel Study on Wind and Turbulence Intensity Profiles in Wind Turbine Wake,” J. Therm. Sci., **20**(2), pp. 127–132.

[45] Troldborg, N., Sørensen, J. N., and Mikkelsen, R., 2007, “Actuator Line Simulation of Wake of Wind Turbine Operating in Turbulent Inflow,” J. Phys.: Conf. Ser., **75**(1), p. 012063.

[46] Wu, Y.-T., and Porté-Agel, F., 2012, “Atmospheric Turbulence Effects on Wind-Turbine Wakes: An LES Study,” Energies, **5**(12), pp. 5340–5362.

[47] Chamorro, L. P., and Porté-Agel, F., 2010, “Effects of Thermal Stability and Incoming Boundary-Layer Flow Characteristics on Wind-Turbine Wakes: A Wind-Tunnel Study,” Boundary-Layer Meteorol, **136**(3), pp. 515–533.

[48] Iungo, G. V., Wu, Y.-T., and Porté-Agel, F., 2013, “Field Measurements of Wind Turbine Wakes with Lidars,” Journal of Atmospheric and Oceanic Technology, **30**(2), pp. 274–287.

[49] Li, Q., Murata, J., Endo, M., Maeda, T., and Kamada, Y., 2016, "Experimental and Numerical Investigation of the Effect of Turbulent Inflow on a Horizontal Axis Wind Turbine (Part II: Wake Characteristics)," Energy, **113**, pp. 1304–1315.

[50] Wiser, R. H., and Bolinger, M., 2019, "2018 Wind Technologies Market Report."

[51] Stathopoulos, T., Alrawashdeh, H., Al-Quraan, A., Blocken, B., Dilimulati, A., Paraschivoiu, M., and Pilay, P., 2018, "Urban Wind Energy: Some Views on Potential and Challenges," Journal of Wind Engineering and Industrial Aerodynamics, **179**, pp. 146–157.

[52] Al-Quraan, A., Stathopoulos, T., and Pillay, P., 2016, "Comparison of Wind Tunnel and on Site Measurements for Urban Wind Energy Estimation of Potential Yield," Journal of Wind Engineering and Industrial Aerodynamics, **158**, pp. 1–10.

[53] Bataineh, K. M., and Dalalah, D., 2013, "Assessment of Wind Energy Potential for Selected Areas in Jordan," Renewable Energy, **59**, pp. 75–81.

[54] Al-Quraan, A., and Al-Mhairat, B., 2022, "Intelligent Optimized Wind Turbine Cost Analysis for Different Wind Sites in Jordan," Sustainability, **14**(5), p. 3075.

[55] Li, Q., Jia, H., Qiu, Q., Lu, Y., Zhang, J., Mao, J., Fan, W., and Huang, M., 2022, "Typhoon-Induced Fragility Analysis of Transmission Tower in Ningbo Area Considering the Effect of Long-Term Corrosion," Applied Sciences, **12**(9), p. 4774.

[56] Fleming, P. A., Ning, A., Gebraad, P. M. O., and Dykes, K., 2016, "Wind Plant System Engineering through Optimization of Layout and Yaw Control," Wind Energy, **19**(2), pp. 329–344.

[57] Machielse, L., Schepers, J., and Wagenaar, J., 2012, "Controlling Wind in ECN`s Scaled Wind Farm."

[58] Fleming, P., Annoni, J., Shah, J. J., Wang, L., Ananthan, S., Zhang, Z., Hutchings, K., Wang, P., Chen, W., and Chen, L., 2017, "Field Test of Wake Steering at an Offshore Wind Farm," Wind Energy Science, **2**(1), pp. 229–239.

[59] Howland, M. F., Lele, S. K., and Dabiri, J. O., 2019, "Wind Farm Power Optimization through Wake Steering," Proceedings of the National Academy of Sciences, **116**(29), pp. 14495–14500.

[60] Simley, E., Fleming, P., Girard, N., Alloin, L., Godefroy, E., and Duc, T., 2021, "Results from a Wake-Steering Experiment at a Commercial Wind Plant: Investigating the Wind Speed Dependence of Wake-Steering Performance," Wind Energy Science, **6**(6), pp. 1427–1453.

[61] Bastankhah, M., and Porté-Agel, F., 2014, "A New Analytical Model for Wind-Turbine Wakes," Renewable Energy, **70**, pp. 116–123.

APPENDIX

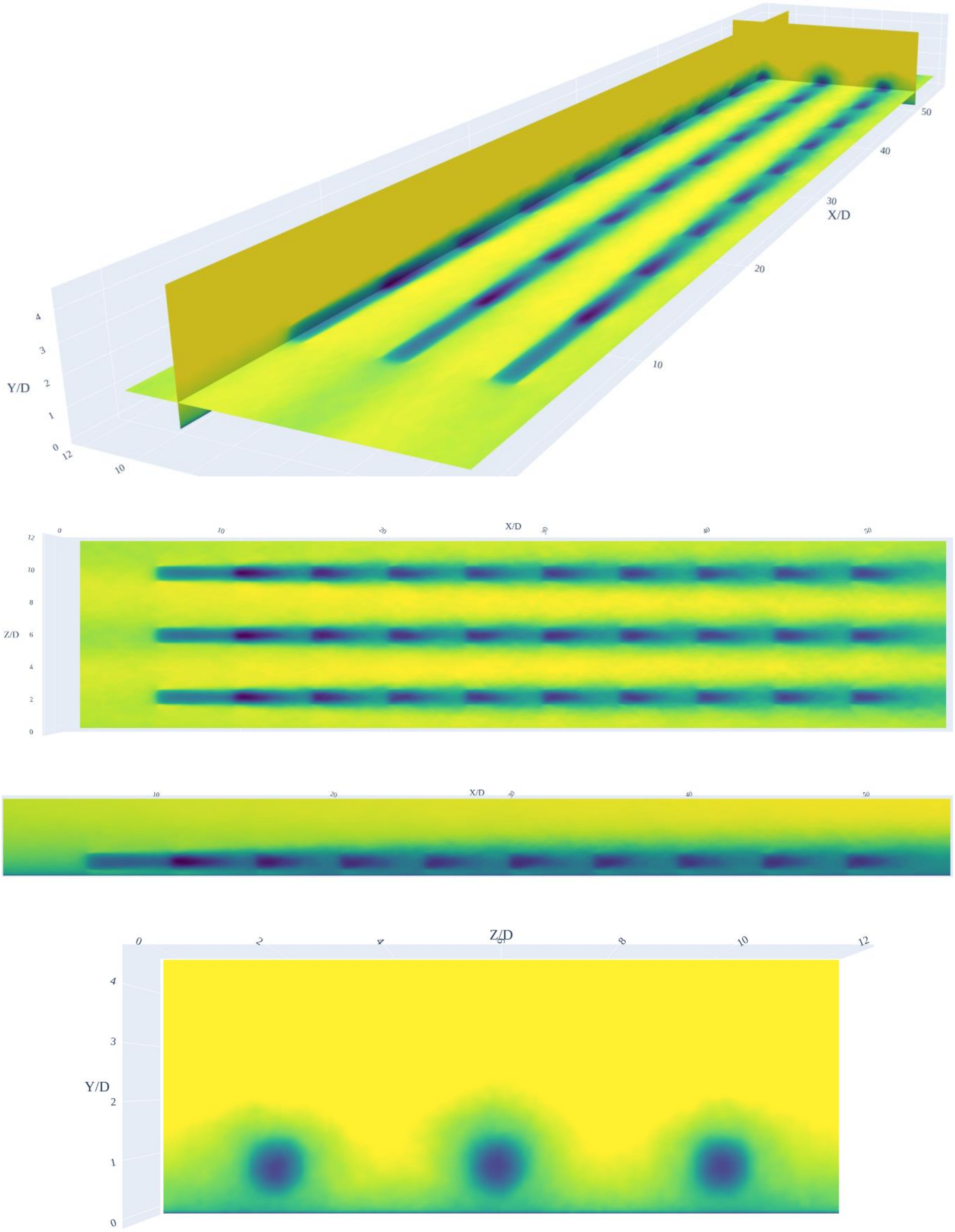

Figure: Time-average flow field of the wind farm validation case.

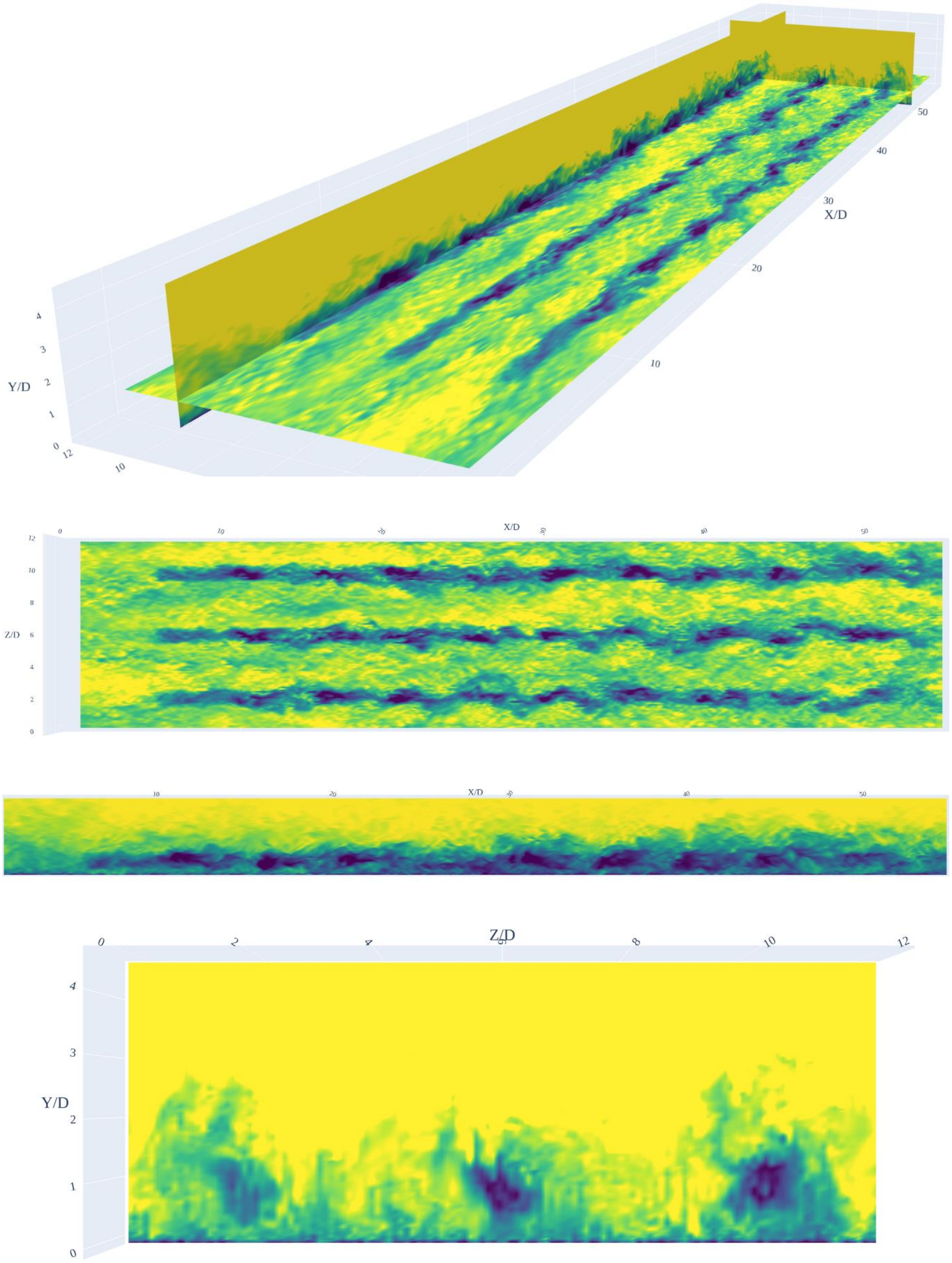

Figure: Instantaneous flow field of the wind farm validation case.

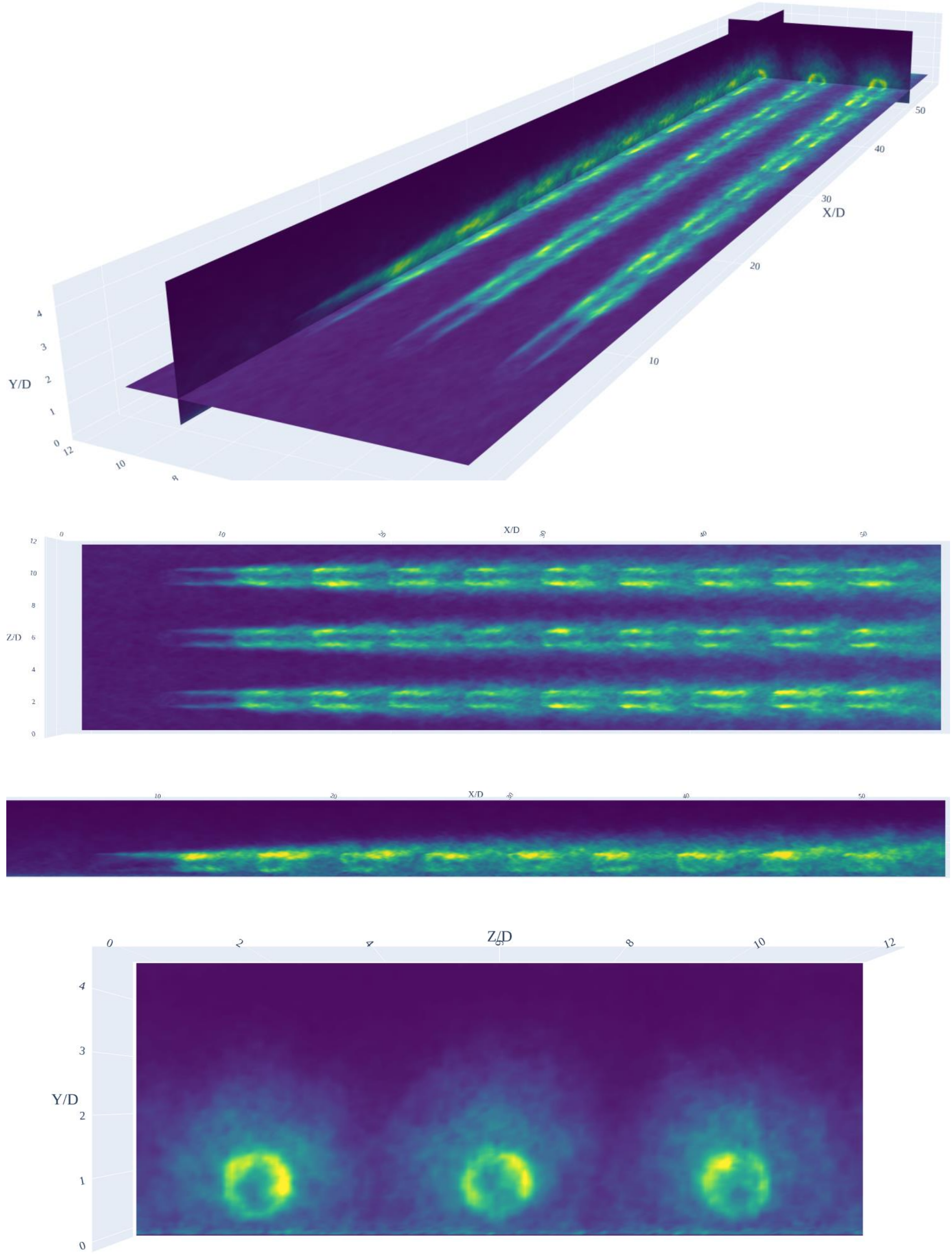

Figure: Turbulence intensity contours of the wind farm validation case.